

Modifying spin diffusion in a nondegenerate ultracold gas

by

Sean David Graham

B.Sc., University of Waterloo, 2013

Thesis Submitted in Partial Fulfillment of the
Requirements for the Degree of
Doctor of Philosophy

in the
Department of Physics
Faculty of Science

© Sean David Graham 2019
SIMON FRASER UNIVERSITY
Fall 2019

Copyright in this work rests with the author. Please ensure that any reproduction or re-use is done in accordance with the relevant national copyright legislation.

Approval

Name: Sean David Graham
Degree: Doctor of Philosophy (Physics)
Title: Modifying spin diffusion in a nondegenerate ultracold gas
Examining Committee: **Chair:** Karen Kavanagh
Professor

Jeffrey McGuirk
Senior Supervisor
Associate Professor

Malcolm Kennett
Supervisor
Associate Professor

Paul Haljan
Supervisor
Associate Professor

Michael Hayden
Internal Examiner
Professor

Peter Engels
External Examiner
Professor
Department of Physics and
Astronomy
Washington State University

Date Defended: December 9, 2019

Abstract

Diffusion plays a major role in describing how particles and heat move in any nonequilibrium system. The diffusion of quantum properties is not as well understood as the diffusion of classical properties, especially at low temperatures or high densities. Exploring the diffusion of the quantum property known as spin is beneficial for explaining quantum effects that arise at low temperatures or high densities, and this knowledge acquired could assist in the development of new ultra-low-power devices. This thesis examines spin diffusion at various temperatures and densities using the highly-tunable experimental platform of ultracold atoms.

Around one million rubidium-87 atoms are cooled to nanokelvin temperatures to create an ultracold gas, where quantum interactions between atoms can significantly modify spin diffusion compared to classical diffusion. One-dimensional spin diffusion is observed for an initial two-domain spin profile. Remarkably, diffusion of this spin profile is slowed at temperatures above quantum degeneracy, where the ultracold gas is largely classical but with quantum collisions. We demonstrate that this slowing of spin diffusion is due to the presence of spin coherence between spin domains, and that the removal of coherence speeds up spin diffusion to classical timescales.

Spin diffusion is further modified by applying a linear differential potential that can speed, slow, or stop spin diffusion of a two-domain spin profile. Differential potentials spatially alter the precession of spins, which then alters the spin-rotating quantum collisions that modify spin diffusion. For a linear differential potential with a specific sign and magnitude, stabilized spin domains in an ultracold gas are observed for 40 times longer than classical diffusion timescales.

In addition to modifying spin diffusion with coherence and differential potentials, we demonstrate arbitrary control of one-dimensional spin diffusion using temporally varying differential potentials and three-domain spin profiles. These spin diffusion modifying techniques could be useful for manipulating spin in other nonequilibrium systems, and set the stage for simulating spin-based devices in ultracold atoms.

Keywords: ultracold atoms, spin diffusion, spin transport, nondegenerate, nonequilibrium

Acknowledgements

I would like to express my deepest gratitude to my advisor, Jeffrey McGuirk. All of Jeff's support, knowledge, advice, and pedagogy over the course of my graduate schooling is greatly appreciated. I am thankful for having the opportunity to work with Jeff over the years, and I will truly miss being part of the McGuirk group.

I want to thank my committee members Malcolm Kennett and Paul Haljan for their insightful research and career advice. I was fortunate to have worked with Dorna Niroomand, where her knowledge and training on the experiment was invaluable. This thesis would not be possible without all of Dorna's efforts, and I want to explicitly thank her for those efforts. Thanks to Danyel, Alex, Juan, Kshitij, Jake, Santiago, Martin, David, and Olga, who have all contributed to the experiment during this thesis. I am also appreciative to my previous advisors, John Nieminen, Robert Weersink and Jim Martin, who sparked my interest in pursuing graduate school in atomic physics at SFU.

Thank you to Janet Rumleskie for supporting me over the years and putting up with the long work days and nights. Janet's never-ending support and motivation over the years is greatly appreciated. Lastly, I want to thank my parents (Peggy and David), sisters, and the rest of my family for their support, encouragement, and interest over the years. I would not have been able to write this thesis without all of their support.

Table of Contents

Approval	ii
Abstract	iii
Acknowledgements	v
Table of Contents	vi
List of Tables	ix
List of Figures	x
1 Introduction	1
1.1 Ultracold atoms	1
1.2 Spin diffusion	3
1.3 Thesis overview	5
2 Spin diffusion theory	7
2.1 Two-level spin system	7
2.1.1 Optical Bloch equations	9
2.1.2 Ramsey interferometry	11
2.1.3 Two-photon spectroscopy	12
2.2 Identical spin rotation effect	14
2.3 Spin diffusion theory	21
2.4 Simulations of spin diffusion	23
2.4.1 Alternating-direction-implicit method	24
2.4.2 Dynamic time stepping	25
2.5 Spin-dependent and independent potentials	26
3 Apparatus and procedures	31
3.1 Experimental overview	31

3.1.1	Magneto-optical trap	31
3.1.2	The science cell	37
3.2	Spin profile preparation	40
3.3	Imaging atoms	42
3.3.1	Experimental procedure	42
3.3.2	Image processing	44
3.3.3	Fitting for cloud parameters	47
3.4	Accessible phase space	48
3.5	Spin detection	52
3.5.1	Longitudinal spin detection	52
3.5.2	Transverse spin detection	55
3.6	Total spin by combining spin components	62
3.7	Effective magnetic field control	64
3.8	Digital micromirror device	70
3.8.1	Firmware	73
3.8.2	Optics	76
3.8.3	Error diffusion	79
4	Calibrations	84
4.1	Magnetic trap frequencies	84
4.2	Radio frequency evaporation and trap bottom	87
4.3	Magnetic bias field	88
4.4	Adiabatic rapid passage	89
4.5	Probe local oscillator frequency	91
4.6	Imaging camera and DMD image focus	92
4.7	Magnification	97
4.8	Probe intensity	100
4.9	Atomic cloud density	100
4.9.1	Density calibration with 2D images	101
4.9.2	Density calibration with 1D density profiles	102
4.10	Optimizing the initial spin profile	106
5	Diffusion of a dipolar spin profile	110
5.1	Spin diffusion with high initial coherence	110
5.2	The effect of coherence on longitudinal spin diffusion	116
5.3	A spin instability	118

5.4	Summary	121
6	Stable spin domains	123
6.1	Effect of linear differential potentials	123
6.2	Tracking domain stability	124
6.3	Transverse spin waves	131
6.4	Towards arbitrary control of 1D spin diffusion	133
7	Conclusion	137
7.1	Future enhancements	138
7.2	Future experiments	140
	Bibliography	143
	Appendix A Physical parameters of ^{87}Rb	154
	Appendix B Collisional integrals for 1D spin transport	155
	Appendix C 1D quantum Boltzmann equation in Cartesian, cylindrical, and spherical coordinate systems	156

List of Tables

Table 3.1	USB endpoints used by DMD	74
Table 3.2	USB vendor commands	75
Table 3.3	Custom DMD register addresses for USB	75
Table A.1	Selection of relevant properties of ^{87}Rb	154

List of Figures

Figure 2.1	The Bloch sphere	9
Figure 2.2	Rabi oscillations in the Bloch sphere	10
Figure 2.3	Two-photon spectroscopy energy levels	13
Figure 2.4	Collisions between distinguishable and indistinguishable atoms	15
Figure 2.5	Example of the identical spin rotation effect	16
Figure 2.6	Dipolar energy shift	29
Figure 3.1	Doppler cooling in one dimension	33
Figure 3.2	Schematic of the magneto-optical trap vacuum cell	34
Figure 3.3	Zeeman levels localizing atoms in a MOT	35
Figure 3.4	Atomic transitions used for the cooling and repump lasers . .	36
Figure 3.5	Hybrid Ioffe-Pritchard trap	38
Figure 3.6	Two-photon transition energy levels	41
Figure 3.7	Masking technique used to prepare initial spin profiles	41
Figure 3.8	Helical spin structure	42
Figure 3.9	Energy levels used in imaging atoms	43
Figure 3.10	Imaging correction factors	46
Figure 3.11	Example absorption image	48
Figure 3.12	Accessible parameter space	50
Figure 3.13	Longitudinal spin detection	54
Figure 3.14	Longitudinal spin diffusion normalization	55
Figure 3.15	Comparison of how phases shift in the three transverse spin measurement techniques	57
Figure 3.16	Moving window method to process and measure transverse spin	59
Figure 3.17	Pseudo-PSK technique for processing and measuring transverse spin	61
Figure 3.18	PSK technique for measuring transverse spin	63
Figure 3.19	Total spin profiles	64
Figure 3.20	Cancellation of the mean-field and Zeeman shift	66

Figure 3.21	Cancellation and magic spots	67
Figure 3.22	Differential potential at the cancellation spot	68
Figure 3.23	Laser painting with an acousto-optical modulator	69
Figure 3.24	Measured differential potentials generated with laser painting	71
Figure 3.25	Digital micromirror device cartoon	72
Figure 3.26	Discovery 4100 control board schematic	73
Figure 3.27	First pattern on the digital micromirror device	77
Figure 3.28	Optical setup for the digital micromirror device	78
Figure 3.29	Comparison of a error diffused pattern with the 8-bit pattern .	82
Figure 3.30	DMD generated differential potential	83
Figure 4.1	Magnetic field coil placement for trap frequency measurement	85
Figure 4.2	Trap frequency measurement	86
Figure 4.3	RF evaporation frequency cuts	87
Figure 4.4	Magnetic field calibration	90
Figure 4.5	Adiabatic rapid passage frequency calibration	90
Figure 4.6	Cloud temperature while tuning the adiabatic rapid passage frequency	91
Figure 4.7	Probe local oscillator calibration	93
Figure 4.8	Focusing the imaging camera	94
Figure 4.9	Single Ramsey image used for measuring DMD focus	96
Figure 4.10	Focusing the DMD image onto the atoms	97
Figure 4.11	Measuring image magnification with falling atoms	98
Figure 4.12	Measurement of image magnification using weakly trapped atoms	99
Figure 4.13	2D cloud type detection	103
Figure 4.14	Density profile fitted for density calibration	104
Figure 4.15	Density calibration using the condensate fraction	105
Figure 4.16	Optical Bloch simulations of spin profile preparation	107
Figure 4.17	Optimizing detuning using spin domain balance	109
Figure 5.1	Coherence measured in a helical domain structure	112
Figure 5.2	Longitudinal spin diffusion for max coherence	113
Figure 5.3	Transverse spin diffusion of a dipolar spin profile	115
Figure 5.4	Longitudinal spin diffusion with various initial coherences . . .	116
Figure 5.5	Dipole moment during longitudinal spin diffusion at various initial coherences	117

Figure 5.6	Damping and oscillation rate of the dipole moment	118
Figure 5.7	Transverse spin diffusion at different initial coherences	119
Figure 5.8	Ensemble coherence dynamics at different initial coherences	121
Figure 5.9	Numerical simulation of the transverse instability strength	122
Figure 6.1	Spatiotemporal evolution of longitudinal spin with a linear dif- ferential potential	125
Figure 6.2	Domain wall width dynamics	127
Figure 6.3	Stabilizing gradient	129
Figure 6.4	Transverse spin diffusion in a stable longitudinal spin domain	132
Figure 6.5	Spin diffusion with a gradient that flips sign	134
Figure 6.6	Stabilized three-domain spin profile	135

Chapter 1

Introduction

1.1 Ultracold atoms

Physics occurring at the coldest possible temperatures was never considered until around 1665 when Boyle first discussed the possibility of an absolute zero temperature [1]. Nearly two centuries later, Lord Kelvin presented the idea of an absolute zero and the now well-known Kelvin temperature scale in 1848 [2]. In 1823 Faraday demonstrated how to liquefy chlorine to temperatures of 143 K, achieving the coldest temperature at the time [3, 4]. Liquefying different gases continued as groups searched for the element with the lowest boiling point, which led to the first production of liquid nitrogen at 77 K in 1883 [5, 6], hydrogen at 23 K in 1898 [7], and helium at 4 K in 1908 by Onnes [8]. The lab that Onnes started would be the first to demonstrate the next big decrease in temperature with the realization of London's design [9] of a helium dilution fridge in 1964, reaching temperatures of 2 mK [10]. Remarkably, over the span of only three centuries, the coldest temperatures experimentally accessible dropped five orders of magnitude. However, researchers continued to search for cooling techniques to reach lower temperatures that could be used to observe nonclassical physics.

In 1978, laser cooling experiments demonstrated that it was possible to cool ions to less than 40 K using lasers, and it was postulated that laser cooling could reach millikelvin temperatures [11, 12, 13]. The laser cooling of ions was adapted to cool a gas of neutral atoms and microkelvin temperatures were achieved [14, 15, 16, 17]. And in 1995, Cornell and Wiemann, and Ketterle independently reached temperatures around 170 nK, which is significantly colder than any previously observed and shows incredible progress in only a couple decades. Temperatures below 1 mK are typically referred to as ultracold temperatures. At these temperatures, the two aforementioned

groups independently observed [18, 19] a Bose-Einstein condensate (BEC), a new phase of matter predicted to exist at ultracold temperatures by Bose and Einstein in 1924 [20, 21]. To date, the coldest known object in the universe is still a BEC at a temperature of around 50 pK [22, 23].

Physics at these ultracold temperatures deviates significantly from classical physics. The position of an atom is not well defined, due to Heisenberg's uncertainty principle, so each atom is spread out spatially more than it would be at room temperature. The spatial extent of an atom is characterized by its thermal de Broglie wavelength. For room temperature objects the de Broglie wavelength is incredibly small, but for atoms in a BEC the de Broglie wavelength is larger than the average distance between atoms. In the case of a BEC, the atoms act collectively as a macroscopic quantum object since there is no clear definition of where one atom stops and the next begins. This quantum macro-object must obey the statistical properties specific to the fundamental particles of which it is composed. A BEC must obey Bose-Einstein statistics since it is composed of bosons with integer spin. At ultracold temperatures, bosons condense to a BEC because Bose-Einstein statistics specify that bosons tend to group together into a ground state. Fermions (particles with half-integer spin) on the other hand obey Fermi-Dirac statistics and no two atoms can be in the same state. Fermions at ultracold temperatures keep their distance from each other, forming degenerate Fermi gases (DFG). BECs and DFGs are two classes of degenerate gases that are used to explore quantum mechanical effects that can be dominant near absolute zero.

The low temperatures reached by the liquefaction of gases led to new research fields, spawning dilution refrigerator experiments for exploring superconductivity [24, 25], quantum computation [26], and quantum magnetism [27]. Similarly, laser cooling and the observation of BECs began a research field that explores the quantum mechanical effects present at ultracold temperatures. The field of ultracold atom research now covers topics such as superconductivity [28], precision clocks [29, 30], gravity sensors [31, 32], phases in semiconductors [33], long-range interactions [34, 35, 36, 37], fundamental particle physics [38, 39], and spinor physics [40, 41, 42]. This broad range of topics is possible because of the tunability offered by ultracold atoms through advances in physics, optics, engineering, and technology. In addition, the specific atomic element used in experiments can drastically change the underlying quantum properties.

Currently, there are ultracold experiments in which a large variety of atoms and molecules are cooled and studied. For bosonic systems there are groups using Rb, Cs, K, Na, Li, Sr, Yb, and other atoms [43, 44]. As an example, the choice of element could

depend on the ease of tuning a contact interaction through a Feshbach resonance or the mass of the atom altering dynamic timescales. The atoms Sr and Yb are used to create highly precise clocks [45, 46] and to explore the dynamics of long-lived excited states [47]. Long-range interactions between atoms are explored in dipolar BECs made of atoms with large permanent magnetic dipole moments, such as Cr, Er, and Dy [34, 37, 36]. Fermionic systems using isotopes of Li or K can form a DFG that can be used to model the physics of electron transport in superconductors [48], spin-charge separation [49], universal spin transport [50], and for performing quantum simulations [51]. While ultracold atoms experiments cover a wide range of research topics, this thesis focuses on exploring the diffusion of spin with ultracold bosonic atoms.

1.2 Spin diffusion

In this thesis, ultracold atoms are used as a tunable experimental platform to explore the diffusion of the fundamental quantum property known as spin. Classical diffusion is well explained by Boltzmann transport theory, which can be used to describe the behaviour of a thermodynamic system that is out of equilibrium. As an example, Boltzmann transport theory is in use today to describe classical systems such as the diffusion of gases in the atmosphere and for improved temperature control by describing heat diffusion. While classical diffusion is suitable to describe those systems, it is not suitable for ultracold atoms where quantum mechanics plays a larger role. This thesis studies spin diffusion in an ultracold but nondegenerate gas of rubidium-87 at temperatures above the threshold for Bose-Einstein condensation. Despite using a nondegenerate ultracold gas that is above quantum degeneracy, quantum mechanical effects can be strong enough to modify spin diffusion.

The theory of spin diffusion in a nondegenerate gas was independently described by Bashkin and by Lhuillier and Laloë [52, 53, 54]. They showed that in nondegenerate systems the quantum indistinguishability of atoms leads to an identical spin rotation effect (ISRE) that can significantly modify spin diffusion. The modification of spin diffusion by the ISRE was demonstrated in helium nuclear magnetic resonance experiments, where a slower-than-classical spin diffusion rate was measured at temperatures below and above degeneracy [55, 56]. This behaviour was interpreted as collective behaviour due to quantum collisions that modify spin during a two-body collision [57]. These spin-rotating collisions were shown to be strong enough at temperatures above degeneracy that modified spin diffusion could be observed [55, 56].

Later, theoretical studies [58, 59] on spin diffusion suggested that examples of collective spin behaviour, such as spin waves, spin instabilities, and stable spin domains, were within reach in ultracold gas experiments.

A decade after the helium spin diffusion experiments, spin waves were observed in an ultracold gas where collective spin behaviour led to an oscillation of spin within a nondegenerate gas [60]. Unlike the earlier helium experiment, where the spatially averaged spin was measured as a function of time, spin waves in ultracold gases were measured both temporally and spatially, providing an additional degree of freedom to experimentally characterize spin diffusion. Since then, collective spin behaviour was also demonstrated when spins remained coherent for longer than usual due to spin-rotating collisions, with this collective behaviour being known as spin self-rephasing [61]. In a Fermi gas, collective spin behaviour was demonstrated when spin interactions between two oppositely polarized dilute clouds were strong enough to cause the two clouds to rebound off of each other [62]. Recently, collective spin behaviour in a Mott insulator state was observed, demonstrating spatial separation of spin in a Mott insulator [63]. Additionally, collective spin behaviour was demonstrated with the observation of a transition between dynamical phases in a DFG [64].

Spin diffusion could be useful to the spintronics field, which aims to develop spin-based devices with some advantages over charge-based devices. These spintronic devices use spin instead of charge to create devices with new or improved functionalities, such as low-power digital memory. The potential advantages of spintronic devices over conventional semiconductor devices are stability, increased data processing speed, decreased electric power consumption, and increased integration densities [65, 66]. Successful incorporation of spin into current semiconductor technology requires efficient transport, control, and manipulation of spin. Learning how to modify spin diffusion in an ultracold gas could inform the spintronic semiconductor industry, potentially assisting in the development of spin-based devices.

The McGuirk group has previously explored spin diffusion in spinor BECs with a significant thermal component [67]. They have also demonstrated the effect of optically excited differential potentials on spin diffusion [68], and observed a localized collapse and revival of transverse spin [69]. This thesis builds on the previous work of the group by demonstrating how to speed, slow, and stop spin diffusion in a weakly-interacting nondegenerate ultracold gas of rubidium-87.

1.3 Thesis overview

This thesis describes studies of spin diffusion in a quasi-one-dimensional (quasi-1D) ultracold cloud of gas, where the effect of spin coherence and spatially varying effective magnetic fields are explored. This weakly-interacting ultracold gas is formed with rubidium-87 atoms cooled to temperatures that are just above quantum degeneracy. The use of a quasi-1D cloud simplifies studies of diffusion by limiting the degrees of freedom available to atoms, making it easier to compare experimental data to simulations of quantum diffusion theories. The degree of spin coherence is varied in these experiments. When all spins occupy the same local quantum state a high degree of coherence is obtained and spin diffusion is slowed. Additionally, the effective magnetic field alters the rate that spins precess at different positions in the cloud, and is shown to modify spin diffusion significantly.

In Chapter 2, a review of relevant spin-1/2 physics and spectroscopy is presented, and the coupling between light and atoms is described. Next, the spin-exchange effect known as the identical spin rotation effect that modifies spin diffusion is presented. This rotation effect comes from the quantum indistinguishability of atoms, and the description of how indistinguishability leads to a rotation of spins is reviewed. This rotation effect is included in a quantum Boltzmann transport equation to describe spin diffusion in a Bose gas. Spin diffusion can be further modified with spin-dependent and spin-independent potentials, and the theory of generating these potentials is also discussed. Lastly, the techniques used to numerically simulate spin diffusion are presented.

The experimental aspects of the study are discussed in Chapter 3. The process of trapping and cooling rubidium atoms to near degeneracy is discussed first. Next, a masking technique that is used to initialize a two-domain spin profile is described. This is followed by a discussion of the atomic imaging method. An overview of the densities and temperatures that are accessible in these experiments is presented, showing the available parameter space and limitations of the work described in this thesis. Next, the measurement techniques used to detect different spin components are presented, including a discussion on combining spin components to track the total spin in the system. Chapter 3 ends with a discussion of the techniques used to control the effective magnetic field or differential potential. A method that uses an acousto-optical modulator to “paint” simple differential potential patterns with a laser is first presented. This is followed by a description of a digital micromirror device that allows arbitrary differential potential patterns and initial spin profiles to be generated.

In Chapter 4 the most common, and most critical, calibrations required for smooth operation of the experiment are discussed. This includes descriptions of when certain calibrations should be performed and methods for each one. This chapter does not include a description of all possible calibrations, but it does include a description all calibrations that were performed as part of the work described in this thesis.

The effect of coherence on spin diffusion is demonstrated in Chapter 5. Here the presence of coherence is shown to be the dominant modifier of spin diffusion at ultracold temperatures. The transverse and longitudinal spins for various initial coherences are studied, and an instability in ensemble coherence is presented. The phase space of this instability is explored numerically, highlighting where the effect can be strengthened for future studies.

Spin diffusion is further modified in Chapter 6 through the application of a linear differential potential. This potential is shown to speed, slow, or stop spin diffusion depending on the sign and magnitude of the applied field. The applied field that stops spin diffusion and stabilizes the spin domains is experimentally measured and compared to a hydrodynamic prediction based on the quantum Boltzmann transport equation. The techniques used to stabilize two-domain spin profiles can be extended to allow for arbitrary control of spin diffusion and two examples of this arbitrary control are shown.

A summary of the main results in this thesis can be found in Chapter 7. Experimental enhancements that could be done to improve upon the work presented in this thesis are discussed. A discussion of some newly accessible spin diffusion experimental studies is given, along with a discussion of how one could expand on this work.

Chapter 2

Spin diffusion theory

This chapter discusses the relevant theoretical frameworks for describing spin transport in a one-dimensional (1D) system. It begins with a review of two-level systems and spectroscopy techniques used for measuring and manipulating spin. Next, we discuss how ultracold temperatures and atom indistinguishability can lead to a two-body spin exchange interaction, known as the identical spin rotation effect. This spin rotation effect is the dominant effect that modifies spin diffusion in our ultracold gases. A quantum Boltzmann transport equation that describes 1D spin diffusion in our 1D weakly-interacting Bose gas is then presented. This 1D spin diffusion can be modified by using light to apply spatially varying spin-dependent and spin-independent potentials, and a relevant theoretical description is presented. Lastly, a discussion of the technique used to numerically simulate spin diffusion with the quantum Boltzmann equation is provided, which is invaluable for comparisons of data to theory.

2.1 Two-level spin system

A theoretical description of two-level spin systems forms the foundation for measuring and manipulating spin in any spin-1/2 system. An atom with two energy states can map onto a two-state spin system, where g and e denote the ground and excited state. Placing the atom in an oscillating electric field couples these two states, which can be described with a two-level Hamiltonian

$$H = \begin{pmatrix} \hbar\omega_0/2 & \Omega_R e^{i\omega t/2} \\ \Omega_R e^{-i\omega t/2} & -\hbar\omega_0/2 \end{pmatrix}, \quad (2.1)$$

where ω_0 is the frequency separating the two energy states, ω is the frequency of the oscillating field, Ω_R is the Rabi frequency, and t is the interaction time between the

atom and the oscillating field. The strength of the coupling is characterized by the Rabi frequency

$$\Omega_R = \frac{\mathbf{d}_{ge} \cdot \mathbf{E}}{\hbar}, \quad (2.2)$$

where $\mathbf{E} = \hat{\epsilon}E_0$ describes the electric field with amplitude E_0 and polarization $\hat{\epsilon}$, and \mathbf{d}_{ge} is the electric dipole transition operator. The electric dipole transition operator $\mathbf{d}_{ge} = \langle \psi_g | -e\hat{\mathbf{r}} | \psi_e \rangle$ describes the coupling of the electric field and the two energy states. Here $\hat{\mathbf{r}}$ is the position operator, e is the charge of an electron, and $|\psi_g\rangle$ and $|\psi_e\rangle$ are the wavefunctions for the ground and excited states.

Solving the time-dependent Schrödinger equation

$$i\hbar \frac{\partial |\psi\rangle}{\partial t} = H|\psi\rangle \quad (2.3)$$

with the coupled two-level Hamiltonian can be done with the rotating wave approximation. The resulting probability of an atom starting in the ground state and being in the excited state after time t is [70]

$$P_e(t) = \left(\frac{\Omega_R}{\Omega'_R} \right)^2 \sin^2 \left(\frac{\Omega'_R t}{2} \right). \quad (2.4)$$

At resonance ($\Omega'_R = \Omega_R$), the state oscillates between the excited and ground states at the Rabi frequency. This oscillation of the state population in an oscillating field is called Rabi flopping. Off resonance, the effective Rabi frequency Ω'_R is altered such that

$$\Omega'_R = \sqrt{|\Omega_R|^2 + \Delta^2}, \quad (2.5)$$

where $\Delta = \omega - \omega_0$ is the detuning of the applied oscillating field from resonance. A finite detuning increases the oscillation frequency but lowers the probability amplitude of these oscillations. Altering the resonant Rabi frequency Ω_R without a loss of probability amplitude requires changing the amplitude of the oscillating field E or using atomic states with a different electric dipole transition operator.

The sine term in Eqn. 2.4 is maximized for $\Omega'_R t_\pi = \pi$ and the probability is halved for $\Omega'_R t_{\pi/2} = \pi/2$. These two conditions define what are known as a π -pulse and $\pi/2$ -pulse, which correspond to rotations of the spin in the Bloch sphere by π and $\pi/2$ respectively. Both of these pulse timings are crucial for state manipulation of a two-level system and are used for state manipulation in this thesis (see Sections 3.2 and 3.5).

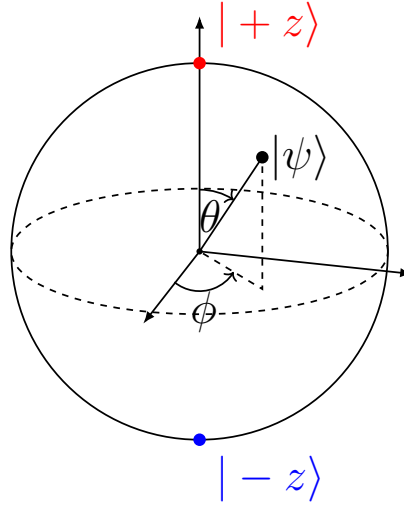


Figure 2.1: The Bloch sphere is used to visualize the evolution of a spin in an oscillating electric field. The spin state $|\psi\rangle$ is represented by a vector on the Bloch sphere, with azimuthal angle ϕ and zenith angle θ . The ground state $|-z\rangle$ corresponds to a vector pointing towards the bottom of the sphere (blue dot) and the excited state $|+z\rangle$ is a vector pointing to the top of the sphere (red dot). The ground and excited state are the longitudinal spin components. Spin vectors in the x-y plane at the equator of the sphere are purely transverse (superposition) spin states.

2.1.1 Optical Bloch equations

The Bloch sphere is a powerful framework to describe two-level quantum systems and how the quantum states evolve in an oscillating field. In a Bloch sphere representation, the basis states of the two-level system are placed at opposite poles of a sphere as in Fig. 2.1. These two states are known as longitudinal spin states since they are aligned with the basis states, which are usually the $|\pm z\rangle$ states. The equator of the Bloch sphere represents equal superposition states. These superposition states are referred to as transverse spin states because the spin vector is perpendicular to the quantization axis. For example, if the longitudinal (basis) states are $|\pm z\rangle$, then transverse states are a combination of the $|\pm x\rangle$ and $|\pm y\rangle$ states, where $|\pm x\rangle = \frac{1}{\sqrt{2}}(|+z\rangle \pm |-z\rangle)$ and $|\pm y\rangle = \frac{1}{\sqrt{2}}(|+z\rangle \pm i|-z\rangle)$.

A quantum state is described by a vector on the Bloch sphere and state evolution involves rotations of this Bloch vector. The density matrix representing the state can be written

$$\hat{\rho} = \frac{1}{2} (\hat{I} + \mathbf{M} \cdot \hat{\sigma}), \quad (2.6)$$

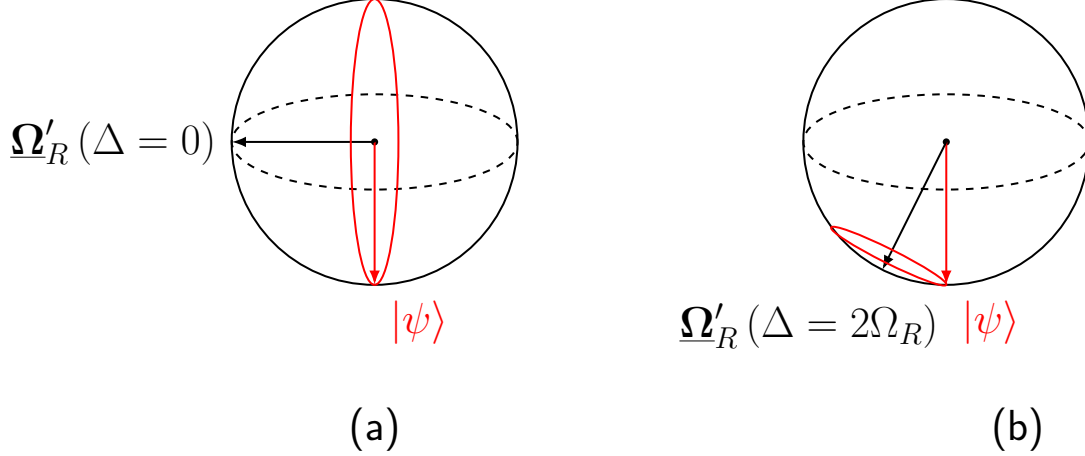


Figure 2.2: Rabi oscillations on the Bloch sphere for two different detunings from resonance. (a) For zero detuning the Bloch vector rotates with full amplitude to the excited state. (b) For a detuning of $\Delta \approx 2\Omega_R$ the Bloch vector rotates near the bottom of the Bloch sphere at a faster rate of $\Omega'_R \approx \sqrt{5}\Omega_R$.

where $\underline{\mathbf{M}} = (M_x, M_y, M_z)$ is the Bloch vector, \hat{I} is the identity operator, and $\hat{\underline{\sigma}} = (\sigma_x, \sigma_y, \sigma_z)$ are the Pauli matrices. During Rabi flopping, the state evolution of the Bloch vector amounts to a rotation about the vector

$$\underline{\Omega}'_R = (\Omega_R \cos(\phi), \Omega_R \sin(\phi), \Delta), \quad (2.7)$$

with ϕ being the relative phase between the spin and the applied oscillating field. Figure 2.2 shows rotations for a resonant pulse and for a pulse that is detuned by $\Delta = 2\Omega_R$.

Ignoring radiative damping, the precession of the Bloch vector during this interaction is

$$\frac{d\underline{\mathbf{M}}}{dt} = \underline{\Omega}'_R \times \underline{\mathbf{M}}, \quad (2.8)$$

where the cross product describes a rotation about $\underline{\Omega}'_R$. Equation 2.8 is a simple description of the state evolution during interaction with an oscillating field, where the precession around $\underline{\Omega}'_R$ is given by the cross product. The evolution of the state when radiative damping is added is obtained by solving the Schrödinger equation for the Hamiltonian in Eqn. 2.1 and modelling the effect of radiative decay by a constant decay rate Γ . Using the rotating wave approximation, the resulting equations are

known as the optical Bloch equations [71]

$$\frac{d\rho_{gg}}{dt} = \frac{i\Omega_R}{2} (\rho_{ge} - \rho_{eg}) + \Gamma\rho_{ee}, \quad (2.9)$$

$$\frac{d\rho_{ee}}{dt} = -\frac{i\Omega_R}{2} (\rho_{ge} - \rho_{eg}) - \Gamma\rho_{ee}, \quad (2.10)$$

$$\frac{d\rho_{ge}}{dt} = -\left(\frac{\Gamma}{2} + i\Delta\right) \rho_{ge} - \frac{i\Omega_R}{2} (\rho_{ee} - \rho_{gg}), \quad (2.11)$$

where ρ_{ij} are matrix elements of the density operator

$$\hat{\rho} = \begin{pmatrix} \rho_{ee} & \rho_{ge}^* \\ \rho_{ge} & \rho_{gg} \end{pmatrix}, \quad (2.12)$$

and Γ is the linewidth of the transition. The optical Bloch equations describe the state evolution of a single spin interacting with the applied field, and all other interactions, collisions, or motion are ignored. This approximation is valid for interaction times that are much shorter than the timescales for these other effects. The optical Bloch equations and Eqn. 2.8 are used in this thesis for modelling the state evolution of a spin-1/2 atom interacting with an applied oscillating field.

2.1.2 Ramsey interferometry

In the previous section, short interaction pulses were presented along with a description of how oscillating fields can be used to alter the quantum state of a two-level system. Information about the two-level system can be extracted through interferometry techniques, where multiple pulses are applied at various times. A specific pulse procedure known as Ramsey interferometry is particularly useful for measuring the energy difference between two states [72].

Ramsey interferometry consists of two short Rabi-interaction pulses separated by a long noninteraction or Ramsey time T . The first pulse prepares the state with some transverse spin and a definite phase. During the Ramsey time, the transverse spin precesses at the Larmor frequency and can accumulate phase relative to the oscillator used to generate the first pulse. The phase is accumulated at the frequency difference, or detuning, between the oscillator and the atomic state. In the Bloch sphere representation this Larmor precession is around the $\hat{\mathbf{z}}$ axis. The second Rabi interaction pulse converts the accumulated phase into a probability distribution for the atom being in the ground or excited state. This distribution can be sampled as a function of time to map out Ramsey fringes that can be used to measure a Ramsey

frequency. This Ramsey frequency represents the detuning between the oscillator frequency and the energy difference between the two states during the Ramsey time.

For spins that are initially in the ground or excited state, $\pi/2$ -pulses are used as the two interaction pulses to maximize the signal. These two pulses rotate the initial ground or excited state to the transverse plane and back. The Rabi-interaction times are then fixed to the pulse time of $t_{\pi/2}$. For atoms initially in the ground state, the probability of an atom being in the excited state after a Ramsey interferometry sequence with $\pi/2$ -pulses, small detuning $\Delta \ll \Omega_R$, and short interaction times $t_{\pi/2} \ll T$ is

$$P_e(T) = \cos^2\left(\frac{\Delta T}{2}\right) = \frac{1}{2}(1 + \cos(\Delta T)). \quad (2.13)$$

The detuning Δ can be extracted from data by sampling the excited state population as a function of time. Using rotations other than $\pi/2$ will lower the measured fringe amplitude since the initial transverse spin component is smaller due to the inefficient pulses. In the work described in this thesis, all Ramsey interferometry is performed with resonant $\pi/2$ -pulses during the interaction time, and during the Ramsey time the oscillator frequency is shifted using frequency shift keying. This process allows for efficient interaction pulses for all Ramsey frequencies and is used in Sections 3.5.2, 3.7, 4.3, and 4.10.

2.1.3 Two-photon spectroscopy

The description presented in Sections 2.1 and 2.1.1 is based on single-photon coupling, but because of the atomic states used in this thesis, all Rabi flopping and Ramsey spectroscopy are performed using two-photon pulses. The procedure for two-photon pulses is functionally the same as for single-photon transitions, except that some formulae need to be modified. An intermediate state is used to couple two spin states to enable a transition that is normally forbidden by selection rules ($\Delta m_F = 0, \pm 1$). The level diagram for two-photon spectroscopy is shown in Fig. 2.3. In the interaction picture, the two-photon interaction Hamiltonian for a three-state system is

$$H_{\text{int}} = \begin{pmatrix} 0 & \frac{\hbar}{2}\Omega_2 e^{i\omega_2 t} & 0 \\ \frac{\hbar}{2}\Omega_2 e^{-i\omega_2 t} & 0 & \frac{\hbar}{2}\Omega_1 e^{i\omega_1 t} \\ 0 & \frac{\hbar}{2}\Omega_1 e^{-i\omega_1 t} & 0 \end{pmatrix}, \quad (2.14)$$

where Ω_1 and Ω_2 are the single-photon Rabi frequencies for each two-state coupling, and ω_1 and ω_2 are the frequencies of the two photons. The wavefunction during the

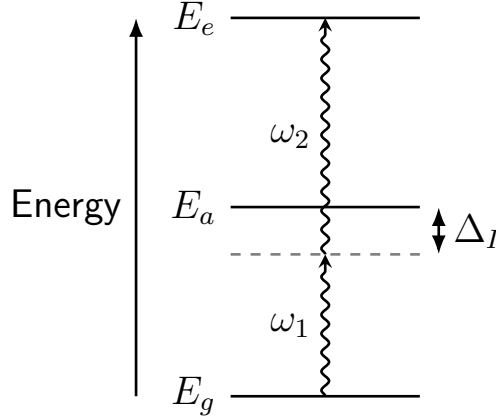


Figure 2.3: Example of an energy level diagram for two-photon spectroscopy that uses an intermediate state (E_a) to couple two states (E_g and E_e). Two photons (wavy lines) with frequencies ω_1 and ω_2 couple the two states through two individual Rabi couplings. The single photon transition is detuned by Δ_I to limit the intermediate state population. The two-photon coupling is useful when the two desired spin states are separated by two units of angular momenta and single-photon transitions between the states are forbidden.

interaction is

$$\begin{aligned}
 |\psi(t)\rangle &= c_g(t)e^{-i\omega_g t}|g\rangle + c_a(t)e^{-i\omega_a t}|a\rangle + c_e(t)e^{-i\omega_e t}|e\rangle \\
 &= c_g(t)e^{-i\omega_g t}|g\rangle + c_a(t)e^{-i(\omega_g + \omega_1 + \Delta_I)t}|a\rangle + c_e(t)e^{-i(\omega_g + \omega_1 + \omega_2 + \delta)t}|e\rangle, \quad (2.15)
 \end{aligned}$$

where the states have energy $\hbar\omega_x$ with $x = \{g, a, e\}$ corresponding to the ground state (g), intermediate state (a), and excited state (e), the detuning from the intermediate state is $\Delta_I = \omega_1 - \omega_a + \omega_g$, and the detuning from the two-photon transition is $\delta = \omega_1 + \omega_2 - \omega_e + \omega_g$.

Solving the time-dependent Schrödinger equation for this Hamiltonian with the atom initially in the ground state, the probability of being in the excited state is

$$P_e(t) = \left(\frac{\Omega_R}{\Omega'_R}\right)^2 \sin^2\left(\frac{\Omega'_R t}{2}\right), \quad (2.16)$$

where $\Omega'_R = \sqrt{\Omega_R^2 + \delta^2}$ [73, 74]. This solution ignores the shift in energy of the intermediate state due to the AC Stark shift from off-resonant light. The solution also assumes the intermediate detuning is large ($\delta \ll \Delta_I$) so the intermediate state is negligibly populated. Under these assumptions, two-photon spectroscopy is effectively

the same as single-photon Rabi flopping, but with a two-photon Rabi frequency of

$$\Omega_R = \frac{\Omega_1 \Omega_2}{2\Delta_I}. \quad (2.17)$$

Just as in the single-photon case, the effective two-photon Rabi frequency Ω'_R can be increased with the detuning δ , leading to a loss in oscillation amplitude as in Eqn. 2.16. However, in two-photon spectroscopy, the Rabi frequency can be modified with the intermediate detuning Δ_I without loss of amplitude. This additional tunability of the Rabi frequency is one small advantage in flexibility when using two-photon spectroscopy, where both cases can modify the Rabi frequency with field amplitude.

2.2 Identical spin rotation effect

The coupling of a single spin to an oscillating field was presented in the previous section. However, in an ultracold gas there can be a million atoms (spins) that are moving within the gas and colliding with other atoms. These collisions with other atoms can significantly alter the single-atom behaviour within the gas. For instance, elastic collisions between atoms lead to exchange of kinetic energy, altering the motion of both atoms. At nondegenerate temperatures the collisions between spins can lead to an exchange of spin through a quantum collision effect known as the identical spin rotation effect (ISRE).

The ISRE can be described in terms of two-body collisions between indistinguishable atoms. This two-body picture is suitable for dilute nondegenerate gases because collisions are infrequent and each collision is independent. At higher densities a mean-field approach can be used to derive a similar spin rotation effect known as the Leggett-Rice effect [75, 76, 77]. The discussion below focusses on the two-body picture of the identical spin rotation effect.

As atoms are cooled to near degeneracy, the spatial extent of their wavefunctions grows with decreasing temperature. The extent of an atomic wavefunction can be quantified with the thermal de Broglie wavelength

$$\lambda_{\text{dB}} = \left(\frac{2\pi\hbar^2}{mk_B T} \right)^{1/2}. \quad (2.18)$$

When the thermal de Broglie wavelength is larger than the relevant collision length, the colliding atoms can be indistinguishable if their spin states are not orthogonal. The relevant collision length here is the hard-core or s-wave scattering length a . The

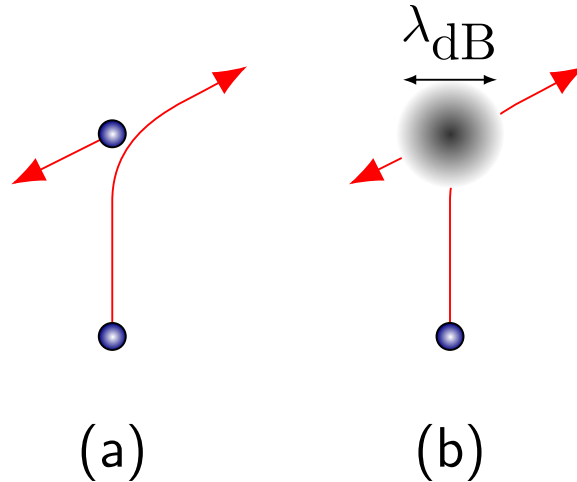


Figure 2.4: Collisions between (a) distinguishable atoms and (b) indistinguishable atoms. The blue spheres represent the atomic s -wave scattering length and the grey shaded region corresponds to the thermal de Broglie wavelength λ_{dB} . At ultracold temperatures, the large thermal de Broglie wavelength makes the colliding atoms indistinguishable and so their wavefunctions must be symmetrized for atom exchange. This indistinguishability leads to the identical spin rotation effect.

indistinguishability of forward or backward scattering events is shown as a cartoon in Figure 2.4. Because of the wavefunction overlap, the atomic wavefunctions must be symmetrized with respect to atom exchange and the net effect of the indistinguishability is a rotation of individual spins about the mean spin. This rotation is known as the ISRE.

As an example of the effect of a collision, the ISRE for two transverse spins separated by some phase is shown in Figure 2.5. After the collision, the outgoing spins have both acquired longitudinal spin components. The ISRE conserves total spin and so equal and opposite amounts of longitudinal spin are created during collisions. For other initial spin states, an ISRE collision could lead to the spins acquiring a larger transverse component instead of a longitudinal component, but the total spin is still conserved. In large spin ensembles, multiple collision events can generate collective spin behaviour that is challenging to predict based on only a few ISRE collision events.

A theoretical discussion to highlight how atom indistinguishability can lead to a spin rotation effect is presented by following the work in Refs. [78, 53, 54, 79, 80]. For a gas of N atoms, the quantum state of the system can be described by an N -atom density matrix $\hat{\rho}_N$, which evolves in time following the Liouville-von Neumann

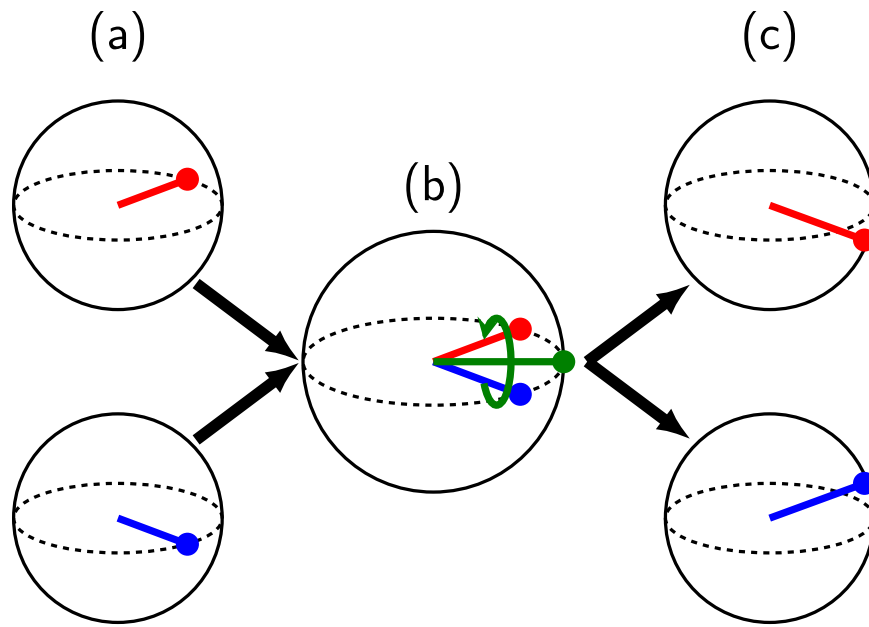


Figure 2.5: Example of the identical spin rotation effect (ISRE) for a collision between two spins, where spins are represented as Bloch spheres. (a) Before the collision the spins are purely transverse vectors separated by a phase. (b) During the collision the spins rotate about their mean spin (green), and the extent of the rotation depends on the strength of the ISRE. (c) The outgoing atoms in this example have opposite longitudinal spin components, because the ISRE conserves total spin.

equation

$$i\hbar \frac{\partial \hat{\rho}_N}{\partial t} = [\hat{H}_N, \hat{\rho}_N]. \quad (2.19)$$

The symbols with a hat, such as $\hat{\rho}_N$, denote operators, and $[\hat{A}, \hat{B}] = \hat{A}\hat{B} - \hat{B}\hat{A}$ is the commutator. The N-atom Hamiltonian is assumed to be of the form

$$\hat{H}_N = \sum_{i=1}^N \hat{H}_i + \frac{1}{2} \sum_{i \neq j} \hat{V}_{ij}, \quad (2.20)$$

where $\hat{H}_i = \frac{\hat{p}_i^2}{2m} + \hat{V}_{\text{ext}}$ is the single-atom Hamiltonian that includes kinetic and external potential terms, and \hat{V}_{ij} is the short-range interaction potential between two atoms. For large N , Equation 2.19 is impractical to solve because of the large number of degrees of freedom. The number of degrees of freedom can be reduced by assuming the gas is dilute, so that individual atoms are approximately independent. This approximation is known as the Boltzmann property [78]

$$\hat{\rho}_N = \prod_{i=1}^N \hat{\rho}_i, \quad (2.21)$$

which is another way of saying that the quantum state of each atom is independent.

Using Eqn. 2.21 and taking the trace of Eqn. 2.19 over all indices except for one gives the single atom evolution

$$i\hbar \frac{\partial \hat{\rho}_1}{\partial t} - [\hat{H}_1, \hat{\rho}_1] = \left. \frac{\partial \hat{\rho}_1}{\partial t} \right|_{\text{collisions}}, \quad (2.22)$$

where the evolution of the state due to collisions is

$$\left. \frac{\partial \hat{\rho}_1}{\partial t} \right|_{\text{collisions}} = \text{Tr}_2 \left([\hat{V}_{12}, \hat{\Omega} \hat{\rho}_1 \hat{\rho}_2 \hat{\Omega}^\dagger] \right). \quad (2.23)$$

Here Tr_2 is the trace over the second indice corresponding to a second atom, and $\hat{\Omega}$ is the Møller collision operator [81]

$$\hat{\Omega} \equiv \lim_{\tau \rightarrow -\infty} \exp \left[i \left(\frac{\hat{p}_1^2}{2m} + \frac{\hat{p}_2^2}{2m} + \hat{V}_{\text{ext}} + \hat{V}_{12} \right) \tau / \hbar \right] \exp \left[-i \left(\frac{\hat{p}_1^2}{2m} + \frac{\hat{p}_2^2}{2m} + \hat{V}_{\text{ext}} \right) \tau / \hbar \right], \quad (2.24)$$

where \hat{p}_i represents the momentum of the i^{th} atom, \hat{V}_{ext} represents the external potential, and \hat{V}_{12} represents the interaction potential. The Møller operator can be used in scattering theory when the interaction potential asymptotically vanishes at large

positive or negative times, which it does for short-range collisions. The Møller operator connects the free-motion states with the states after a collision, such that the matrix $\hat{\Omega}\hat{\rho}_1\hat{\rho}_2\hat{\Omega}^\dagger$ represents the density matrix of the two spins after a collision event. The use of the Møller operator is valid for dilute gases where the collision time is small compared to the free-motion time. Equation 2.23 can be generalized to include spin exchange as

$$\left. \frac{\partial \hat{\rho}_1}{\partial t} \right|_{\text{collisions}} = \text{Tr}_2 \left(\frac{1 + \epsilon \hat{P}_{\text{ex.}}}{\sqrt{2}} \left[\hat{V}_{12}, \hat{\Omega}\hat{\rho}_1\hat{\rho}_2\hat{\Omega}^\dagger \right] \frac{1 + \epsilon \hat{P}_{\text{ex.}}}{\sqrt{2}} \right), \quad (2.25)$$

where $\hat{P}_{\text{ex.}}$ is the exchange operator, and ϵ is +1 for bosons and -1 for fermions. Equation 2.25 describes the state evolution of atom 1 due to a collision with atom 2.

For an ensemble of classical atoms the density distribution describes the probability of an atom having a given position and momentum. The quantum analog of this classical distribution is a Wigner quasiprobability distribution, which is a probability distribution of an atom having a certain position, momentum, and spin state. The Wigner transform maps a single-atom density matrix evolution to an N-atom probability density in a momentum-position-spin phase space. The two-atom Wigner transform of the density operator $\hat{\rho}$ is

$$\hat{W}(\underline{\mathbf{R}}, \underline{\mathbf{r}}, \underline{\mathbf{P}}, \underline{\mathbf{p}}) = (2\pi\hbar)^{-6} \int d^3 K \int d^3 \kappa \left[e^{i\mathbf{K}\cdot\underline{\mathbf{R}}} e^{i\kappa\cdot\underline{\mathbf{r}}} \langle \underline{\mathbf{K}}_+, \underline{\mathbf{k}}_+ | \hat{\rho} | \underline{\mathbf{K}}_-, \underline{\mathbf{k}}_- \rangle + c.c. \right], \quad (2.26)$$

where the position and momentum of the two atoms are $(\underline{\mathbf{R}}, \underline{\mathbf{P}})$ and $(\underline{\mathbf{r}}, \underline{\mathbf{p}})$, $K_\pm = \frac{\mathbf{P}}{\hbar} \pm \frac{\mathbf{K}}{2}$, $k_\pm = \frac{\mathbf{p}}{\hbar} \pm \frac{\kappa}{2}$, and *c.c.* denotes the complex conjugate terms. Here we can see that the Wigner function is the Fourier transform of the density operator.

Taking the Wigner transform of Eqn. 2.25 and then performing a Groenewold gradient expansion [82, 83] to zero order in gradients gives

$$\begin{aligned} \left. \frac{\partial \hat{\rho}(\underline{\mathbf{r}}, \underline{\mathbf{p}})}{\partial t} \right|_{\text{collisions}} = & - \int d^3 q \frac{q}{m} \left\{ \left[\sigma_T(k) \hat{\rho}(\underline{\mathbf{r}}, \underline{\mathbf{p}}) f(\underline{\mathbf{r}}, \underline{\mathbf{p}}_2) - \int d^2 k' \sigma_k(\theta) \hat{\rho}(\underline{\mathbf{r}}, \underline{\mathbf{p}}') f(\underline{\mathbf{r}}, \underline{\mathbf{p}}'_2) \right] \right. \\ & + \frac{\epsilon}{2} \left(\nu \tau_{\text{fwd.}}^{\text{ex.}}(k) \left[\hat{\rho}(\underline{\mathbf{r}}, \underline{\mathbf{p}}), \hat{\rho}(\underline{\mathbf{r}}, \underline{\mathbf{p}}_2) \right] - \int d^2 k' \nu \tau_k^{\text{ex.}}(\theta) \left[\hat{\rho}(\underline{\mathbf{r}}, \underline{\mathbf{p}}'), \hat{\rho}(\underline{\mathbf{r}}, \underline{\mathbf{p}}'_2) \right] \right. \\ & \left. \left. + \int d^2 k' \sigma_k^{\text{ex.}}(\theta) \left(\left\{ \hat{\rho}(\underline{\mathbf{r}}, \underline{\mathbf{p}}), \hat{\rho}(\underline{\mathbf{r}}, \underline{\mathbf{p}}_2) \right\} - \left\{ \hat{\rho}(\underline{\mathbf{r}}, \underline{\mathbf{p}}'), \hat{\rho}(\underline{\mathbf{r}}, \underline{\mathbf{p}}'_2) \right\} \right) \right) \right\}. \quad (2.27) \end{aligned}$$

Here the primed coordinates denote the momenta of scattered particles, where the integral over k' is only performed over the angular components, and the azimuthal angle of the scattered particle is $\theta = \tan^{-1}(k'_y/k'_x)$. Additionally, the anti-commutator

is $\{\hat{A}, \hat{B}\} = \hat{A}\hat{B} + \hat{B}\hat{A}$, the atomic distribution $f(\mathbf{r}, \mathbf{p}) = \text{Tr}_S\{\hat{\rho}(\mathbf{r}, \mathbf{p})\}$ is obtained by taking the trace over the spin, the parameterized momenta are $\mathbf{q} = 2\hbar\mathbf{k}$, $\mathbf{p}_2 = \mathbf{p} - \mathbf{q}$, $\mathbf{p}' = \mathbf{p} - (\mathbf{q}/2) + \hbar k \hat{k}'$, $\mathbf{p}'_2 = \mathbf{p} - (\mathbf{q}/2) - \hbar k \hat{k}'$, and \mathbf{k} is the collision wavevector over which the integration is performed. The differential and total cross sections that describe the classical elastic collisions are

$$\sigma_k(\theta) = (4\pi^4 m^2 / \hbar^4) |T(\mathbf{k}, \mathbf{k}')|^2 \quad (2.28)$$

$$\sigma_T(k) = \int d^2 k' \sigma_k(\theta), \quad (2.29)$$

where the T matrix for s-wave scattering is

$$T(\mathbf{k}, \mathbf{k}') = T(\mathbf{k}) = \frac{\hbar^2}{2\pi^2 m} (a - ika^2). \quad (2.30)$$

The s-wave scattering length a is assumed to be the same for both spin states, which is approximately true for rubidium-87 because $a_{11} = 100.4a_0$, $a_{22} = 95.5a_0$ and $a_{12} = 98.1a_0$ [84]. Here, a_0 is the Bohr radius, a_{11} corresponds to collisions between two $|F = 1, m_F = -1\rangle$ spins, a_{22} corresponds to collisions between two $|F = 2, m_F = 1\rangle$ spins, and a_{12} corresponds to collisions between one $|F = 1, m_F = -1\rangle$ spin and one $|F = 2, m_F = 1\rangle$ spin. See Fig. 3.6 for rubidium-87 states. Because of the isotropic nature of s-wave scattering, the primed coordinate can be dropped since only the scattering length a and collision wavevector k are needed to describe the collision when $ka \ll 1$. This small ka expansion is valid for s-wave collisions when the s-wave scattering length is much smaller than the thermal de Broglie wavelength. The quantities $\tau_{\text{fwd.}}^{\text{ex.}}(k)$, $\sigma_k^{\text{ex.}}(\theta)$, and $\tau_k^{\text{ex.}}(\theta)$ that appear in Eqn. 2.27 represent the spin exchange cross sections are

$$\tau_{\text{fwd.}}^{\text{ex.}}(k) = \left(\frac{-8\pi^3 m}{\hbar^2 k} \right) \text{Re}\{T(-\mathbf{k}, \mathbf{k})\} = -\frac{4\pi a}{k} \quad (2.31)$$

and

$$\sigma_k^{\text{ex.}}(\theta) - i\tau_k^{\text{ex.}}(\theta) = \left(\frac{4\pi^4 m^2}{\hbar^4} \right) T(-\mathbf{k}, \mathbf{k}') T^*(\mathbf{k}, \mathbf{k}') = a^2(1 + k^2 a^2). \quad (2.32)$$

Equation 2.27 includes the details of both the classical collisions and the ISRE in a relatively dense format. The first two terms that scale with $\sigma_T(k)$ and $\sigma_k(\theta)$ represent the distinguishable interaction terms describing classical scattering between atoms. The following four terms that depend on ϵ describe the collisional effect of

indistinguishable atoms. The terms with $\tau_{\text{fwd.}}^{\text{ex.}}$ and $\tau_k^{\text{ex.}}$ describe the contribution of the forward and lateral exchange scattering to the ISRE. The $\sigma_k^{\text{ex.}}$ terms consist of anti-commutators, which do not alter the quantum state, instead those terms describe exchange effects that modify the total and lateral cross-sections.

To explicitly show the spin rotation part of the ISRE, the density operator can be simplified to

$$\hat{\rho} = \frac{1}{2} \left(f(\mathbf{r}, \mathbf{p}) + \mathbf{m}(\mathbf{r}, \mathbf{p}) \cdot \hat{\sigma} \right), \quad (2.33)$$

for spin-1/2 atoms, where $f(\mathbf{r}, \mathbf{p})$ is the atomic density distribution and $\mathbf{m}(\mathbf{r}, \mathbf{p})$ is the spin density distribution. Substituting this spin-1/2 density matrix into Eqn. 2.27 and only considering the forward scattering spin exchange term gives

$$\int d^3q \frac{q}{m} \frac{\epsilon}{2} \tau_{\text{fwd.}}^{\text{ex.}} \left[\hat{\rho}(\mathbf{r}, \mathbf{p}), \hat{\rho}(\mathbf{r}, \mathbf{p}_2) \right] = \frac{\epsilon}{2} \int d^3q \frac{q}{m} \tau_{\text{fwd.}}^{\text{ex.}} \mathbf{m}(\mathbf{r}, \mathbf{p}) \times \mathbf{m}(\mathbf{r}, \mathbf{q}). \quad (2.34)$$

This simplifies to

$$\frac{\epsilon}{2} \int d^3q \frac{q}{m} \tau_{\text{fwd.}}^{\text{ex.}} \mathbf{m}(\mathbf{r}, \mathbf{p}) \times \mathbf{m}(\mathbf{r}, \mathbf{q}) = \frac{\epsilon}{2} \frac{4\pi\hbar^2 a}{m} \mathbf{m}(\mathbf{r}, \mathbf{p}) \times \int d^3q \mathbf{m}(\mathbf{r}, \mathbf{q}), \quad (2.35)$$

where the quantity $\int d^3q \mathbf{m}(\mathbf{r}, \mathbf{q})$ is proportional to the local spin $\mathbf{M}(\mathbf{r})$. Equation 2.35 shows that the forward scattering contribution to the ISRE amounts to a rotation of spin about the local, or mean, spin $\mathbf{M}(\mathbf{r})$. While only the forward scattering case was shown for simplicity, lateral scattering also contributes to the ISRE as shown in Ref. [53]. Note that the ISRE for colliding bosons and fermions only differs by the value of ϵ in Eqn. 2.35, which only changes the sign of the effect.

The strength of the ISRE is greatest at the coldest temperatures, as shown by dropping the first order term of the low energy limit ($ka \ll 1$) of the cross-sections in Eqns. 2.28, 2.29, 2.31, and 2.32 to find

$$\sigma_k(\theta) = a^2 \quad (2.36)$$

$$\sigma_T = 4\pi a^2 \quad (2.37)$$

$$\tau_{\text{fwd.}}^{\text{ex.}} \rightarrow \infty \quad (2.38)$$

$$\tau_k^{\text{ex.}} \rightarrow 0. \quad (2.39)$$

The ISRE forward scattering cross-section $\tau_{\text{fwd.}}^{\text{ex.}}$ tends to infinity at low energies, while the rest of the cross sections approach a finite number. The large forward scattering cross-section shows that the ISRE can be strong at ultracold temperatures and can

provide significant spin exchange interactions. The strength of the ISRE can also be quantified relative to the classical collision timescale as

$$\mu = \frac{gn}{\hbar}\tau = \frac{\pi\hbar^2}{4a\sqrt{\pi k_B T m}}, \quad (2.40)$$

where $g = 4\pi\hbar^2 a/m$ represents a mean-field coupling constant, the density is n , the temperature is T , and the radially averaged elastic collision time is

$$\tau = \left(16a^2 n \sqrt{\pi k_B T/m}\right)^{-1}. \quad (2.41)$$

A large value of μ corresponds to a stronger ISRE compared to classical elastic scattering. At the temperatures explored in this thesis, such as $T = 650$ nK, the relative ISRE strength is $\mu \approx 8$. This means the ISRE can be a strong effect during spin diffusion, and in Section 6.1 the ISRE is shown to be the dominant effect.

2.3 Spin diffusion theory

Spin diffusion in a dilute nondegenerate 1D ultracold gas can be described with a 1D quantum Boltzmann equation. This Boltzmann equation can be derived from the Liouville-von Neumann equation (Eqn. 2.19) following an approach similar to that described in the previous section. This time the Wigner transform of Eqn. 2.19 in its entirety is computed so that we include the kinetic motion, an external trapping potential, external Rabi coupling, and the collisions. The detailed steps involved in this derivation can be found in Refs. [78, 53, 54, 79, 80, 85]. The coupled quantum Boltzmann equations describing the diffusion of the atomic density distribution $f = f(\mathbf{r}, \mathbf{p}, t)$ and the spin density distribution $\mathbf{m} = \mathbf{m}(\mathbf{r}, \mathbf{p}, t)$ in 3D are

$$\frac{\partial f}{\partial t} + \frac{\mathbf{p}}{m_{\text{atomic}}} \cdot \nabla_r f - \nabla U_n \cdot \nabla_p f - \frac{\hbar}{2} \nabla \Omega_n \cdot \nabla_p m_i = \left. \frac{\partial f}{\partial t} \right|_{\text{collisions}}, \quad (2.42)$$

and

$$\begin{aligned} \frac{\partial \mathbf{m}}{\partial t} + \frac{\mathbf{p}}{m_{\text{atomic}}} \cdot \nabla_r \mathbf{m} - \nabla U_n \cdot \nabla_p \mathbf{m} \\ - \frac{\hbar}{2} \nabla \Omega_n \cdot \nabla_p f - \mathbf{\Omega} \times \mathbf{m} = \left. \frac{\partial \mathbf{m}}{\partial t} \right|_{\text{collisions}}, \end{aligned} \quad (2.43)$$

where the index i is summed over the three spin components, m_{atomic} denotes the atomic mass, $n(\underline{\mathbf{r}}, t) = \int d^3p f(\underline{\mathbf{r}}, \underline{\mathbf{p}}, t)/(2\pi\hbar)^3$ is the atomic density, and $\underline{\mathbf{M}}(\underline{\mathbf{r}}, t) = \int d^3p \underline{\mathbf{m}}(\underline{\mathbf{r}}, \underline{\mathbf{p}}, t)/(2\pi\hbar)^3$ is the spin density. The center of mass potential is $U_n(\underline{\mathbf{r}}, t) = U_{\text{ext}}(\underline{\mathbf{r}}) + 3gn(\underline{\mathbf{r}}, t)/2$, and the spin rotation term that includes the Rabi coupling term $\underline{\Omega}$ (Section 2.1.1) and the ISRE is

$$\underline{\Omega}_n(\underline{\mathbf{r}}, t) = \underline{\Omega}(\underline{\mathbf{r}}, t) + \frac{g}{\hbar}\underline{\mathbf{M}}(\underline{\mathbf{r}}, t). \quad (2.44)$$

Finally, the classical collision integrals that $\left. \frac{\partial \underline{\mathbf{m}}}{\partial t} \right|_{\text{collisions}}$ represents are reproduced in Appendix B.

Equations 2.42 and 2.43 can be uncoupled by assuming that the coupling field only generates a local Larmor precession such that the Rabi vector is $\underline{\Omega} = (0, 0, U_{\text{diff}})$, where U_{diff} represents the relative detuning across the cloud and is called the differential potential. Uncoupling these equations also requires that the terms that scale with the spatial gradient of the density are neglected, which are the third and fourth terms in Eqns. 2.42 and 2.43. Both of these approximations are satisfied in a dilute gas, or in a gas with uniform density so that the spatial gradient of the density is small, and if the spins are not externally coupled via Rabi pulses. The decoupled 3D Boltzmann equation that results is

$$\frac{\partial \underline{\mathbf{m}}}{\partial t} + \frac{\underline{\mathbf{p}}}{m_{\text{atomic}}} \cdot \nabla \underline{\mathbf{m}} - \nabla U_{\text{ext}} \cdot \nabla_p \underline{\mathbf{m}} - \underline{\Omega} \times \underline{\mathbf{m}} = \left. \frac{\partial \underline{\mathbf{m}}}{\partial t} \right|_{\text{collisions}}. \quad (2.45)$$

The quantum Boltzmann equation describing spin diffusion in 1D is obtained by averaging over the two radial directions. In the work described in this thesis, the radial dimensions of the atomic gas are significantly (~ 37 times) smaller than the axial direction. Because of this geometry, there are effectively no spin dynamics in the radial direction. The radial trap frequency is faster than any spin dynamics or collision rates, and so the radial dynamics are averaged out. The 1D quantum Boltzmann equation that describes the diffusion of spin in a weakly-interacting nondegenerate ultracold gas is [85]

$$\frac{\partial \underline{\mathbf{m}}(z, p, t)}{\partial t} + \frac{p}{m_{\text{atomic}}} \frac{\partial \underline{\mathbf{m}}(z, p, t)}{\partial z} - \frac{\partial U_{\text{ext}}}{\partial z} \frac{\partial \underline{\mathbf{m}}(z, p, t)}{\partial p} - \underline{\Omega} \times \underline{\mathbf{m}}(z, p, t) = \left. \frac{\partial \underline{\mathbf{m}}(z, p, t)}{\partial t} \right|_{\text{collisions}}. \quad (2.46)$$

The first term in Eqn. 2.46 is the dynamical term that describes how the spin density distribution evolves in time. The next two terms are the classical drift and force terms, where $U_{\text{ext}} = \frac{1}{2}m_{\text{atomic}}(\omega_z^2 z^2 + \omega_\rho^2 \rho^2)$ is the magnetic trapping potential that is quadratic in the axial z and radial ρ directions. The Larmor precession and ISRE are described by the fourth term (Section 2.2), where $\underline{\Omega}\hbar = U_{\text{diff}}\hat{\mathbf{z}} + g\underline{\mathbf{M}}(z, t)$ corresponds to the precession of spin around the differential potential $U_{\text{diff}}\hat{\mathbf{z}}$ and the local spin $\underline{\mathbf{M}}(z, t) = \frac{1}{2\pi\hbar} \int dp \underline{\mathbf{m}}(z, p, t)$. The term on the right describes the time evolution of the remainder of the collision terms, which are the elastic scattering terms. In the relaxation time approximation the effect of classical collisions can be written as

$$\left. \frac{\partial \underline{\mathbf{m}}(z, p, t)}{\partial t} \right|_{\text{collisions}} \approx -\tau^{-1}(z) [\underline{\mathbf{m}}(z, p, t) - f(p)\underline{\mathbf{M}}(z, t)], \quad (2.47)$$

where $f(p) = \lambda_{\text{dB}} \exp(-p^2/2p_0^2)$ is the equilibrium atomic distribution in momentum space with $p_0 = \sqrt{m_{\text{atomic}}k_B T}$, and $\tau(z) = (16a_{12}^2 n_0(z) \sqrt{\pi k_B T/m})^{-1}$ is the radially averaged mean collision time.

The 1D quantum Boltzmann equation in Eqn. 2.46 can be expressed in other spin state coordinate systems, which can be used to describe the diffusion of specific spin components (see Appendix C). In cylindrical coordinates, evolution of the transverse amplitude and phase evolution are obtained, mapping directly to the experimental observables (see Section 3.5.2). This particular coordinate system simplifies the effect of the differential potential, but does not make the Boltzmann equation tractable for an analytic solution in any nontrivial case.

2.4 Simulations of spin diffusion

The quantum Boltzmann equation (Eqn. 2.46) can be simulated numerically by using a finite-difference technique. The results of these simulations can be used to guide the collection of data and for comparisons between data and theory. The simulations are especially useful for exploring new ideas, because it is not always obvious how certain experimental parameters change spin diffusion. The simulation process follows the procedure outlined in Ref. [85], which applies a Crank-Nicolson alternating direction implicit technique to numerically step the spin density distribution through time. In the work described in this thesis, a dynamic time step was added to increase the numerical reliability of simulation results.

2.4.1 Alternating-direction-implicit method

Applying the Euler method to the quantum Boltzmann equation yields

$$\begin{aligned} \frac{\underline{\mathbf{m}}(z, p, t_{i+1}) - \underline{\mathbf{m}}(z, p, t_i)}{\Delta t} = & -\frac{p}{m} \delta_z \underline{\mathbf{m}}(z, p, t_i) + m\omega_z^2 \delta_p \underline{\mathbf{m}}(z, p, t_i) \\ & + \frac{1}{\hbar} (U_{\text{diff}} \hat{\mathbf{z}} + g \underline{\mathbf{M}}(z, t_i)) \times \underline{\mathbf{m}}(z, p, t_i) \\ & - \frac{1}{\tau} (\underline{\mathbf{m}}(z, p, t_i) - f(p) \underline{\mathbf{M}}(z, t_i)), \end{aligned} \quad (2.48)$$

where the subscripts i and $i+1$ are the relative times at $t_i = t_0 + i\Delta t$, $\delta_{z,p}$ indicates a finite backward difference on the position z or momentum p , and Δt is the time step. The finite backward difference for position z is defined as

$$\delta_z \underline{\mathbf{m}}(z, p, t_i) = \frac{\underline{\mathbf{m}}(z, p, t_i) - \underline{\mathbf{m}}(z - \Delta z, p, t_i)}{\Delta z}, \quad (2.49)$$

where the difference is explicitly taken at the known time t_i . This type of finite difference is called an explicit finite difference. While the Euler method is easy to compute, it is not numerically stable for all conditions [85, 86].

The stability of the numerical solution is improved by using the Crank-Nicolson method, which is typically unconditionally stable for all time steps Δt [85, 86]. This stability arises from the separation of each time step into two time steps where only one step needs to be unconditionally stable [86]. During each time step the finite difference is alternated between one that is explicit in position (and implicit in momentum) and one that is explicit in momentum (and implicit in position). This is known as the alternating direction implicit (ADI) method. The implicit differentiation requires solving a tri-diagonal matrix because there are multiple position or momentum terms, such as the terms at position $z - \Delta z$, z , and $z + \Delta z$ after an implicit difference in position. Applying ADI to the discretized Boltzmann equation gives the following two time steps:

$$\begin{aligned} \frac{\underline{\mathbf{m}}(z, p, t_{i+1/2}) - \underline{\mathbf{m}}(z, p, t_i)}{\Delta t/2} = & -\frac{p}{m} \delta_z \underline{\mathbf{m}}(z, p, t_{i+1/2}) + m\omega_z^2 \delta_p \underline{\mathbf{m}}(z, p, t_i) \\ & + \frac{1}{\hbar} (U_{\text{diff}} \hat{\mathbf{z}} + g \underline{\mathbf{M}}(z, t_i)) \times \underline{\mathbf{m}}(z, p, t_i) \\ & - \frac{1}{\tau} (\underline{\mathbf{m}}(z, p, t_i) - f(p) \underline{\mathbf{M}}(z, t_i)), \end{aligned} \quad (2.50)$$

and

$$\begin{aligned}
\frac{\underline{\mathbf{m}}(z, p, t_{i+1}) - \underline{\mathbf{m}}(z, p, t_{i+1/2})}{\Delta t/2} &= -\frac{p}{m} \delta_z \underline{\mathbf{m}}(z, p, t_{i+1/2}) + m\omega_z^2 \delta_p \underline{\mathbf{m}}(z, p, t_{i+1}) \\
&+ \frac{1}{\hbar} \left(U_{\text{diff}} \hat{\mathbf{z}} + g \underline{\mathbf{M}}(z, t_{i+1/2}) \right) \times \underline{\mathbf{m}}(z, p, t_{i+1/2}) \\
&- \frac{1}{\tau} \left(\underline{\mathbf{m}}(z, p, t_{i+1/2}) - f(p) \underline{\mathbf{M}}(z, t_{i+1/2}) \right). \quad (2.51)
\end{aligned}$$

The first of these equations is implicit in position and the second is implicit in momentum, where the distinction is found by the time subscript used in each step. An explicit time step uses the current values to compute the finite difference, while an implicit time step uses the next computed value to compute the finite difference. An initial condition for the spin and atomic distribution is prepared, and then these equations are iterated until the time span for the simulation is sufficient to be compared to data.

2.4.2 Dynamic time stepping

The “unconditional” stability of the Crank-Nicolson technique appears to break down when the differential potential U_{diff}/h is 100 Hz or larger. At these differential potentials, the transverse spin rotates too far in a single time step and the simulation becomes numerically unstable. The time step size could be manually lowered to counteract the unstable numerics, but then computation time is increased. We introduced a dynamic time stepping procedure as a quick fix for this numerical instability, where we limit large changes in any spin component by reducing the size of the time step.

The size of each dynamic time step is calculated so that the spin density distribution is changed by a fraction of the current spin density distribution. The dynamic time step at time t_i is fixed for both ADI steps and calculated based on the first ADI step that is implicit in position. The dynamic time step $\Delta\tau$ is calculated so that each time step only changes the spin density distribution by a relative amount η , satisfying

$$\frac{\Delta m_k(z, p)}{\Delta\tau} \frac{1}{m_k(z, p)} \leq \eta. \quad (2.52)$$

Here $m_k = \underline{\mathbf{m}} \cdot \hat{\mathbf{k}}$ are the three components of the spin density distribution m_x, m_y, m_z , where $\hat{\mathbf{k}} = \{\hat{\mathbf{x}}, \hat{\mathbf{y}}, \hat{\mathbf{z}}\}$. The change in the spin component during the implicit position step is $\Delta m_k(z, p)/\Delta\tau$ (Eqn. 2.50), and spin density distribution at the current time step is $m_k(z, p)$. The mean of each spin component over position z and momentum p

is computed and the minimum time step of the three spin components that satisfies Eqn. 2.52 is

$$\Delta\tau = \eta \min_k \left(\frac{\sum_{z,p} |m_k(z,p)|}{\sum_{z,p} |\Delta m_k(z,p)|} \right). \quad (2.53)$$

The minimum is taken between the three spin components labelled with the subscript k . The relative change of the spin density distribution η is typically set to 0.05 so that on average the spin components change by 5% or less each time step. For large differential potentials of 100 Hz or higher, the spin components precess quickly and dynamic time stepping reduces the time steps, slowing down the calculations. However, the smaller time step should ensure the phase only wraps a small fraction of the way around the Bloch sphere during each step leading to reliable numerics. Even though dynamic time stepping improves the simulation quality and reliability, the numerical simulation is still not unconditionally stable, and for extremely large differential potentials η may need to be tweaked further.

2.5 Spin-dependent and independent potentials

Spin-independent potentials, like the magnetic trapping potential for our two pseudo-spin states, can be used to shape the atomic density profile since all spins experience the same potential or force at the same position. However, spin-dependent potentials provide an opportunity to create separate potentials for each of the two spin states. One spin state could be tightly confined while the other spin state is weakly confined or even anti-trapped by a strong spin-dependent potential. In addition to separate trapping potentials, spin-dependent potentials shift the local Larmor precession frequency by modifying the energy difference between spin states. Shifting either the spin-dependent trapping potential or the local Larmor precession frequency can modify spin diffusion, and in Section 6.1 weak spin-dependent potentials are used to modify the local Larmor precession.

Typically, the simplest method to create a spin-dependent potential is with a magnetic field. For a spin with magnetic moment $\underline{\mu}$ in a magnetic field \mathbf{B} , the energy of the spin state is shifted by $\Delta U_{\text{magnetic}} = -\underline{\mu} \cdot \mathbf{B}$. However, the pseudo-spin states used in this thesis have nearly the same magnetic moment so that they are equally trapped by the magnetic field. So for these pseudo-spin states, a magnetic field creates a spin-independent trapping potential that determines the shape of the 1D density profile.

Since magnetic fields cannot be easily controlled to generate arbitrary patterns with arbitrary strengths, all spin-dependent potentials used in this thesis are created using the oscillating electric field in laser light. This oscillating field couples each spin state to a higher energy state, creating an AC Stark shift of varying magnitude and sign. The AC Stark shift, also called the Autler-Townes effect or dipolar shift, arises from the interaction between the oscillating induced atomic dipole and the electric field. The energy of the atom is modified by $\Delta U = -\frac{1}{2}\langle \mathbf{p} \cdot \mathbf{E} \rangle$, where $\langle \cdot \rangle$ denotes a time average and $\mathbf{p} = \alpha(\omega)\mathbf{E}$ is the dipole moment of the atom that is induced by the oscillating field. The dynamic atomic polarizability is given by [87, 88, 89]

$$\alpha(\omega) = \frac{e^2}{m\omega_0^2 - \omega^2 - i\omega\Gamma}, \quad (2.54)$$

where ω_0 is the resonant frequency and Γ is the natural linewidth. The dynamic polarizability drastically increases near a resonance and changes sign on the opposite side of the resonance. Spin-dependent potentials can be tuned by controlling the detuning of the oscillating field. The difficulty with these dipolar interactions is in finding the strongest coupling to the higher state without actually exciting the transition. The smaller the detuning the larger the spin-dependent potential, but the more likely it is for an atom to be excited to an unwanted state.

For alkali atoms in the vicinity of the D₁ and D₂ lines the dipolar interaction is given by [87]

$$U_{\text{dipole}}(\mathbf{r}) = \frac{\pi c^2 \Gamma}{2\omega_0^3} \left(\frac{2 + P g_F m_F}{\Delta_{2,F}} + \frac{1 - P g_F m_F}{\Delta_{1,F}} \right) I(\mathbf{r}), \quad (2.55)$$

where ω_0 is the atomic transition frequency, $\Delta_{2,F}$ and $\Delta_{1,F}$ are the detunings from the D2 and D1 lines, $P = 0, \pm 1$ is for linearly and circularly polarized light, g_F is the Landé factor, m_F is the Zeeman sublevel, and $I(\mathbf{r})$ is the intensity of the radiation field. Simplifying this equation in the limit of large detunings from the D1 and D2 lines, so that $\Delta_{1,F} = \Delta_{2,F} = \Delta$, the dipolar interaction is

$$U_{\text{dipole}}(\mathbf{r}) = \frac{3\pi c^2 \Gamma}{2\omega_0^3 \Delta} I(\mathbf{r}). \quad (2.56)$$

The dipolar potential is tunable with the laser intensity I and laser detuning Δ . Alternatively, for detunings near the D2 transition $\Delta_{1,F} \gg \Delta_{2,F}$ the contribution

from the D1 line can be ignored and the dipolar potential is then given by

$$U_{\text{dipole}}(\mathbf{r}) = \frac{\pi c^2 \Gamma}{2\omega_0^3} \left(\frac{2 + P g_F m_F}{\Delta_{2,F}} \right) I(\mathbf{r}). \quad (2.57)$$

The latter is the approach used going forward.

For two spin states labelled 1 and 2, the spin-independent (common) and spin-dependent (differential) potentials are $U_{\text{common}} = U_2 + U_1$ and $U_{\text{diff}} = U_2 - U_1$, where U_1 and U_2 are the dipolar shifts experienced by atoms in each spin state interacting with the same radiation field. In terms of Eqn. 2.57 this becomes

$$U_{\text{common/diff}}(\mathbf{r}) = \frac{\pi c^2 \Gamma}{2\omega_0^3} \left(\frac{2 + P g_F^{(2)} m_F^{(2)}}{\Delta_{2,F}^{(2)}} \pm \frac{2 + P g_F^{(1)} m_F^{(1)}}{\Delta_{2,F}^{(1)}} \right) I(\mathbf{r}), \quad (2.58)$$

where the superscripts indicate the spin-state specific parameters. The common and differential modes scale with detunings as $(\Delta_{2,F}^{(1)} \pm \Delta_{2,F}^{(2)}) / \Delta_{2,F}^{(1)} \Delta_{2,F}^{(2)}$.

The three different types of dipolar shifts are illustrated with two-state energy levels in Fig. 2.6. Far red- or blue-detuned frequencies shift the energy of both states in the same direction. Detuning between the spin states shifts the energy levels in opposite directions. Moving the detuning closer to a resonance can increase the overall differential potential but will start to transfer atoms to the excited state.

Coupling atoms to higher energy states can excite the atoms, and so one should be careful of photon scattering rates whenever dipolar shifts are used. The scattering rate corresponding to Eqn. 2.57 is

$$\Gamma_{\text{sc}}(\mathbf{r}) = \frac{\pi c^2 \Gamma^2}{2\hbar\omega_0^3} \left(\frac{2}{\Delta_{2,F}^2} \right) I(\mathbf{r}). \quad (2.59)$$

Notice that the scattering rate scales as I/Δ^2 while the interaction potential in Eqn. 2.58 scales as I/Δ . Far-detuned frequencies reduce the scattering rate faster than the dipolar shift. So for a dipolar shift of a single atomic state, large detunings are always better if the intensity is available to compensate. Spin-dependent potentials require frequencies near resonance, but the largest detunings possible still give the lowest scattering rates.

The optimal detuning minimizes the scattering rate while also maximizing the interaction potential. For spin-independent potentials, large detunings combined with the largest possible laser intensity are optimal. For spin-dependent potentials, the optimal detuning to minimize scattering rate is found when the laser frequency is

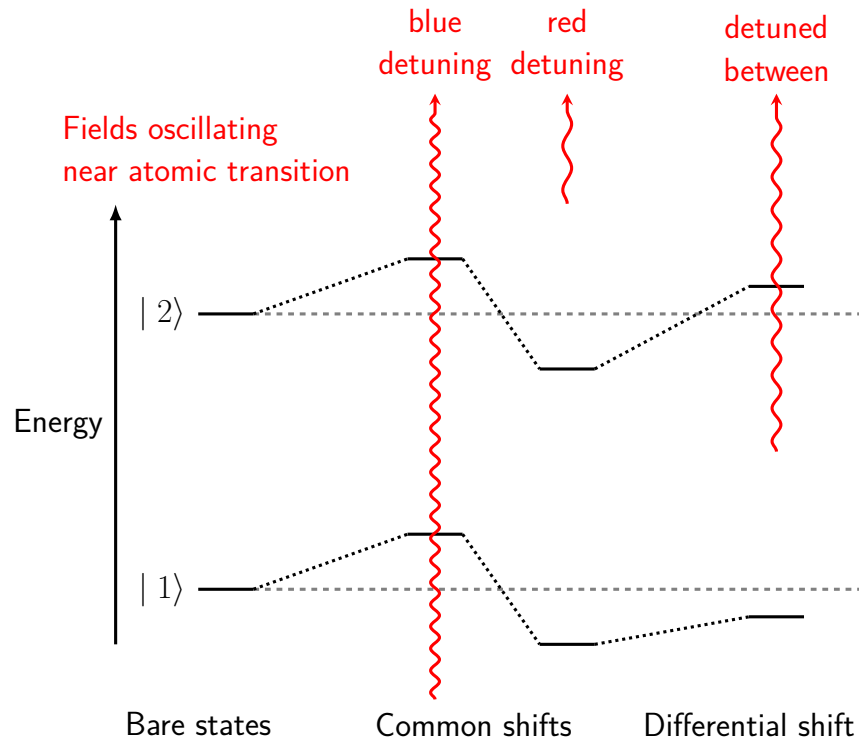


Figure 2.6: Dipolar energy shifts caused by coupling to a higher-energy atomic state. Examples are shown for the case of two coupled hyperfine states ($|1\rangle$ and $|2\rangle$). The common mode shifts can either raise or lower the average energy, corresponding to blue and red detunings, respectively. A coupling frequency that is between the two states creates a differential energy shift raises the energy of one state and lowers the energy of the other spin state.

between the two states, such that $\Delta_{2,F}^{(1)} = -\Delta_{2,F}^{(2)}$. This thesis uses this optimal detuning configuration to limit photon scattering rates when generating spin-dependent potentials that modify spin diffusion in Chapter 6.

This chapter discussed the theoretical frameworks that describe how to control, measure, and modify spin diffusion. Rabi pulses are used for control of spin states, while Ramsey spectroscopy is used for measuring differential potentials and transverse spin. The identical spin rotation effect manifests from the indistinguishability of atoms at ultracold temperatures. A dynamical description of spin diffusion can be obtained in the quantum Boltzmann equation and provides insight into spin diffusion processes. By numerically simulating this equation, the experiment can be guided by the simulation results or the simulation can be used to compare with spin diffusion data. Lastly, the generation of spin-independent and spin-dependent potentials was discussed, where spin-dependent potentials are used to modify spin diffusion by altering the local Larmor precession.

Chapter 3

Apparatus and procedures

This chapter provides an overview of the apparatus and procedures used to study one-dimensional (1D) spin diffusion in an ultracold gas of ^{87}Rb . The first half of this chapter describes how ultracold gases are formed and detected using the apparatus. The second half of this chapter discusses the methods for preparing spin states and manipulating the effective magnetic field.

3.1 Experimental overview

The design of the apparatus used in this thesis work is based on the apparatus used in H. J. Lewandowski's doctoral thesis work for studying coherences and correlations in a BEC [84]. A ^{87}Rb vapor is laser cooled and trapped with a magneto-optical trap (MOT) in a vacuum. The atoms are then transferred to an ultra-high vacuum (UHV) cell at pressures of order 10^{-11} Torr by translating the magnetic field coils of the MOT on a motorized track. Inside the UHV cell the loss of trapped atoms due to collisions with the background gas is minimal and lifetimes longer than 100s of seconds are observed. The McGuirk group's implementation of Lewandowski's apparatus is straightforward and robust, requiring minimal daily care. This section provides a more detailed description of the two main parts of the apparatus: the magneto-optical trap and the UHV science cell.

3.1.1 Magneto-optical trap

The magneto-optical trap (MOT) is formed inside a glass vacuum cell that is filled with rubidium vapor. Rubidium vapor is produced in the MOT cell by dispensers sitting inside the vacuum. The alkali metal dispensers contain a stable rubidium salt mixed with a getter material that facilitates evaporation of rubidium atoms and

capture of excess gases. Once the evaporation process has started, the dispensers will continuously evaporate rubidium atoms into our MOT cell, until they run out of atoms to evaporate. The evaporation rate is controlled by the temperature of the dispensers. The evaporation rate is increased by heating up the dispensers with electric current through wires that are connected to a power supply outside the vacuum. The current running through the dispensers is continuously operated at ~ 3.4 Amps to ensure a nearly constant evaporation rate of rubidium atoms into the MOT cell.

The ^{87}Rb vapor is laser-cooled using Doppler cooling, where the motion of the atom can increase or decrease the frequency of a photon in the rest frame of the atom. To Doppler cool atoms, a laser is red-detuned from an atomic transition so that only the atoms moving toward the beam will be resonant with the photons. The moving atom absorbs a resonant photon and also receives a small momentum kick in the direction the photon was travelling, with magnitude $\hbar k$, where $k = 2\pi/\lambda$ is the wavenumber and λ is 780.23 nm for this work. Only the atoms moving towards the beam will be resonant and so the momentum kick slows the atom down. The now-excited atom will spontaneously emit a photon and receive another momentum kick of $\hbar k'$ in a random direction, where $k < k'$. The emitted photon has a higher wavenumber and carries away the kinetic energy the atoms loses. Since spontaneous emission is isotropic the average momentum kick after many emissions is zero. The net momentum change of the atom absorbing and then emitting is $\hbar k$ in the opposite direction of travel. This reduction in the momentum of the atom is equivalent to cooling, and when performed on an ensemble of atoms the temperature of the ensemble is reduced. Figure 3.1 shows the cooling process in one dimension for a single photon and atom going through a Doppler cooling cycle.

The procedure in Fig. 3.1 only provides cooling to atoms moving to the right. To cool atoms travelling to the left and the right simultaneously, a second laser beam is applied that travels in the opposite direction, cooling the atoms moving to the left. This counterpropagating laser is resonant with atoms moving to the left because the laser frequency adds with the Doppler shift of the left-moving atom. Doppler cooling in 3D replicates the 1D process in the two other dimensions by using a total of six laser beams, three pairs of counterpropagating beams. The coldest temperature that Doppler cooling can reach is limited by the fluctuations of the momentum of an atom due to spontaneous emission. This temperature is called the Doppler limit $T_{\text{Doppler}} = \frac{\hbar\Gamma}{2k_B}$, which is 145 μK for ^{87}Rb , about one million times colder than room temperature. Note that in experimentally realized MOTs there exists sub-Doppler

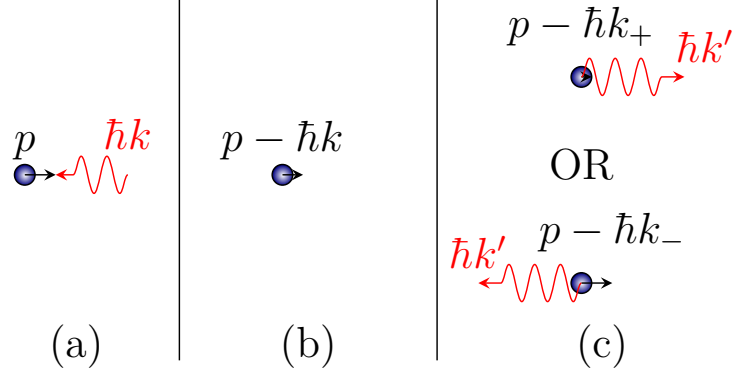


Figure 3.1: Doppler cooling example in one dimension. (a) An atom with momentum p is moving towards a photon with momentum $\hbar k$ that is Doppler shifted to be resonant. (b) The atom absorbs the photon and is slowed down by the absorbed photon momentum $\hbar k$. (c) The atom will spontaneously emit a photon, which in 1D must be either to the left or the right. If emitted to the left the momentum of the atom is reduced by $\hbar k_-$, but if emitted to the right the momentum of the atom is reduced by $\hbar k_+$, where $k_{\pm} = k \pm k'$. This example only cools atoms moving to the right, a second laser is added to cool atoms moving to the left. By repeating this cooling process many times, the average change in momentum of an atom is $\hbar k$ per photon scattered.

cooling forces that allow the MOT to reach temperatures lower than the Doppler limit.

Doppler cooling is effective at cooling atoms, but it does not spatially confine them and the cooled atoms can travel out of the laser beam. The atoms can be spatially trapped near the center of the Doppler cooling beams by adding a pair of magnetic field coils, called the MOT coils. The MOT coils are arranged in an anti-Helmholtz configuration (Fig. 3.2) to create a large magnetic field gradient at the center. This magnetic field gradient Zeeman shifts the energy of the magnetic sublevels m_F so that as an atom moves away from the center it becomes resonant with the laser. An atom that is resonant with the laser undergoes absorption and emission of photons, which ultimately pushes the atom back to the magnetic field zero.

Figure 3.3 shows an energy diagram for a one-dimensional MOT [71]. The cooling laser is red detuned by δ from the zero-field transition. As an atom moves away from the center it becomes resonant with the $\Delta m = \pm 1$ transition and scatters σ^{\pm} polarized photons, which pushes the atom back towards the MOT center. For three dimensions, this process is repeated in three orthogonal directions each with σ^{\pm} polarized laser beams and the MOT coils provide a field gradient in all directions. In Fig. 3.3 the ground state is shown to be in the $m_F = 0$ sublevel, but the cooling transition for

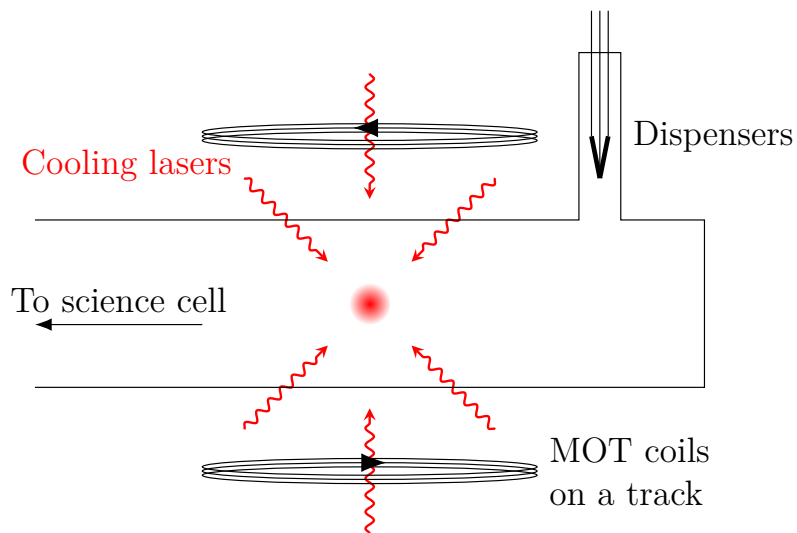


Figure 3.2: The MOT vacuum cell used to trap and cool one billion ^{87}Rb atoms to $\sim 145 \mu\text{K}$ using six counterpropagating beams (red). Each laser beam is antiparallel to one other beam and orthogonal to the rest. The MOT coils are used to localize the cold cloud with magnetic field gradients that shift the energy of the atomic states. The arrows on the coils signify that the current in these coils flow in opposite directions. These coils are attached to a track that translates the MOT cloud to the science cell for further cooling and experiments. The dispensers fill the MOT cell with rubidium vapor

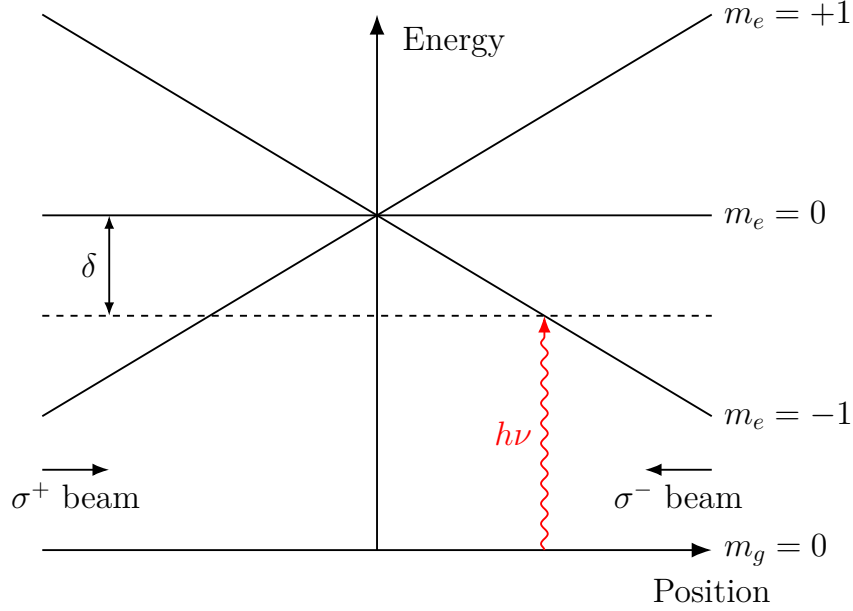


Figure 3.3: The magnetic field generated by the MOT coils shifts the energy of Zeeman sublevels in the excited state m_e . As an atom moves away from the center of the trap to the right, the $m_e - m_g = \Delta m = -1$ transition becomes resonant with the σ^- beam and the atom will scatter more σ^- photons, pushing it back to the center. The magnetic field direction is flipped on the left side and $\Delta m = +1$ transitions are resonant. While this figure is for one dimension, extending to three dimensions requires six laser beams instead of two.

^{87}Rb is $5S_{1/2} |F = 2\rangle \rightarrow 5P_{3/2} |F = 3\rangle$, meaning that the ground state could occupy a nonzero Zeeman level. Since the cooling transition is always a $\Delta J = +1$ transition, the excited state will have one more magnetic sublevel than the ground state. The $F = 2$ state has five magnetic sublevels, while the $F = 3$ state has seven sublevels. Even though m_g is not necessarily zero, the MOT will localize all magnetic sublevels of the $F = 2$ hyperfine state because only the change in sublevel $\Delta m = \pm 1$ is relevant.

The relevant ^{87}Rb electronic states are in Fig. 3.4 and shows the cooling and repump transitions used to create a MOT. The MOT uses transitions between the $5S_{1/2}$ and $5P_{3/2}$ fine structure states, known as D_2 transitions. The quantum number for the hyperfine states in the $5S_{1/2}$ and $5P_{3/2}$ manifolds are denoted with F and F' , respectively. When loading the MOT with atoms, the cooling laser is frequency locked at the $F = 2$ to $F' = 3$ transition with a red detuning of about 20 MHz. While the $F' = 3$ state can only decay into $F = 2$ due to selection rules, the cooling laser will excite some atoms to $F' = 2$ and about one in 1,000 atoms then decay into the

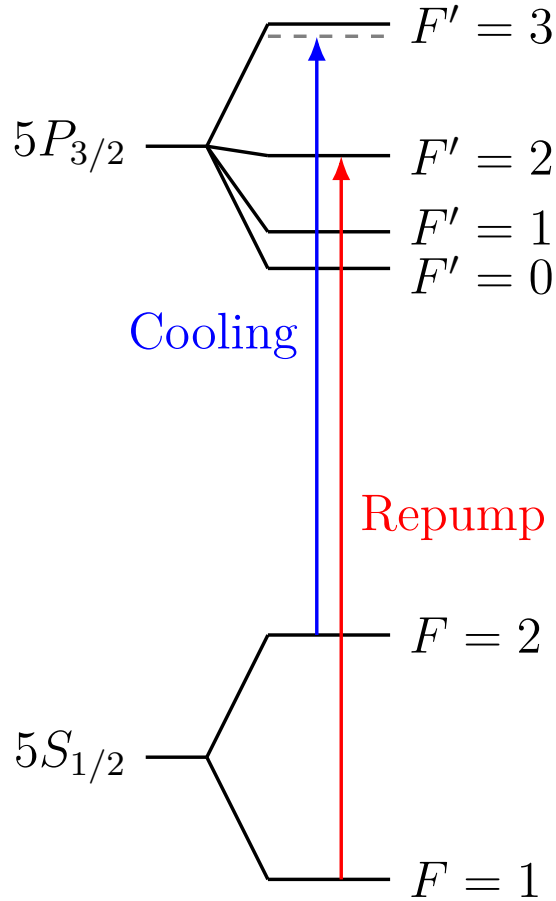


Figure 3.4: Cooling and repump transitions used in laser cooling rubidium atoms. Both are at wavelengths close to 780.23 nm. The cooling laser is detuned from the $F = 2 \rightarrow F' = 3$ transition and the repump laser is resonant with the $F = 1 \rightarrow F' = 2$ transition.

$F = 1$ ground state. A repumper laser excites those atoms in $F = 1$ to $F' = 2$ until they decay back into $F = 2$ where the cooling laser is effective.

A lens is used to image the fluorescence from atoms in the MOT onto a photodiode. When this signal reaches a set level, usually after 1 – 10 seconds of loading, the atoms are then prepared for transfer to the science cell. The sequence of operations needed to transfer the atoms uses a compressed MOT (CMOT) to reduce the size of the cloud, optically pumping to the magnetically trappable state, and then magnetically trapping the atoms and moving the coils. The atoms should occupy the smallest possible volume before turning on the magnetic trap otherwise atoms far from the trap center will acquire too much magnetic potential energy and heat the cloud. The CMOT stage reduces the size of the cloud by reducing the radiation pressure at the

center of the cloud. This is done by detuning the cooling laser by 50 MHz and lowering the repump intensity. Detuning the cooling laser reduces the photon scattering rate of the $F = 2$ atoms and the reduction in repump intensity lowers the amount of time an atom is in the $F = 2$ state. The CMOT stage lasts about 10 ms.

Next, the atoms are optically pumped into the $F = 1$ state by turning off the repump laser and waiting 1 ms for the atoms to all reach the $F = 1$ state. The optical pumping used here does not select what sublevel is occupied so the optically pumped cloud is a mixture of $m_F = -1, 0, +1$ sublevels. Of the $F = 1$ sublevels, only the $|F = 1, m_F = -1\rangle$ state is magnetically trappable since its energy increases with larger magnetic field. When the magnetic field coils are ramped up to produce higher field gradients to trap atoms in the $m_F = -1$ state, atoms in the other sublevels will be lost since they are not trapped. The MOT coils are ramped to a high field gradient, trapping the $m_F = -1$ atoms tightly so that they are able to be transported. The MOT coils are mounted on a track that physically transports the MOT coils using a stepper motor. The coils move 53.4 cm, transporting the cloud of atoms through a 2 cm wide vacuum cell to reach the science cell. Here the atoms are released from the MOT coils and caught with the coils that are part of the science cell.

3.1.2 The science cell

The science cell is a glass cell that has ultra-high vacuum pressures to lengthen cloud lifetime by limiting collisions with background gases. Surrounding the glass cell is a hybrid Ioffe-Pritchard trap (Figure 3.5) made with two permanent magnets and four magnetic field coils. The magnets are glued into a machined block of boron-nitride, which is transparent to microwaves. The permanent magnets are oriented with the same magnetic pole facing each other to create a quadrupolar magnetic field. This orientation provides a strong magnetic field gradient in the two radial directions. Inside the boron-nitride block, the two pairs of magnetic field coils control the axial trap geometry. The inner pair are called the bias coils and the outer are the pinch coils. The bias coils are in Helmholtz configuration and provide a uniform magnetic field. The combination of the magnetic fields from the pinch and bias coils sets the magnetic field at the center of the trap, known as the bias field. Calibration of the bias field is discussed in Section 4.3. The pinch coils provide an axial magnetic field gradient that confines atoms in the axial direction. The magnetic confinement in the axial direction is typically 37 times weaker than the trapping in the two radial directions from the permanent magnets. Atoms released from the MOT coils into the

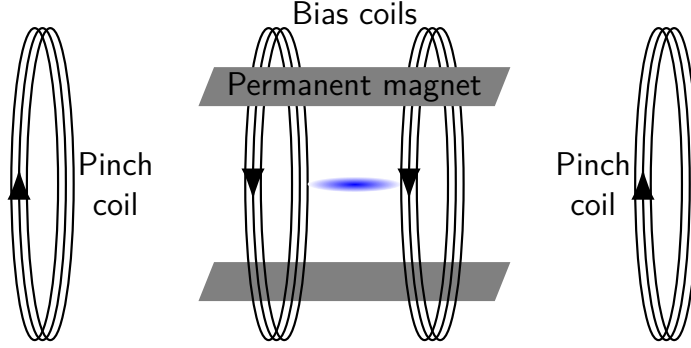


Figure 3.5: Hybrid Ioffe-Pritchard trap consisting of two permanent magnets and four magnetic field coils to create a quasi-1D cloud geometry. The outer coils confine the cloud axially, while the inner coils are in a Helmholtz configuration and control the bias field. Arrows on the coils indicate the direction of current flow. The blue cloud indicates the position of the atomic cloud; the size of the cloud is not drawn to scale.

hybrid Ioffe-Pritchard trap will form a pencil-shaped cloud in the center, with an aspect ratio of 37 to 1.

The pencil-shaped trap geometry of the science cell is quasi-1D. The confinement in the radial direction is strong enough that the corresponding dynamics are much faster than in the axial direction. This permits one to average over the dynamics in the radial direction. In quasi-1D geometries atoms are free to move past each other in the axial direction by translating in the radial direction. In a truly 1D geometry this is not possible since the atoms would form a chain and have to exchange places to move past one another. To quantify the difference between these two geometries, we can compare the radial harmonic oscillator length $a_{\text{ho}} = \sqrt{\hbar/m\omega_{\rho}}$ to the radial width of the density distribution ρ_0 . The harmonic oscillator length characterizes the spatial extent of the available motional modes that atoms can occupy, while the density distribution describes how far atoms travel from the trap center. To reach a 1D geometry the radial width should be much smaller than the harmonic oscillator length $\rho_0 \ll a_{\text{ho}}$. In our trap, the radial width of the density distribution is about seven times larger than the harmonic oscillator length, so atoms have enough space to go around neighbouring atoms to avoid collisions.

Immediately after catching the $|F = 1, m_F = -1\rangle \equiv |1, -1\rangle$ atoms in the science cell's pencil-shaped trap, the MOT coils move back to the MOT cell, and evaporation of the cloud is used to reach colder temperatures. Evaporation is performed by applying radio frequency fields to flip the spins of the most energetic atoms, leaving them in an untrapped state, so that they are released from the trap and carry away

above-average kinetic energy. The atoms remaining in the cloud rethermalize to a lower temperature, and the process is repeated until the cloud is sufficiently cold or until all of the atoms have been evaporated from the trap. Evaporation can be a lengthy process that is limited by rethermalization timescales, which scale with the elastic scattering rate

$$\gamma_{\text{elastic}} = n(8\pi a^2)v_{\text{rel}}, \quad (3.1)$$

where n is the density, $a = 100.4(1)a_0$ is the s-wave scattering length of the $|1, -1\rangle$ state [90, 91, 92, 93], and

$$v_{\text{rel}} = \sqrt{\frac{16k_B T}{3\pi m}} \quad (3.2)$$

is the relative velocity. Our evaporation protocol uses nine stages, where each stage incrementally ramps the frequency of the applied radio frequency (RF) from 60 MHz to 2 MHz using exponential steps. Further discussion of evaporation can be found in the calibration section (Section 4.2).

Atom losses from the science cell trap are primarily due to inelastic collisions. Long cloud lifetimes require minimizing these inelastic collisions by limiting the one-, two-, and three-body loss rates. One-body losses occur as a result of collisions with background gas, which are limited by the ultra-high vacuum in the science cell. Two-body losses are significantly suppressed in spin-polarized gases that occupy the maximally polarized magnetic sublevel, i.e. $m_F = \pm F$. An upper bound on the two-body loss coefficient is $1.6 \times 10^{-16} \text{ cm}^3/\text{s}$ [84]. Lastly, three-body losses are dominant at densities of 10^{13} cm^{-3} or higher, where molecule formation can occur more often since collisions of three atoms are more likely. For the $|1, -1\rangle$ state of ^{87}Rb , the loss rate coefficients are $4.3(1.8) \times 10^{-29} \text{ cm}^6\text{s}^{-1}$ and $5.8(1.9) \times 10^{-30} \text{ cm}^6\text{s}^{-1}$ for a noncondensed and condensed cloud, respectively [94]. Short evaporation times need to be used to limit the three-body losses at densities higher than 10^{13} cm^{-3} .

After evaporation, the cloud temperature is around 100–1,000 nK and the density is about $1 - 4 \times 10^{13} \text{ cm}^{-3}$. The density and temperature are tunable through the MOT load parameters and the final RF evaporation frequency. Larger MOT loads give rise to higher densities and lower RF frequencies yield colder clouds. For a fixed MOT load and final RF evaporation frequency, the density and temperature of the cloud in the science cell varies from shot-to-shot by about 5%. While this variation can be challenging to work with, the simple tunability of temperature and density make it easy to explore spin diffusion under different conditions.

3.2 Spin profile preparation

All spin preparation in this work is performed using cloud-wide two-photon pulses that couple the $|F = 1, m_F = -1\rangle \equiv |1\rangle$ and $|F = 2, m_F = 1\rangle \equiv |2\rangle$ states as shown in Fig. 3.6. A microwave field applied at frequency $\nu_{\mu\text{W}}$ provides the first photon with a single-photon detuning from the intermediate state of $\Delta_{\text{IM}} \sim 70$ kHz below the $|1, -1\rangle \rightarrow |2, 0\rangle$ transition. An RF field applied at frequency ν_{RF} is tuned so that the two-photon transition is on resonance. Typical microwave and RF frequencies used are 6,831 MHz and 3.126 MHz, respectively. A microwave waveguide that terminates near the science cell is fed with the microwave signal to irradiate the atoms. These fields penetrate the boron-nitride that surrounds the science cell, enabling them to interact with atoms inside. The RF fields are supplied by a coil antenna placed near the atoms, between the boron-nitride and the vacuum cell. All two-photon pulses are performed by applying these two fields simultaneously for a fixed time period. Typical Rabi frequencies are around 4 kHz, but because we use a two-photon transition there is flexibility to change the Rabi frequency by changing the intermediate detuning Δ_{IM} .

The evolution of the spin state during the two-photon transition can be controlled by applying a spatially varying two-photon detuning across the cloud (Section 2.5). The two-photon detuning is controlled with a spatially varying spin-dependent potential that is generated using a spatially varying laser intensity and the AC Stark effect. As a first step toward controlling the initial spin state of atoms in clouds, a rectangular piece of aluminum was used to block half of an expanded laser beam as shown in Fig. 3.7. The aluminum is painted black to minimize scattered light. The initially collimated laser beam is expanded using two pairs of lenses, one pair of spherical lenses and one pair of cylindrical lenses. Another spherical lens is used to image the aluminum mask plane onto the atoms. With this masking method, one half of the cloud is illuminated while the other is not. For a laser wavelength of 780.23 nm, the laser light provides an AC Stark shift and a detuning δ of around 150 kHz or about $40\Omega_R$.

With half of the cloud detuned, a cloud-wide π -pulse will only transfer the $|1\rangle$ state atoms that are resonant to the $|2\rangle$ state. This corresponds to the atoms in the half of the cloud that is not illuminated. The width of the detuning profile characterizes how the detuning varies from maximum to zero. The width is given by the quality of the optical focus and is further limited by diffraction. Inside this width of the detuning profile, where the intensity of the light varies, the cloud-wide pulse will rotate the

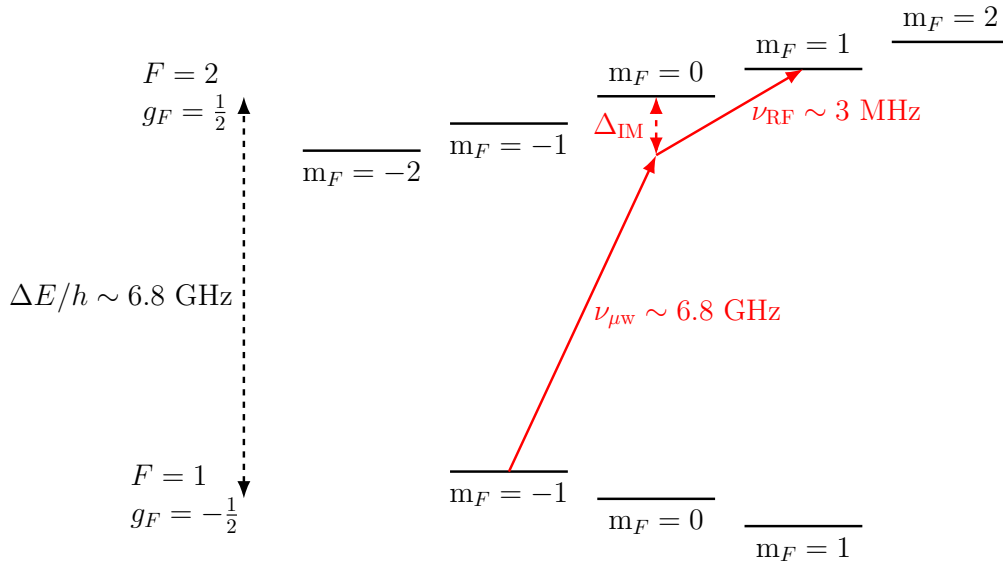


Figure 3.6: The $5S_{1/2}$ ground state manifold of ^{87}Rb , not to scale, which is comprised of two hyperfine states and their corresponding Zeeman sublevels. The red lines show the frequencies used for two-photon spectroscopy between the $|F = 1, m_F = -1\rangle \equiv |1\rangle$ and $|F = 2, m_F = 1\rangle \equiv |2\rangle$ states. A microwave $\nu_{\mu W}$ and radio frequency ν_{RF} photon are used to couple these states together. The intermediate detuning Δ_{IM} is exaggerated since the detuning is usually 70 kHz red detuned and the $m_F = -1$ state represents a 2.3 MHz energy shift from the $m_F = 0$ state.

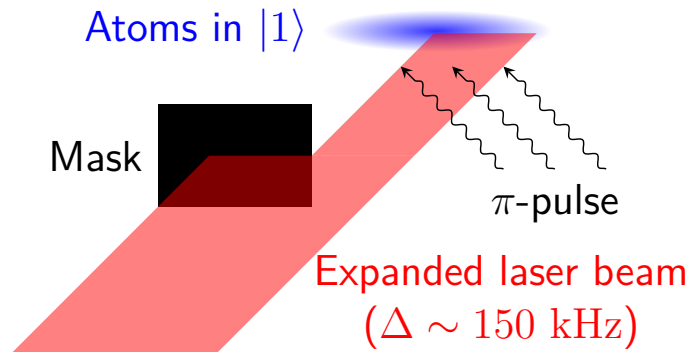


Figure 3.7: Schematic of the masking technique used to apply a large detuning ($\Delta \sim 150$ kHz) to one side of the cloud but not the other. A cloud-wide π -pulse will transfer the atoms that are not detuned to the excited state, but will not alter the spin state of the atoms that are detuned. This process is used to generate a helical spin profile.

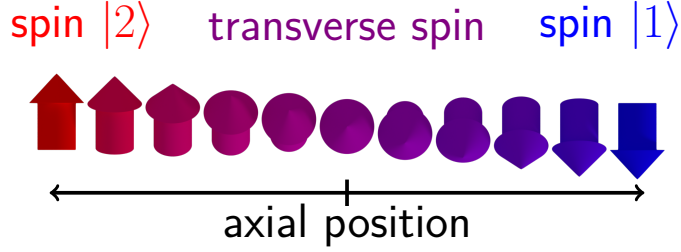


Figure 3.8: The helical spin structure shown with spin vectors has two spin domains spatially separated with an region of transverse spin in between the domains. The spin vector across the cloud starts as spin $|2\rangle$ on the left and rotates around to spin $|1\rangle$ on the right to form a helical shape. This helical spin structure conserves total spin across the spin domains.

spins around the Bloch sphere and convert $|1\rangle$ to transverse spin located between the $|2\rangle$ and $|1\rangle$ domains. The resulting spin profile is known as a helical spin domain because the spin vectors rotate around like a helix as in Fig. 3.8. The width of the transverse spin region is set by the quality of focus of the lens that images the plane of the aluminum mask and is typically $140 \mu\text{m}$ full-width at half-max (FWHM). This masking technique is used for spin preparation in all results presented in this thesis. However, since the aluminum mask does not allow for arbitrary initial spin profiles, it was replaced with a digital micromirror device (DMD) to prepare any initial 1D spin profile. The DMD is discussed in Section 3.8.

3.3 Imaging atoms

Detection of the atomic cloud is performed by optically imaging the plane of the atoms with a camera. These images can be used to extract physical quantities that describe the atomic distribution or spin profile.

3.3.1 Experimental procedure

The atomic states used during imaging are shown in Fig. 3.9. The imaging process starts with atoms in state $|1\rangle$ being transitioned to the $|F = 2, m_F = -2\rangle$ state via adiabatic rapid passage (ARP). The ARP efficiently transfers the entire atomic cloud population, even though the resonance frequency varies across the cloud because of the magnetic trapping potential. The ARP is performed by applying a microwave field at a single frequency and sweeping the bias magnetic field through resonance of all atoms in the cloud, converting all of the atoms in the state $|1\rangle$ to the $|F = 2, m_F = -2\rangle$

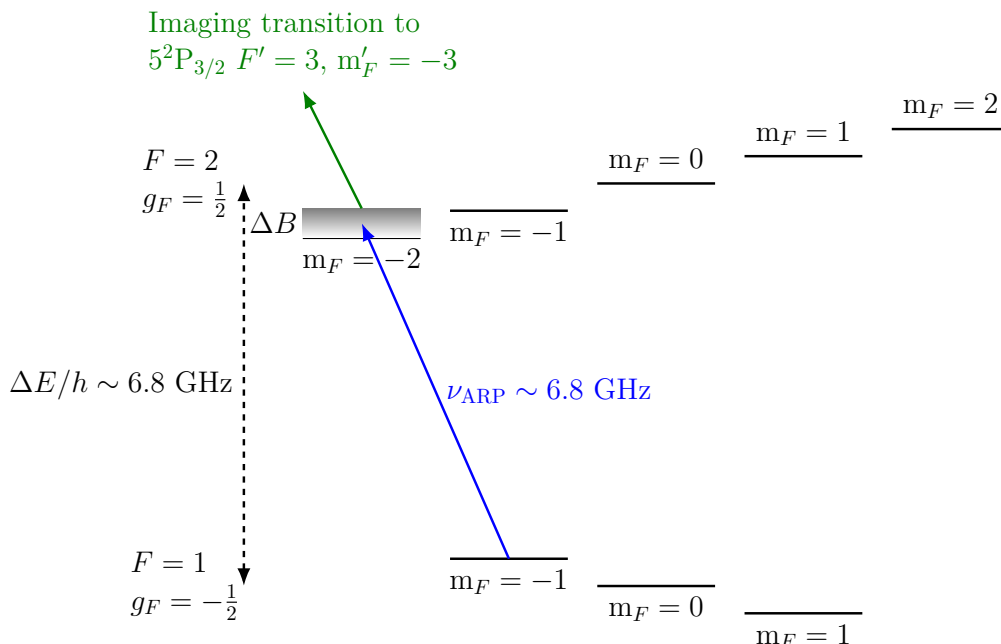


Figure 3.9: Imaging procedure for the $|F = 1, m_F = -1\rangle$ state in the $^{87}\text{Rb } 5S_{1/2}$ manifold. Adiabatic rapid passage (ARP) is performed with a microwave frequency ν_{ARP} and a sweeping of the magnetic field by ΔB through resonance of the $|F = 1, m_F - 1\rangle \rightarrow |F = 2, m_F = -2\rangle$ transition. With atoms in the maximally polarized $|F = 2, m_F = -2\rangle$ state, a cycling transition to the $5P_{3/2}$ state is used to image these atoms through absorption. This process efficiently images only the atoms that were initially in the $|F = 1, m_F = -1\rangle$ state.

state. The ARP does not affect atoms that were initially in state $|2\rangle$, so those atoms remain in the $|2\rangle$ state. Atoms in state $|2\rangle$ minimally scatter the probe light, and so they are not observed during absorption imaging.

After the ARP procedure, the cloud is expanded for 1 – 3 ms in the magnetic trap that is now an anti-trapping potential for atoms in the $|F = 2, m_F = -2\rangle$ state. The expansion of the cloud is performed quickly to spread the atoms out radially and prevent saturation of the detector. To prevent atoms from falling under the influence of gravity, a shim coil is used to apply a magnetic field gradient that approximately cancels the gravitational potential for the $|F = 2, m_F = -2\rangle$ atoms. After expansion, the bias field is ramped to about 100 G over 120 μs . Ramping the bias field to this higher bias field flattens out the magnetic field potential so that all atoms in the expanded cloud are resonant with the probe laser. In addition, the other magnetic

sublevels of ^{87}Rb are further separated from the probe transition frequency for the $|F = 2, m_F = -2\rangle$ state. See Refs. [84, 95] for further details.

A probe laser illuminates the expanded cloud of atoms and drives the cycling transition $|F = 2, m_F = -2\rangle \rightarrow |F' = 3, m'_F = -3\rangle$ to scatter as many photons as possible in an 80 μs image acquisition time. A nearby gradient index lens images the probe light and some of the scattered photons onto an electron multiplying charged-coupled device (EMCCD) camera. This imaging lens collects nearly all of the unscattered probe light and about 3% of the scattered photons. Ideally, none of the scattered photons are collected for absorption imaging. Unfortunately, a small fraction of scattered photons will always be collected by the imaging lens because the photons are scattered isotropically. The collected probe and scattered light is used to perform absorption imaging, and the absorption images that the camera collects are read out to a computer for processing. The imaging procedure described here is destructive. Atoms are released from the trap and their quantum state is destroyed. After every imaging sequence the experiment must start over from the MOT stage.

3.3.2 Image processing

The intensity of the probe light after passing through the atomic cloud is given by the Beer-Lambert law, $I = I_0 \exp(-OD)$, where I_0 is the incident intensity and OD is the optical density of the cloud. The light remaining after absorption is imaged onto the EMCCD camera along with two additional images taken immediately after the atom image. These two additional images are referred to as the light and dark images. The light image has no atoms present during exposure, but the probe light is still on. The light image measures the peak intensity and variations of the probe beam. The dark image is also taken with no atoms, but now the probe is turned off during the exposure. This image provides a measure of the dark currents, bias, and background scattered light in the imaging process. The atom, light and dark images are combined with the Beer-Lambert law to obtain the optical density for each detector pixel

$$OD_{\text{meas}} = \ln\left(\frac{I_0}{I}\right) = \ln\left(\frac{I_{\text{light}} - I_{\text{dark}}}{I_{\text{atoms}} - I_{\text{dark}}}\right). \quad (3.3)$$

The probe light used for imaging typically has off-resonant components that are not absorbed by the atoms. These non-resonant components of the probe light can come from misalignment of the polarization from the quantization axis, background scattered light, or additional off-resonant frequency modes in the laser spectrum.

Since the collected light is never entirely resonant with the atoms, the measured light can never reach zero intensity and a minimum intensity is always observed. This minimum intensity corresponds to a saturation optical density (OD_{sat}), which is observed when atoms have absorbed all of the resonant probe light. An OD larger than OD_{sat} should never be observed even if the optical density of the cloud is actually larger. A correction for this off-resonant background light $I_{\text{bkd}} = I_0 \exp(-OD_{\text{sat}})$ is modelled as a decrease in measured intensities, modifying the Beer-Lambert law to $\exp(-OD_{\text{mod}}) = \frac{I - I_{\text{bkd}}}{I_0 - I_{\text{bkd}}}$. The modified OD that corrects for saturation effects is

$$OD_{\text{mod}} = \ln \left(\frac{1 - e^{-OD_{\text{sat}}}}{e^{-OD_{\text{meas}}} - e^{-OD_{\text{sat}}}} \right). \quad (3.4)$$

The saturation OD is measured by imaging a dense cloud and observing a flat top distribution. Care should be taken to ensure there is enough probe light to reliably measure a large enough OD. A typical OD_{sat} during this work was 2.8.

Another imaging correction is the change in scattering rate caused by saturation of the atomic transition by the probe laser intensity. This correction to the Beer-Lambert law alters the scattering length $\sigma_{\text{scatt}} = \frac{\sigma_0}{1 + I/I_{\text{sat}}}$, where $\sigma_0 = \frac{\hbar\omega\Gamma}{2I_{\text{sat}}}$. The corrected Beer-Lambert law is

$$\frac{dI(z)}{dz} = -n_0\sigma_0 \frac{I(z)}{1 + I(z)/I_{\text{sat}}}, \quad (3.5)$$

where n_0 is the atomic density and the optical density is defined by $OD = \int dz n_0 \sigma_0$. Equation 3.5 can be integrated to obtain the saturation intensity correction to the Beer-Lambert law

$$OD_{\text{act}} = OD_{\text{mod}} + \left(1 - e^{-OD_{\text{mod}}}\right) \frac{I_0}{I_{\text{sat}}}. \quad (3.6)$$

The probe intensity in our experiments is set near $0.08I_{\text{sat}}$ to minimize the saturation correction factor, where $I_{\text{sat}} = 1.67 \text{ mW/cm}^2$ for ^{87}Rb .

The relative correction factors associated with OD_{sat} and I_{sat} are shown in Fig. 3.10. The combined relative correction to the measured OD takes into account both effects; the dominant effect at high ODs comes from the saturation OD correction. The measured OD correction is at least 15%, but for $OD < OD_{\text{sat}}/2$ the overall relative correction is less sensitive to fluctuations in OD. The peak OD of images in our experiments is set to occur where the correction factor is constant. That is at ODs of about 1.4 – 2.

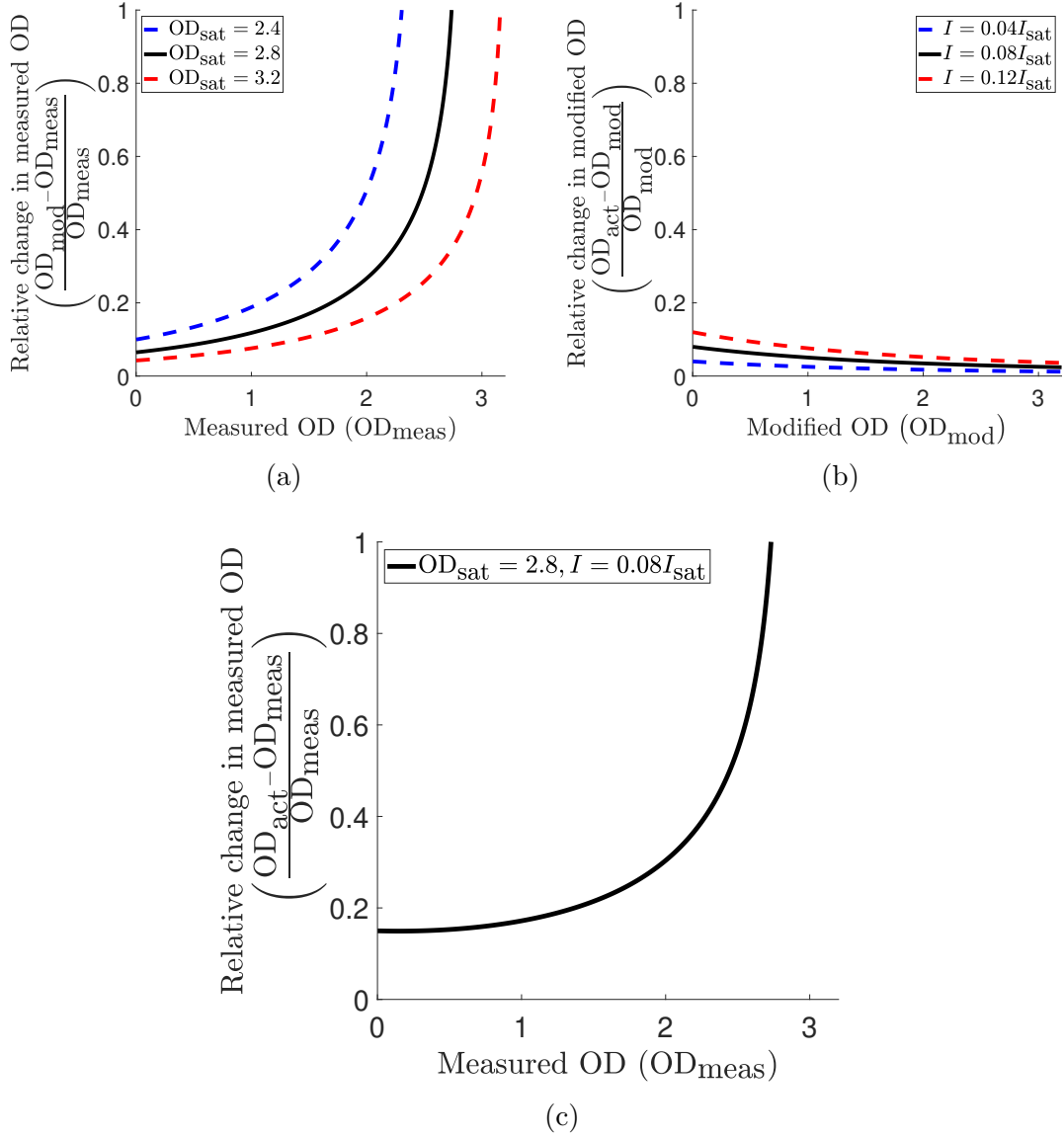


Figure 3.10: Correction factors for absorption imaging. (a) Correction due to saturation of resonant light (Eqn. 3.4), where the correction is significant near OD_{sat} . (b) Correction due to modified scattering rates (Eqn. 3.6). (c) Combined imaging correction factors show that the optimal OD to work at is anywhere less than $OD_{\text{sat}}/2$, where the correction factor is least affected by changes in the measured OD.

3.3.3 Fitting for cloud parameters

Figure 3.11 shows an example of a processed image of a nondegenerate cloud. The image shows the OD on a greyscale, where the darker color corresponds to a larger OD and more atoms per unit area. Each individual image is fitted for cloud parameters such as the temperature, density, and number of atoms. Thermal and nondegenerate clouds have a Gaussian shaped density profile so they are fitted with

$$f_{\text{Gaussian}} = OD_{\text{peak}} \exp\left(-0.5(z - z_c)^2/(z'_0)^2 - 0.5(y - y_c)^2/(y'_0)^2\right), \quad (3.7)$$

where z and y correspond to the axial and radial coordinates, z_c and y_c represent the center of the cloud, and z'_0 and y'_0 characterize the expanded widths of the cloud. The free parameters in the fit are OD_{peak} , z_c , y_c , z'_0 and y'_0 . Convergence of the fit can be a computationally slow process so the image is software binned to 4×4 pixels for speed. The true widths z_0 and y_0 of the cloud are calculated from the expansion time t via

$$z_0 = \frac{z'_0 \omega}{\sqrt{\omega^2 + (\omega^2 + \omega_0^2) \sinh^2(\omega t)}}, \quad (3.8)$$

where ω_0 is the trapping frequency before expansion and ω is the trapping frequency during expansion [84].

From the fitted parameters, we obtain the total number of atoms in the cloud

$$N = 2\pi z_0 y_0 \frac{OD_{\text{peak}}}{AC}, \quad (3.9)$$

where the specific absorption cross section for the rubidium-87 states we use is

$$AC = \frac{1}{2} \left(\frac{3\lambda^2}{2\pi} \right) \frac{1}{1 + 4\frac{\Delta^2}{\Gamma^2}}. \quad (3.10)$$

Here λ represents wavelength, Δ represents detuning, and Γ represents the natural linewidth. The cloud temperature

$$T = \frac{m\omega_z^2 z_0^2}{k_B} \quad (3.11)$$

is calculated from the axial width, because the axial expansion correction is smaller. Additionally, the axial trap frequency ω_z is less sensitive than the radial trap frequency

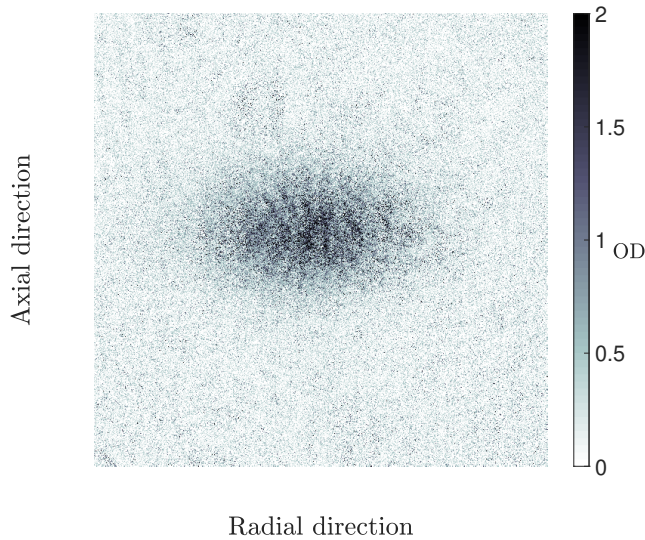


Figure 3.11: Example of an absorption image of an atomic cloud after processing for OD corrections. A larger OD corresponds to more atoms. The cloud has been expanded so that the camera does not saturate. This expansion is significantly faster in the radial direction, so the geometry of the imaged cloud is altered from the actual 37:1 trap ratio to approximately 2:1 here.

ω_ρ to changes in the bias magnetic field. The peak density of the cloud is given by

$$n_0 = \frac{1}{(2\pi)^{3/2}} \frac{N\lambda_{\text{trap}}^2}{z_0^3}, \quad (3.12)$$

where the trap ratio $\lambda_{\text{trap}} = \omega_\rho/\omega_z$ is given by the ratio of the measured trap frequencies in the radial and axial directions (See Sec. 4.1).

3.4 Accessible phase space

The apparatus described above can be used to study atomic clouds with a range of temperatures and densities. The accessible parameter space was roughly mapped out so that spin diffusion simulations could target experimentally attainable temperatures and densities. In some cases the accessible parameter space could be adjusted or extended by making physical modifications to the apparatus. As usual, there are trade-offs that lead to certain configurations being better for high or low density studies and other configurations that are better suited for high or low temperature clouds.

The first factor limiting the accessible phase space is the exclusion of degenerate gases, because the focus of this thesis is on spin diffusion in nondegenerate gases. The temperature at which Bose-Einstein condensation occurs is known as the critical temperature. It marks the boundary between the nondegenerate regime and the degenerate regime. The critical temperature for a harmonically trapped Bose gas is typically written with a dependence on cloud number. Obtaining a density dependence for the critical temperature of a harmonically trapped Bose gas would also provide a dependence on cloud temperature, because the number of atoms in the cloud depends on its temperature. To obtain only a density dependence, we use the critical temperature for a free-space Bose gas [96]

$$T_c = \frac{2\pi\hbar^2}{k_B m} \left(\frac{n_0}{\zeta(3)} \right)^{2/3}, \quad (3.13)$$

where n_0 is the peak density, and ζ is the Riemann-Zeta function. The critical temperature in Fig. 3.12 limits the accessible phase space to temperatures and densities that are outside of the degenerate regime. The degenerate regime is colored black and is excluded.

The imaging camera has a fixed field of view that is set by the imaging optics. For one optical configuration, the camera can only view a cloud up to a certain size before it ends up being larger than the field of view. For a hot cloud that is too large to image, the fits discussed in Section 3.3.3 would yield inaccurate results. One can limit the range of observable temperatures corresponding to cloud sizes around 2 to 2.5 σ , where $\sigma = \sqrt{k_B T / m \omega_z^2}$ is the Gaussian width. This range of widths corresponds to 95% to 99% of the atoms being visible within an image. The camera field of view limitation restricts the cloud temperature only and so this limitation is a horizontal line in Fig. 3.12. This view limitation could be adjusted with different optics that alter the field of view of the imaging camera, which would alter the image resolution.

Each camera pixel needs to collect enough photons to overcome electrical and photon shot noise to obtain a reasonable signal-to-noise ratio (SNR). For a low signal limit, and assuming zero expansion time, the minimal amount of photons required is empirically found to be around 10 photons per camera pixel. For a peak density of

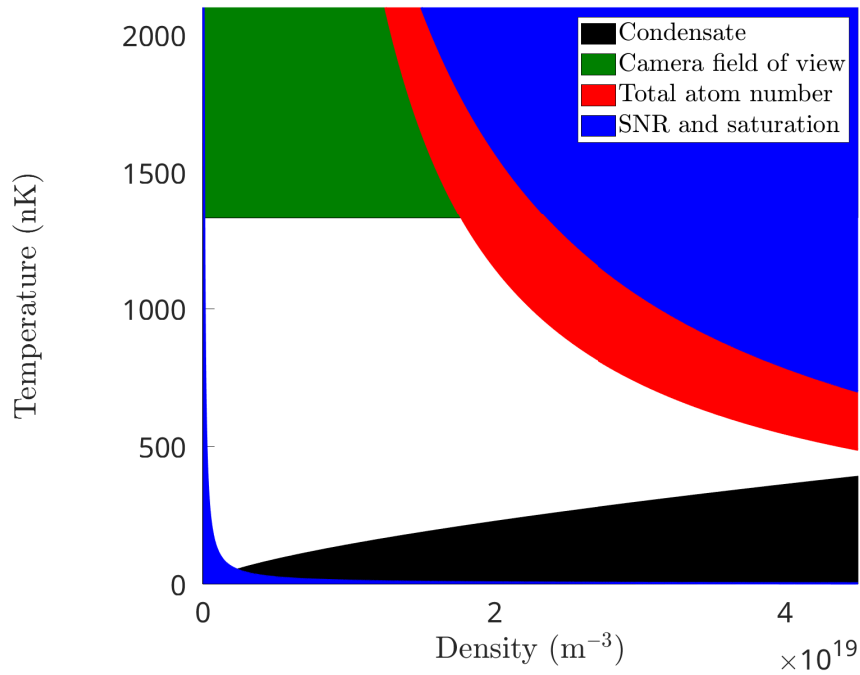


Figure 3.12: Temperature and density parameter space accessible by the apparatus (white). The exclusion zones are associated with Bose-Einstein condensation (black), low SNR and image saturation (blue), camera field of view (green), and total atom number (red). The condensation line is fixed for ⁸⁷Rb, but the rest of these limits could be adjusted to shift the accessible parameter space.

n_0 , the number of atoms within an imaging pixel N_{pixel} of size $p \sim 1.3 \mu\text{m}$ is given by

$$\begin{aligned} N_{\text{pixel}} &= \int_{-\infty}^{-\infty} dx \int_{B-p/2}^{B+p/2} dy \int_{A-p/2}^{A+p/2} dz n(x, y, z) \\ &= n_0 \sqrt{\frac{\pi^3}{2}} x_0 y_0 z_0 \left(\operatorname{erf} \frac{B+p/2}{\sqrt{2}y_0} - \operatorname{erf} \frac{B-p/2}{\sqrt{2}y_0} \right) \left(\operatorname{erf} \frac{A+p/2}{\sqrt{2}z_0} - \operatorname{erf} \frac{A-p/2}{\sqrt{2}z_0} \right), \end{aligned} \quad (3.14)$$

where erf is the error function, A and B are the axial and radial position of the center of the pixel within the cloud, the density is a Gaussian $n(x, y, z) = \exp(-x^2/2x_0^2 - y^2/2y_0^2 - z^2/2z_0^2)$, with Gaussian widths $\{x_0, y_0, z_0\} = \sqrt{\frac{k_B T}{m\omega_{\{x,y,z\}}^2}}$.

Equation 3.14 can be simplified by making three assumptions: only consider the center of the cloud ($A = B = 0$), assume the radial size of the cloud is small ($y_0 \ll p$), and assume the axial size is large ($z_0 \gg p$). With these assumptions the number of atoms per pixel is

$$N_{\text{pixel}} = n_0 2\pi x_0 y_0 p, \quad (3.15)$$

where the limit $\operatorname{erf}(\pm\infty) = \pm 1$ and approximation $\operatorname{erf}(x) \approx \frac{2}{\sqrt{\pi}}x$ for $x \ll 1$ have been used. Using the fact that the radial widths of the cloud are symmetric ($x_0 = y_0$), a lower bound on the temperature for which adequate image quality is obtained is

$$T_{\text{lower}} = \frac{m\omega_{\rho}^2 N_{\text{pixel}}^{\text{lower}}}{2\pi k_B p n_0}. \quad (3.16)$$

For a fixed peak density, images acquired at temperatures below T_{lower} do not have enough atoms per camera pixel to obtain a reasonable SNR at the center of the cloud.

Similarly, an upper bound on the temperature can be estimated. For a fixed atom number per pixel, temperatures above this bound temperature would yield saturated images. The only change here is that the cloud is allowed to expand to prevent saturation, so Eqn. 3.8 is used to modify the Gaussian widths to $x_0 \rightarrow x_0(t)$, $y_0 \rightarrow y_0(t)$, $z_0 \rightarrow z_0(t)$. The upper bound on the temperature is then

$$T_{\text{upper}} = \frac{m\omega_{\rho}^2 N_{\text{pixel}}^{\text{upper}}}{2\pi k_B p n_0} \left(\frac{\sqrt{\omega^2 + (\omega^2 + \omega_0^2) \sinh^2(\omega t)}}{\omega} \right)^2, \quad (3.17)$$

where the maximum expansion time t is about 5 ms when the edge of the cloud expands past the field of view, and $N_{\text{pixel}}^{\text{upper}}$ is the upper limit to the number of atoms imaged by one camera pixel. The upper and lower bounds on the range of accessible

temperatures are shown in Fig. 3.12. The primary constraint they impose is a limit for the lowest accessible densities.

Lastly, the apparatus is limited at high densities by the maximum number of atoms the MOT can load and transfer into the science cell. Evaporation also affects the peak obtainable density. The cloud temperature as a function of peak density is

$$T(n_0) = \frac{m\omega_z^2}{2\pi k_B \lambda^{4/3}} \left(\frac{N(T)}{n_0} \right)^{2/3}. \quad (3.18)$$

At 650 nK and near the maximum MOT load, it was empirically found that the number of atoms in the science cell varied as 2×10^3 atoms/nK. This means the number of atoms in the science cell can be approximated with

$$N(T) = N_0 + 2 \times 10^3 \text{ atoms/nK} \times (T(\text{nK}) - 6.5 \times 10^2 \text{ nK}), \quad (3.19)$$

where $N_0 = 2 \times 10^6$ represents the number of atoms in the cloud at 650 nK. For the same MOT load, there are fewer atoms at colder temperatures since those atoms were evaporated. This empirical result is extrapolated to the rest of the parameter space, where Eqn. 3.19 is unlikely to be accurate across the entire range but is a reasonable first guess. The exclusion zone imposed by the total atom number is shown in Fig. 3.12. This limit could be pushed to higher temperatures and densities by increasing the MOT load, improving transfer efficiency from the MOT to the science cell, or by improving evaporation efficiency.

Putting all of these limiting cases together, the parameter space that can be accessed by the apparatus currently allows for temperatures from 100 – 1,300 nK and peak densities of $0.2 - 4 \times 10^{19} \text{ m}^{-3}$. At high densities the system is limited by either total atom number or Bose condensation. At low densities, the range of accessible temperatures opens up, but is limited by low SNR or the expansion of the cloud.

3.5 Spin detection

3.5.1 Longitudinal spin detection

Longitudinal spin is measured by acquiring absorption images over two separate experimental cycles. The first cycle characterizes state $|1\rangle$ by the usual imaging procedure in Section 3.3.1. On the second experimental cycle a π -pulse is applied to

swap the $|1\rangle$ and $|2\rangle$ state populations, and then the same imaging procedure is repeated. An example of a combined false color image from images acquired during the two cycles is shown in Fig. 3.13(a). The radial direction is averaged to obtain the longitudinal spin density across the axial direction of the quasi-1D cloud. An example of the 1D spin profile is shown in Fig. 3.13(b), where the separate spin profiles are labelled as N_1 and N_2 for states $|1\rangle$ and $|2\rangle$, respectively. Each longitudinal spin profile represents a projection of the spin states into the respective basis states, $|1\rangle$ and $|2\rangle$. Adding these two spin profiles together gives the total spin in our system, if the spins were fully coherent. This maximum total spin profile corresponds to the atomic density distribution. Temperature and peak density can be fitted using this 1D atomic density profile and used to monitor the temperature and density of the cloud throughout data collection. The difference between the $|1\rangle$ and $|2\rangle$ spin profiles is the longitudinal spin profile across the cloud, where positive spin corresponds to $|2\rangle$ (up in Bloch sphere) and negative spin corresponds to $|1\rangle$ (down in Bloch sphere). The spin preparation technique described in Sec. 3.2 creates a dipolar spin profile with two axially separated domains within the cloud as shown in Fig. 3.13. These dipolar spin domains are the typical initial spin profile used in this work, but arbitrary initial spin profiles are discussed in Section 3.8.

The longitudinal spin profile is measured at various times after preparation to explore longitudinal spin diffusion. One of these longitudinal spin diffusion plots is shown in Fig. 3.14(a), where each horizontal slice is one spin density profile. Ideally, the longitudinal spin density is always calculated with $M_z = N_2 - N_1$ for these spin diffusion plots. Unfortunately, spin diffusion homogenizes the spin, leading to smaller longitudinal spin amplitudes. Additionally, dipolar relaxation collisions lead to loss of the $|2\rangle$ state and removal of spin from the cloud. These reductions in the peak M_{tot} can make the spin diffusion plot challenging to read over long timescales. A normalized longitudinal spin $M_z^* = \frac{N_2}{N_{2\text{tot}}} - \frac{N_1}{N_{1\text{tot}}}$ is sometimes shown to highlight the long-term spin behaviour, by normalizing away the spin decay at each sample in time. Here $N_{1\text{tot}} = \sum_i N_1(z_i)$ and $N_{2\text{tot}} = \sum_i N_2(z_i)$ are the total spin of each state, where i denotes each axial bin along the cloud. A comparison between non-normalized and normalized spin diffusion plots is shown in Fig. 3.14, where the difference between them mainly shows up at long diffusion times. The normalized spin diffusion is used when presenting the spin dynamics in a spatio-temporal plot like Fig. 3.14, because it amplifies the long-time behaviour. However, for computing cloud density and temperature from the longitudinal spin components (see Section 3.6), the unnormalized spin diffusion should be used since the normalized spin diffusion will alter these quantities. The spin

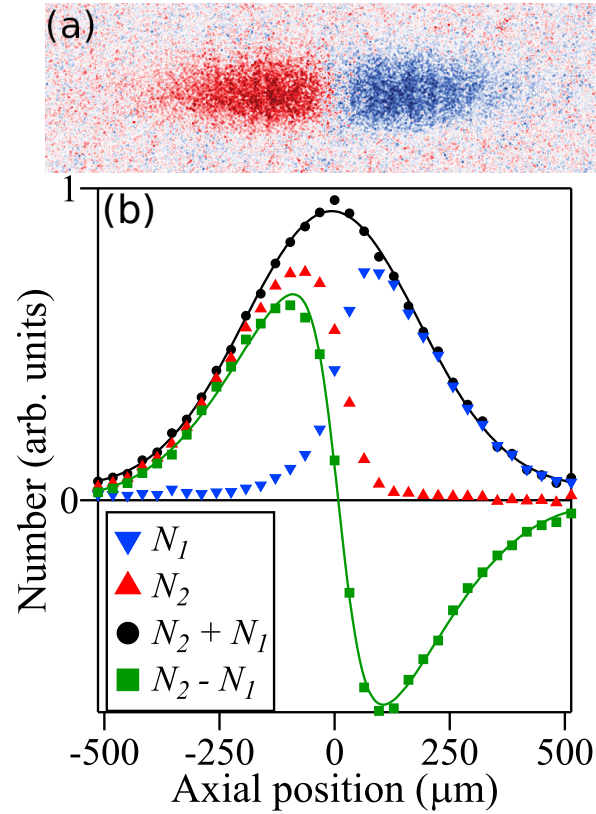


Figure 3.13: Detection of longitudinal spin using two absorption images and radial averaging. (a) A false-color image of the combined $|1\rangle$ (blue) and $|2\rangle$ (red) images. (b) Radially averaged spin density profiles for $|1\rangle$ (blue) and $|2\rangle$ (red), where N_1 and N_2 correspond to the number of atoms in states $|1\rangle$ and $|2\rangle$, respectively. The sum of the two profiles is the atomic density profile $n(z)$ and the difference represents the longitudinal spin density profile $M_z(z, t)$, where $t = 0$ in this example.

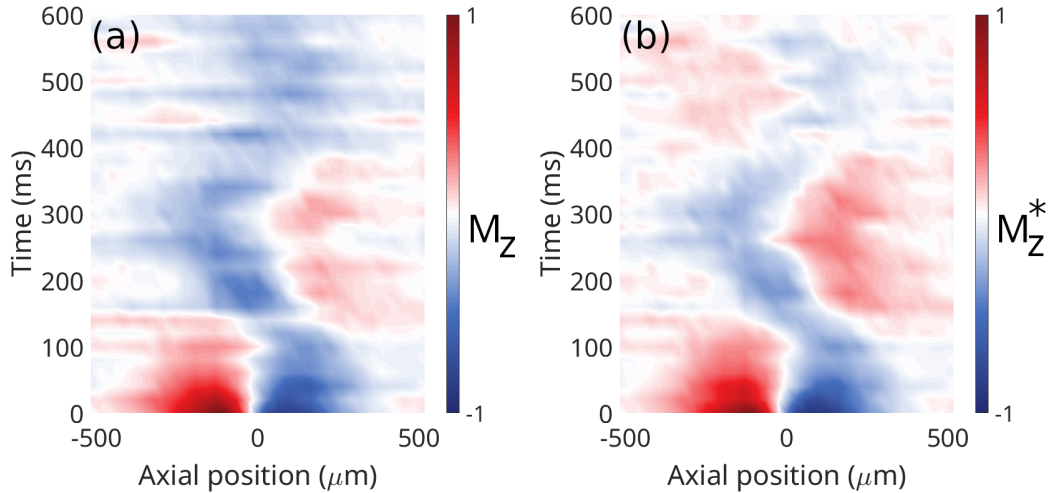


Figure 3.14: Spin diffusion in a flat differential potential ($U_{\text{diff}} \approx 0$) showing (a) the unmodified longitudinal spin profile and (b) the normalized spin profile. The difference between the two is minimal up to about 200 ms. At long times, the normalization process inflates the population of state $|2\rangle$ because atoms are lost from that state via dipolar relaxation.

quantities, such as dipole moment and spin domain width (see Section 5.2 and 6.2), also see a small shift in absolute value between the normalized and unnormalized spin diffusion. However, the dynamics of these spin quantities are nearly identical for the normalized and unnormalized spin diffusion, so it does not matter which method is used for processing these spin quantities. The amplitude of the spin domain would see a significant shift between the normalized and unnormalized cases, so care should be taken if the domain amplitude becomes an important quantity to track.

3.5.2 Transverse spin detection

Transverse spin is not as easy to characterize as longitudinal spin, where the spin state is projected onto the longitudinal states ($|1\rangle$ or $|2\rangle$). Instead, measuring transverse spin requires the use of Ramsey interferometry (see Section 2.1.2) to generate fringes corresponding to the transverse phase precessing relative to a phase reference. In the work described in this thesis, the RF and microwave oscillators are used as phase references since they are coherent over the course of the experiment, and the transverse spins precess relative to the phase of these oscillators. The first $\pi/2$ -pulse in a Ramsey interferometry sequence sets the atom-oscillator phase reference, and the relative phase of the second $\pi/2$ -pulse specifies how the spins rotate in the Bloch sphere (see Eqn. 2.7). For the initial spin state discussed in Section 3.2, the initial

cloud-wide pulse sets the phase reference when the center of the cloud undergoes a $\pi/2$ -pulse. Oscillator and atom phase noise must be small during the time between the two Ramsey pulses to generate high-quality Ramsey fringes.

A single Ramsey fringe is the minimum requirement to measure transverse spin since an amplitude and phase can be extracted by fitting with a sine wave. This Ramsey fringe is obtained by performing Ramsey spectroscopy for various relative phases on the second Ramsey pulse and projecting the rotated spin onto the $|1\rangle$ state. The phase can be varied in a few different ways, depending on the capabilities of the oscillators used. For an oscillator with a frequency detuned from the atomic resonance, the measured transverse phase evolves linearly in time t as

$$\phi = 2\pi ft, \tag{3.20}$$

where f is the detuning or Ramsey frequency. Experimental techniques that measure transverse spin must precisely control this relative phase and the most straightforward approach is to control the detuning frequency using a frequency-shift key (FSK) modulation. Two of the transverse spin detection techniques in this section use the RF oscillator's FSK feature to control the relative transverse phase, while the third technique shifts the phase directly using a phase-shift key (PSK) modulation. Both the FSK and PSK functions maintain phase coherence during the shifted frequency or phase so that the net effect is a shift in the phase reference.

In this thesis, the transverse spin magnitude M_{\perp} and phase M_{ϕ} are measured by using the FSK and PSK oscillator features to measure at least one Ramsey fringe. The three transverse spin measurement techniques are called: moving window FSK, pseudo-PSK, and PSK. A summary of how the relative oscillator phase evolves during each of these measurement techniques is shown in Fig. 3.15. The moving window FSK technique constantly shifts the oscillator phase, while the pseudo-PSK method applies a brief FSK to rapidly change the relative phase. Lastly, the PSK method applies a tunable phase shift only during the second $\pi/2$ -pulse.

Moving window FSK

Just before starting the imaging procedure (Sec. 3.3.1), a $\pi/2$ -pulse is applied to rotate the spin states about a specific oscillator phase in the Bloch sphere. This rotation effectively transfers a particular transverse spin into the $|1\rangle$ state, which is then imaged using the same ARP and cycling transition as previously described in Sec. 3.3.1. A single image is not enough to measure transverse spin, because the full

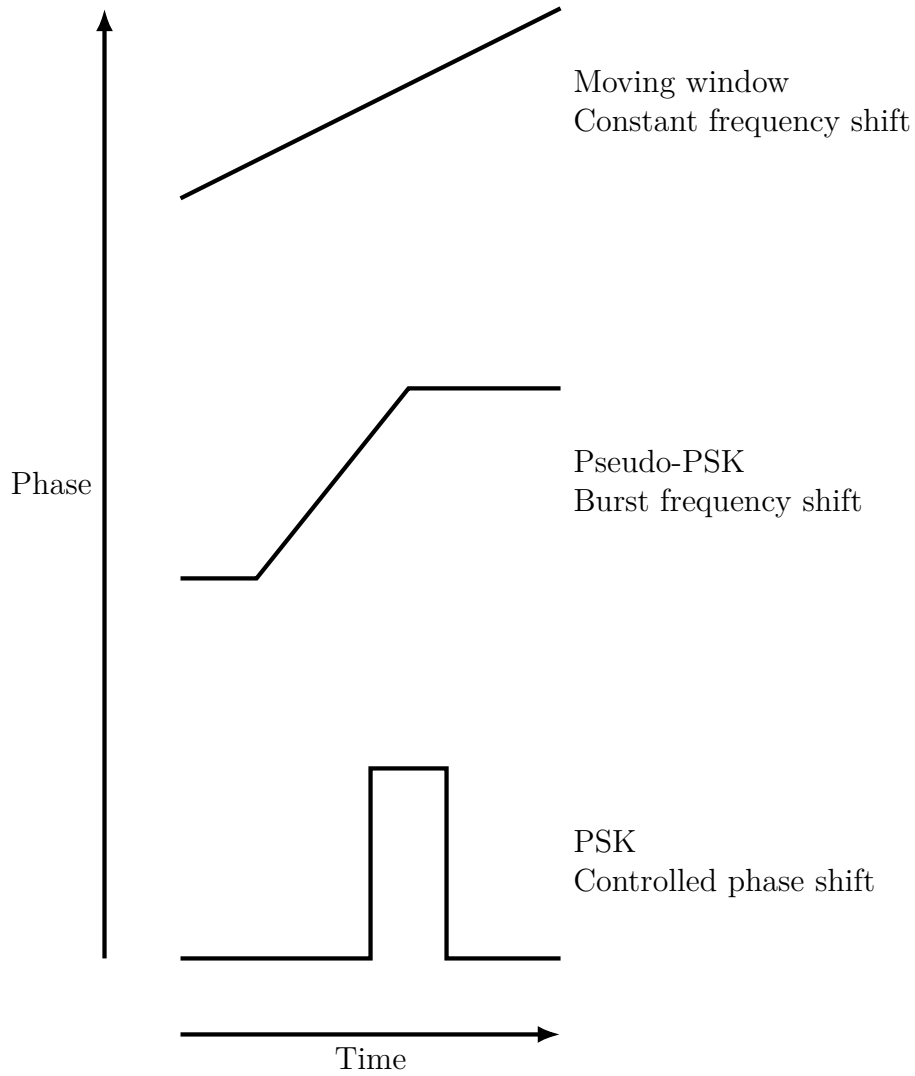


Figure 3.15: Comparison of the relative oscillator phase shift for the three transverse spin measurement techniques. In the moving window technique, the oscillator acquires phase at a constant rate, while in the pseudo-PSK method the oscillator rapidly accrues a controllable phase over a short period of time. The PSK technique arbitrarily shifts the phase of the oscillator as desired, making it the most flexible technique for shifting the phase of an oscillator used for measuring transverse spin.

range of transverse phases must be sampled to accurately measure M_{\perp} and M_{ϕ} with a Ramsey oscillation. The transverse phase that is transferred to $|1\rangle$ can be controlled by applying a fixed FSK to the RF synthesizer and waiting various amounts of time for different phases to accumulate. This phase difference between the RF synthesizer and atomic precession alters the relative phase of the Rabi vector ($\underline{\Omega}'_{\mathbf{R}}$ in Eqn. 2.7) on the Bloch sphere, altering the $\pi/2$ -pulse rotation axis. Multiple images are collected for different $\pi/2$ -pulse phases to measure an oscillation at the FSK frequency.

To measure the temporal evolution of transverse spin, a moving window is used to fit the data within a small time window. An example of the moving window process is shown in Fig. 3.16, where the data is fitted with a fixed frequency as the window moves from left to right. Each axial bin is individually processed with these moving time windows. Each moving window is fitted with a sine function for the transverse amplitude M_{\perp} , transverse phase M_{ϕ} , and an offset. The offset is important to obtain a good fit and is a measure of the incoherent transverse spin and longitudinal spin imbalance. Here incoherent transverse spin is present when averaging over multiple transverse spins that have varying phases, and an ensemble of transverse spins that have random phases is fully incoherent. Maximally coherent transverse spin occurs when the transverse phases are all equal, and there is a continuum between maximally coherent and incoherent.

The moving window method is the fastest to collect data because it usually requires fewer experimental cycles to complete. However, this method averages the transverse spin over the moving window width of about 30 – 50 ms. Another downside is that multiple sampling frequencies are required both to obtain high resolution at short time and to keep data collection time low for long times. Additionally, comparisons with longitudinal spin are difficult with this method since the averaging alters the transverse spin data. Because of this averaging, the short time spin behaviour is typically lost with the moving window method. Even with these negatives, the moving window FSK method was used to measure transverse spin in this thesis because of the faster collection speed and because the other techniques had not been developed.

Pseudo-PSK and PSK

The FSK or PSK features of an RF synthesizer can be leveraged for higher quality transverse spin detection. The pseudo-PSK and PSK methods use these synthesizer features to allow measurements at a single time, eliminating any averaging of

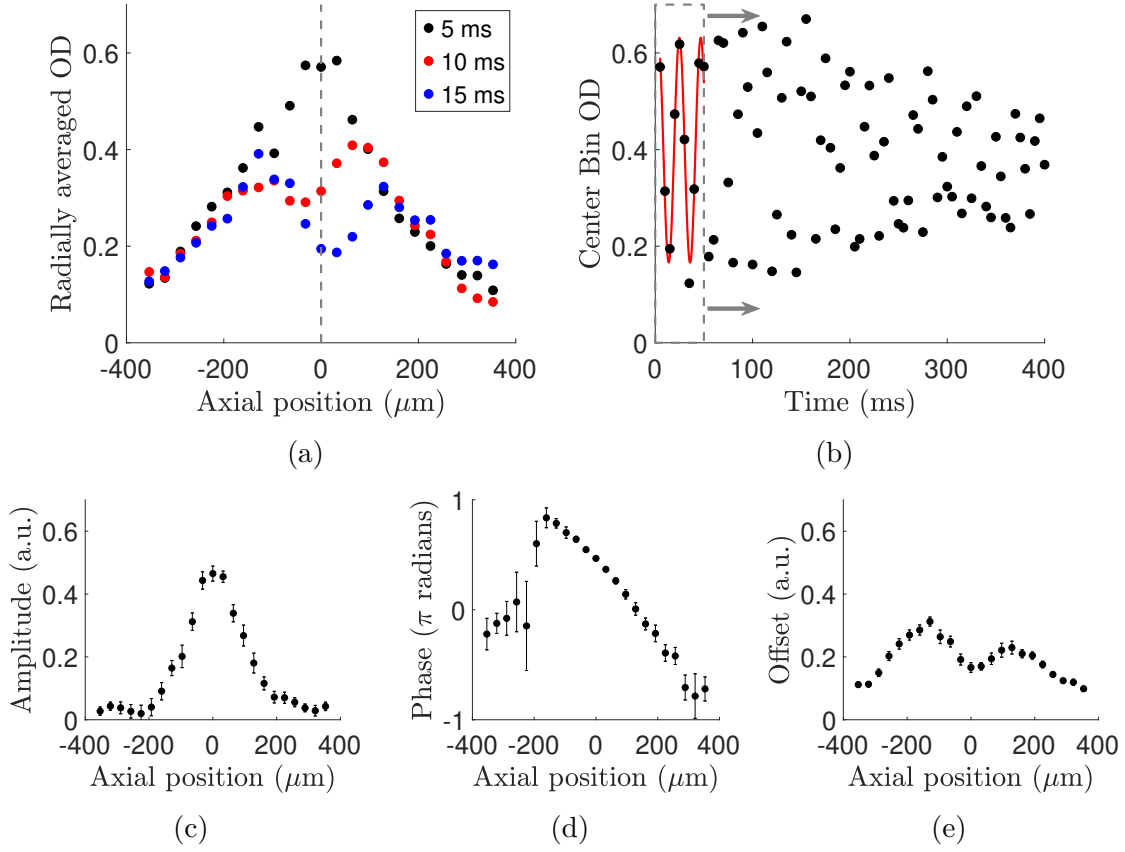


Figure 3.16: The sequence of steps involved in extracting information about transverse spin from the raw binned data with a moving window at a known Ramsey frequency. (a) The raw binned 1D atomic profiles at the first three delay times in the Ramsey fringes, with the center bin (dotted line) being used as an example for the moving window. (b) Center bin OD is measured as a function of time and a moving window fit of a sine function is performed on the data within the window. The fit extracts the transverse (c) amplitude, (d) phase, and (e) offset, which are shown for the first moving window from 0 – 50 ms. Error bars represent fit uncertainties.

the transverse spin. Additionally, these improved short-time transverse spin measurements can be easily compared with longitudinal spin. Unfortunately, these two methods require more experimental cycles to complete, but the ease of experimental use and the improved detection quality makes these two methods enticing choices. Just as in the moving window technique, both of these methods transfer a tunable transverse phase to the $|1\rangle$ state, which is then imaged. The detected transverse phase is then controlled so each time has measurements of at least five transverse phases for fitting.

Pseudo-PSK is an extension of the moving window method, except with higher FSK frequencies and smaller moving windows that do not share any points with adjacent windows. The phase of the RF photon is manipulated with an FSK of 2000 Hz applied for up to 1 ms, which corresponds to a rotation of 4π (two oscillations). The experimental timings are adjusted so that transverse phases are measured at the same evolution time (to within the resolution of electronics of ~ 50 ns) so that there is no averaging of spin diffusion. The relative oscillator phase of the $\pi/2$ -pulse is $\phi = 2\pi f_{\text{FSK}} t_{\text{FSK}}$, where f_{FSK} and t_{FSK} are the FSK frequency and time of the FSK. An example of pseudo-PSK transverse spin data is shown in Fig. 3.17, where each time stamp is fitted at a fixed FSK frequency for an amplitude, phase, and offset. This pseudo-PSK method requires the two-photon detuning to be well known across the cloud so that the fitted frequency can be fixed across the cloud. For large FSKs of about 2 kHz, the spatial variations of the two-photon detuning due to the mean-field (Eqn. 3.23) and Zeeman shift (Eqn. 3.22) are negligible since they only vary by about 5 Hz across the cloud. By ignoring these small spatially varying shifts, the measured Ramsey fringes can be fitted with a singular FSK frequency for all axial positions along the cloud.

Some RF synthesizers now come with an arbitrary PSK option that allows arbitrary phase shifts to be applied to the RF signal. A PulseBlasterDDS-I-300 RF synthesizer was added to the apparatus so that arbitrary PSK could be used to alter the relative oscillator phase, instead of the time-varying FSK used in the pseudo-PSK method. In the PSK method of transverse spin detection, a controlled phase of ϕ is applied to the RF portion of the $\pi/2$ -pulse before imaging. Multiple images collected for varying PSK phases are used to measure a single Ramsey fringe, with the PSK phases corresponding to a phase difference of 2π between the first and last point. The PSK procedure then follows the same as pseudo-PSK, where multiple images are collected at specific phases between 0 and 2π . The difference here is that the phases are easily controlled, since the RF synthesizer can jump to specific phases and map

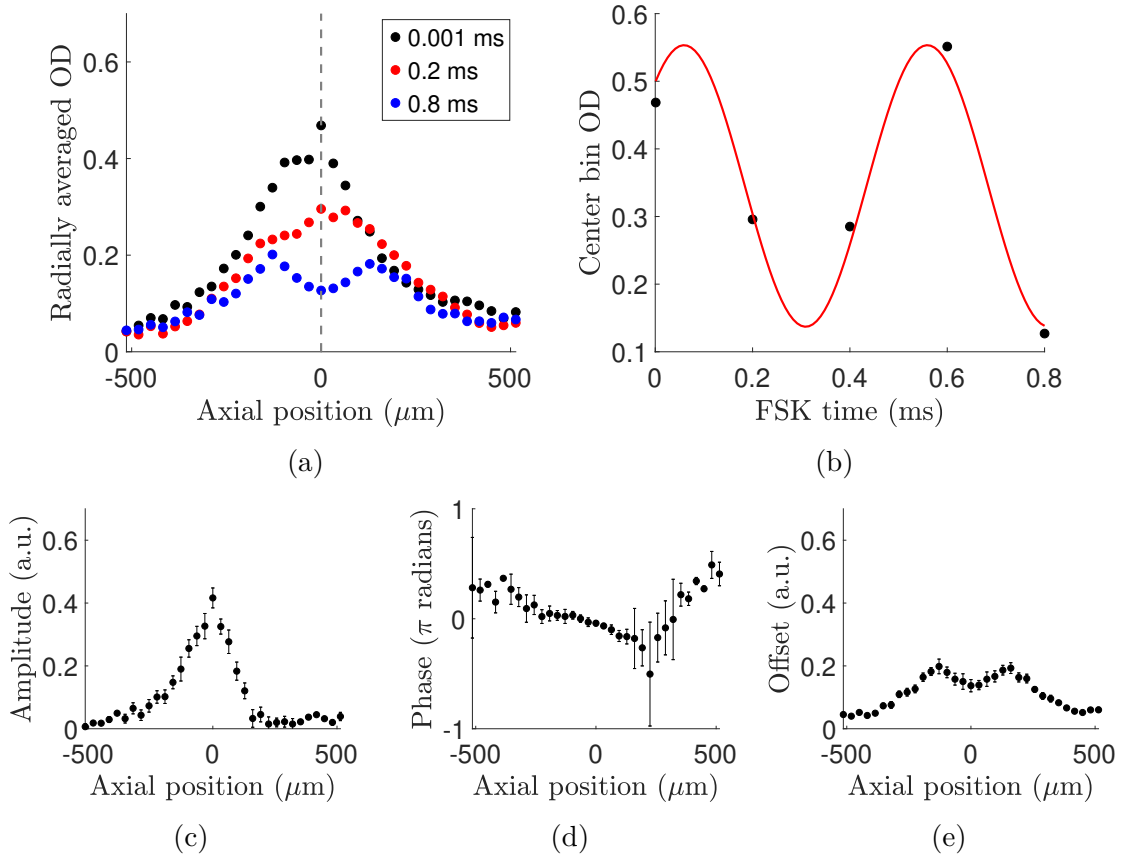


Figure 3.17: The sequence of steps involved in extracting information about the transverse spin by using the pseudo-PSK method. This method samples the transverse spin for five or more different transverse phases using an FSK frequency of 2 kHz. (a) The raw binned 1D density profiles for three of these two-photon phases (FSK times) are shown, where the center axial bin (grey dashed line) being used as an example for fitting. (b) The transverse spin in the center bin, and at different phases, is fitted to a sine at the FSK frequency (red). The fitted transverse spin parameters across the cloud are: (c) amplitude, (d) phase, (e) offset. Error bars represent fit uncertainties.

out an interference fringe. Five images are collected to obtain one oscillation, where the total time since domain preparation is fixed for each PSK phase in the oscillation. Once again, the data is fitted with a sine for the transverse amplitude, phase, and offset. An example of the processing of the raw data and the fitted results from the PSK method is shown in Fig. 3.18. The quality of the data is comparable to pseudo-PSK data, except that a finer axial bin resolution was used for the PSK data.

Because the pseudo-PSK and PSK methods use five images for each specific measurement time, transverse spin can be measured at arbitrary time steps with no smoothing of spin diffusion. This makes these two methods suitable for combining with the measured longitudinal spin. If time permits, pseudo-PSK or PSK should be the preferred spin detection methods. The pseudo-PSK method can be sensitive to large detunings where the effective FSK frequency will shift. However, since the data acquired with the PSK method is always fitted for the same frequency regardless of detuning, the PSK method is preferred if either the RF synthesizer or microwave synthesizer have a PSK feature.

3.6 Total spin by combining spin components

In the previous section, the techniques used to measure the spatial distribution of the longitudinal and transverse spin components were presented. The data from these measurements can be combined to obtain the total spin as a function of position in the cloud. The total spin is useful for checking the consistency of spin preparation, obtaining estimates of the efficiency of transfer pulses, and for monitoring the decay of total spin as diffusion occurs. Combining spin components works best when the transverse spin and longitudinal spin components are measured with the same time delays, however interpolation can be used if the temporal match is imperfect.

Three data sets are collected to compute the total spin: the density profile, the transverse spin profile, and the longitudinal spin profile. Examples of these three spin profiles are shown in Fig. 3.19(a) for spin preparation using the aluminum mask as described in Section 3.2. Three more examples are shown in Fig. 3.19(b) for the case where a near optimal initial state preparation is used. See Section 4.10 for a definition of what an optimal preparation entails and how to optimize spin preparation. Even in the optimal case, the initial total spin amplitude is a bit lower than the density profile amplitude. This difference can be attributed to the efficiencies of the spin preparation procedures and transfer pulses.

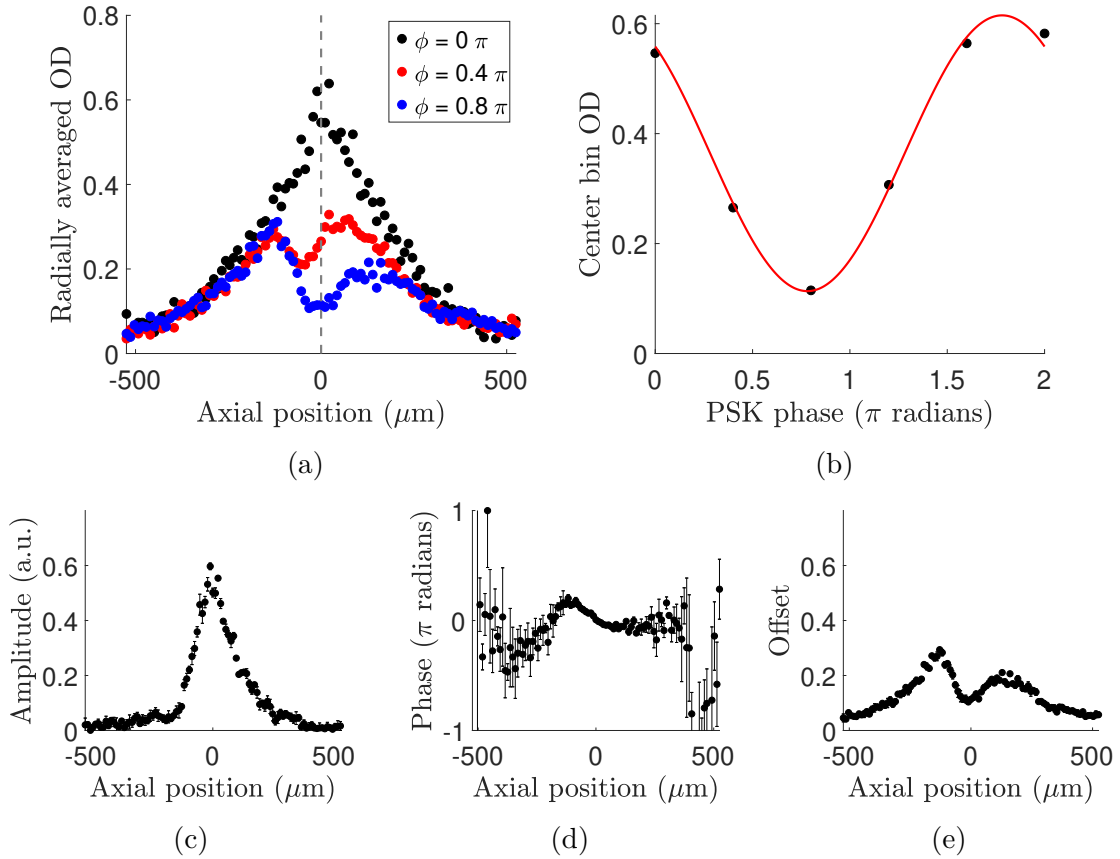


Figure 3.18: The sequence of steps involved in extracting information about the transverse spin by using the PSK method. This method samples the transverse spin for six different transverse phases by using a PSK during the second $\pi/2$ -pulse. (a) The raw binned 1D density profiles for three axial profiles show the transverse spin profile at the three labelled PSK phases. The center bin is the dashed grey line. (b) The oscillation of the projected transverse spin at the center bin is an example of fitting with a sine wave at a frequency of 1 Hz (red). The extracted fit parameters that spatially vary across the cloud are: (c) amplitude, (d) phase, and (e) offset. Error bars represent fit uncertainties.

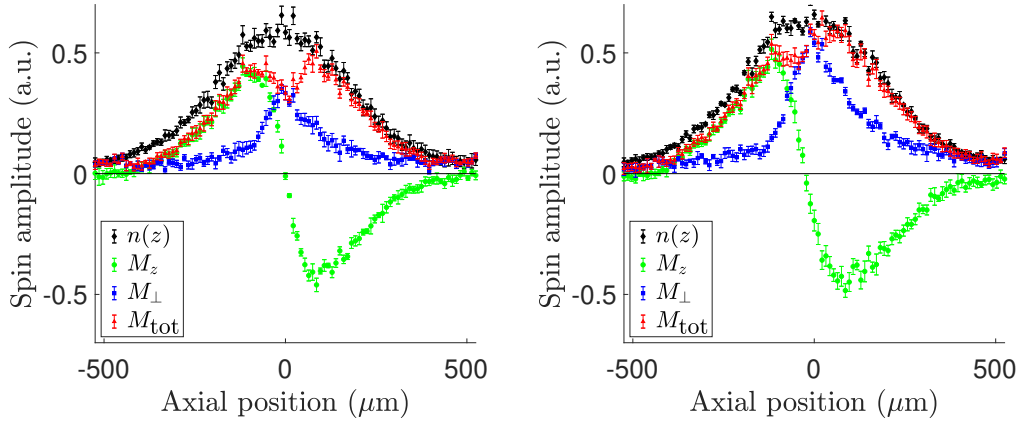


Figure 3.19: Combining the measured longitudinal (green) and transverse (blue) spin components gives the total spin density (red). The total spin should agree with the density profile (black). (a) The total spin after preparation with the aluminum mask. (b) The total spin after an optimized initial spin preparation, where the transverse spin in the center is increased (see Sec. 4.10). The $|2\rangle$ (positive) longitudinal spin domain is measured lower than the $|1\rangle$ domain because of the imperfect pulse efficiency of the two cloud-wide π -pulses needed to prepare and measure that spin state.

3.7 Effective magnetic field control

The evolution of transverse spin depends on the potential energy difference between the two spin states, called the differential potential U_{diff} (see Eqn. 2.46). The differential potential describes the relative precession rate of transverse spin around the z -axis of the Bloch sphere. This precession rate is a spatially varying Larmor precession frequency generated by a differential Zeeman shift, a differential scattering length between the pseudo-spin states, and an applied spin-dependent potential.

At low fields, where the magnetic field interaction $-\underline{\mu} \cdot \underline{\mathbf{B}}$ is much smaller than the correction to the hyperfine splitting, the differential Zeeman shift is $\Delta E = \mu_B(g_F m_F - g'_F m'_F)B$ between the two spin states, where the primed variables correspond to $|1\rangle$ and unprimed for $|2\rangle$. Since the product $g_F m_F$ is the same for both spin states, the differential Zeeman shift is zero in the low field limit. At fields of order ~ 3 G, there is a small difference between the spin states arises because of coupling between the hyperfine and Zeeman interactions. For intermediate magnetic fields, where the correction to the hyperfine splitting and the Zeeman interaction are comparable, this energy shift can be found by diagonalizing the Hamiltonian

$$H = \frac{\Delta E_{hf}}{I + \frac{1}{2}} \underline{\mathbf{I}} \cdot \underline{\mathbf{J}} - \underline{\mu} \cdot \underline{\mathbf{B}} \quad (3.21)$$

for the case $J = 1/2$ to obtain the Breit-Rabi formula [97, 98]

$$\Delta E(z) = \frac{-\Delta E_{hf}}{2(2I+1)} - \mu_B g'_I m_F B(z) \pm \frac{\Delta E_{hf}}{2} \sqrt{1 + \frac{4m_F x}{2I+1} + x^2}. \quad (3.22)$$

Here $x = (g_J + g'_I) \frac{\mu_B B(z)}{\Delta E_{hf}}$, ΔE_{hf} is the hyperfine splitting energy at zero field, I is the nuclear angular momentum, B is the magnetic field magnitude, m_F is the Zeeman sublevel, and g'_I and g_J are the nuclear and Landé g-factors. The spatial dependence of ΔE comes from the magnetic field, which is parabolic in the axial z direction. The Breit-Rabi formula is used to model the contribution of the differential magnetic-field shift to the differential potential. Typical differential energy shifts caused by the magnetic field amount to variations of about 10 Hz across the cloud.

The mean-field shift caused by the different scattering lengths of ^{87}Rb is given by the cold-collisional shift for noncondensed indistinguishable bosons [99, 84]

$$\Delta_{\text{MF}}(z) = \frac{4\pi\hbar^2}{m_{\text{atomic}}} [2a_{22}n_2(z) - 2a_{11}n_1(z) + 2a_{12}(n_1(z) - n_2(z))], \quad (3.23)$$

where m_{atomic} is the ^{87}Rb mass, a_{ij} are the scattering lengths between two atoms in states i and j , and $n_i(z)$ is the density profile of atoms each spin state. The atomic density profile is Gaussian distributed along the axial direction because of the trap geometry. Typical differential mean-field shifts are about 5 Hz at the center of the cloud in our experiments.

A constant shift of the differential potential alters the common Larmor precession frequency, which can always be eliminated by an appropriate choice of rotating reference frame. However, spatial variations of the differential potential exist in all rotating frames, and must be minimized by controlling the differential magnetic-field shift and the mean-field shift (Eqn. 3.22 and Eqn. 3.23). The magnetic field that minimizes the spatial variations of the differential potential is called the cancellation spot. For the small mean-field shifts used in the work described in this thesis, the magnetic field of the cancellation spot is within 0.1 – 0.3 G of the magic spot. The magic spot is where the energy difference between the spin states is insensitive to magnetic field fluctuations. The shift in the magnetic field from the magic spot is small because of the small mean-field shift that is cancelled by a small differential magnetic-field shift. The cancellation of these two differential effects is shown in Fig. 3.20. The spatial profiles of these two shifts do not exactly cancel because the mean-field shift is a Gaussian

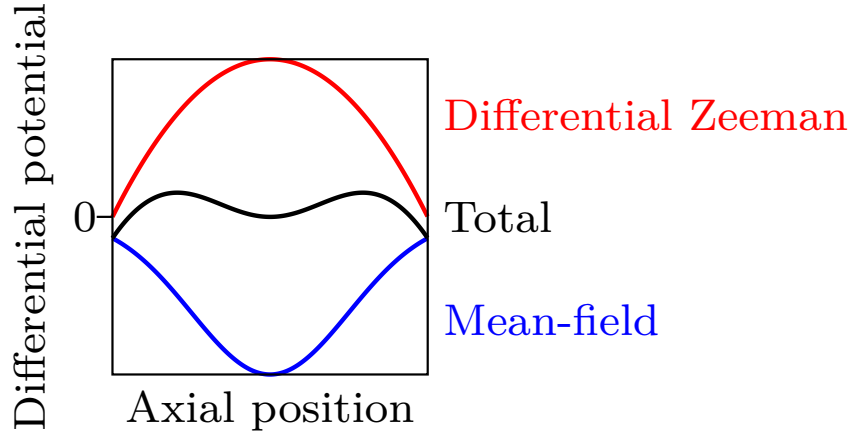


Figure 3.20: Cancellation of the differential potential across the cloud. The Gaussian mean-field shift (blue) is partially cancelled with a quadratic magnetic field shift (red). The spatial variation of the sum (black) of these contributions is minimized by altering the magnetic field to operate at the cancellation spot.

while the magnetic-field shift is parabolic. The cancellation spot is the magnetic field that flattens the differential potential at the center of the cloud.

In Fig. 3.21, the differential potential of the two spin states is shown as a function of magnetic field. The minimum energy difference defines the magic spot, where the energy difference between the spin states is insensitive to changes in the magnetic field and the differential magnetic-field is spatially flat. The cancellation spot is found by shifting the magnetic field from the magic spot until the differential potential is largely cancelled when measured with Ramsey spectroscopy. Care must be taken to ensure the magnetic field is shifted in the correct direction to cancel out the mean-field shift and not add to it. While the spatial variation of these shifts are small at only a few Hz across the cloud, any spatial variation of the differential potential can lead to a lower coherence time, since spins will precess at different rates and spread out in the transverse plane.

The cancellation spot changes every time the temperature or density of the cloud changes. This is because a change in the density will shift the magnitude of the mean-field shift, or a change in the temperature alters the spatial profile of the mean-field shift. An example of the differential potential across a cloud with $T = 650$ nK and $n_0 = 2.8 \times 10^{13}$ cm⁻³ is shown in Fig. 3.22. Ramsey spectroscopy is used to measure the spatial variation of the differential potential. At the cancellation spot, the differential potential should be flat at the center of the cloud. Each time the cloud parameters are changed, the magnetic field corresponding to the now shifted cancellation spot can be

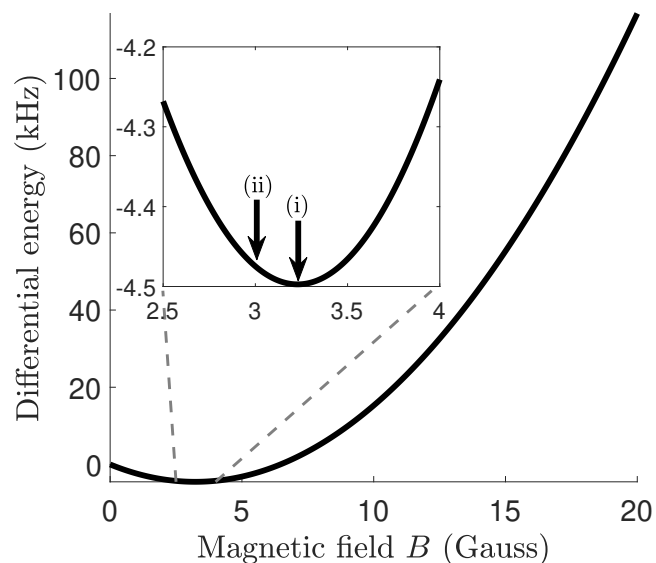


Figure 3.21: The energy difference of the two spin states ($|1\rangle$ and $|2\rangle$) in a magnetic field in frequency units. The inset shows the minimum in differential energy that defines the magic spot (i), where the energy difference is insensitive to magnetic field fluctuations. The cancellation spot (ii) corresponds to the magnetic field that flattens spatial variations of the mean-field differential potential. Since the cancellation spot at $B \sim 3$ G is close to the magic spot $B = 3.23$ G, it also benefits from low sensitivity to magnetic field fluctuations.

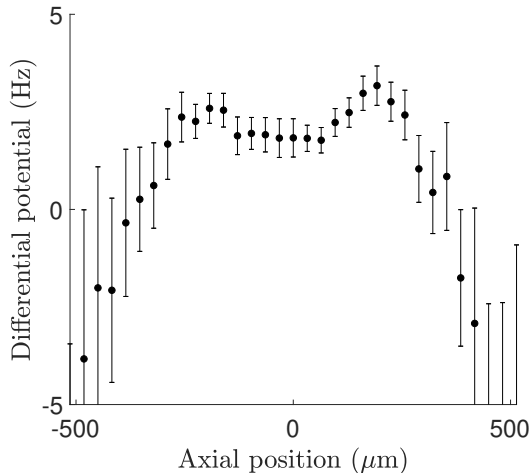


Figure 3.22: The differential potential across the cloud at the cancellation spot for a temperature of 650 nK and peak density of $2.8 \times 10^{13} \text{ cm}^{-3}$. A fit to Ramsey fringes at fixed axial positions determines the relative frequency shift across the cloud. The shape of the spatial variations across the cloud comes from the difference between the differential mean-field and Zeeman shift. Near the center of the cloud at $z = 0$, the differential potential is flat. However, far from the center the potential takes on the form of the differential Zeeman shift. The error bars are from fit uncertainties and are larger near the edges of the cloud because there is less signal at lower densities.

computed numerically. This computation is used to get the magnetic field close to the cancellation spot, but a measurement of the differential potential is still performed as an extra check.

The differential potential can be further controlled using spin-dependent potentials generated with laser light (Section 2.5). An acousto-optical modulator (AOM) deflects a laser to “paint” an intensity profile onto the atoms and alter the differential potential. The laser deflection angle is modulated by adjusting the RF frequency applied to the AOM, and the intensity of the deflected beam is modulated with the amplitude of the applied RF field. For small modulations, the amplitude modulation (AM) and frequency modulation (FM) both give a nearly linear response to the intensity and deflection angle of the laser. A spatially-varying differential potential is “painted” by applying AM and FM at 1 kHz or faster, so that the intensity pattern experienced by atoms is an average of the deflected laser intensity.

A schematic of the AOM is shown in Fig. 3.23(a), where the -1 order deflection from the AOM is used to paint a differential potential. The optics for the AOM consist of two lenses to collimate the sweeping angle of the deflected laser and to focus the sweeping beam size, shown in Fig. 3.23(b). This configuration allows the

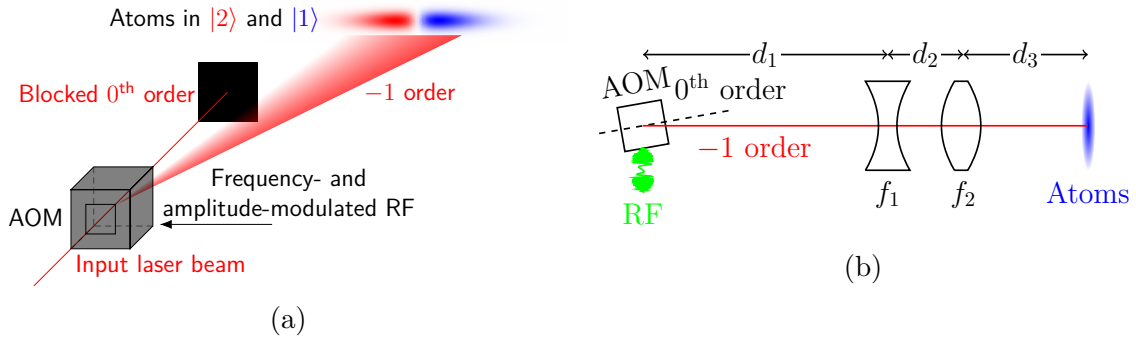


Figure 3.23: Generation of linear differential potentials with an acousto-optic modulator (AOM). (a) The AOM uses amplitude- and frequency-modulation to sweep out an intensity pattern that is sent to the atoms. (b) Schematic of the location of the two singlet lenses used to image the AOM intensity pattern. The focal lengths are $f_1 = -100$ mm and $f_2 = 100$ mm, with distances $d_1 = 416$ mm, $d_2 = 19$ mm, $d_3 = 616$ mm.

extent of laser deflection to be controlled by lens placement as well as by the FM. In addition, the various deflection angles maintain the same laser wavevector direction, so that all atoms experience the same polarization. The smallest detail is limited by the static beam size, so focusing the beam with the lens labelled f_2 allows patterns to be generated with higher resolution.

This laser painting technique can be used to create different patterns by altering the relative frequency between the AM and FM. The differential potential patterns that the AOM generates are characterized by the modulation of the laser intensity

$$I(t) = I_0 \cos(2\pi f_{AM}t + \phi_{AM}) \quad (3.24)$$

and the axial position of the laser

$$z(t) = z_{\max} \cos(2\pi f_{FM}t + \phi_{FM}), \quad (3.25)$$

where the small angle approximation is assumed for the FM deflection, and the frequency and phase of the AM and FM components are denoted (f_{AM}, f_{FM}) and (ϕ_{AM}, ϕ_{FM}) , respectively. By inverting Eqn. 3.25 and eliminating t in Eqn. 3.24, the intensity pattern as a function of axial position is

$$I(z) = I_0 \cos \left[\frac{f_{AM}}{f_{FM}} \arccos \left(\frac{z}{z_{\max}} \right) + \phi_{AM} - \frac{f_{AM}}{f_{FM}} \phi_{FM} \right]. \quad (3.26)$$

Here z_{\max} scales with FM amplitude and is increased with larger FM amplitudes until the entire cloud is swept over by the laser. For $f_{AM} = f_{FM}$, the intensity pattern reduces to

$$I(z) = I_0 \cos \left[\arccos \left(\frac{z}{z_{\max}} \right) + \phi_{AM} - \phi_{FM} \right], \quad (3.27)$$

and for $\phi_{AM} - \phi_{FM} = 0$ or π is

$$I(z) = I_0 \left(\pm \frac{z}{z_{\max}} \right). \quad (3.28)$$

Higher-order patterns can be obtained by using double- and triple-angle trigonometric formulae to obtain quadratic or cubic patterns. These higher-order patterns have been previously demonstrated up to the fourth order term [68].

The sweeping intensity pattern creates a differential potential U_{diff} given by Eqn. 2.58 and can be measured using Ramsey spectroscopy. Examples of two linear differential potential patterns with opposite signs are shown in Fig. 3.24. These linear patterns are characterized by a gradient G , which is large in these examples ($G \sim 100$ Hz/mm and $G \sim -165$ Hz/mm). See Section 6.1 for details on how these linear gradients modify spin diffusion. While the AOM is a fast and low-cost method for controlling an intensity pattern, the types of patterns that can be generated are limited. Arbitrary pulse sequences could be used to generate arbitrary patterns with an AOM, but a well-known device that is better suited for arbitrary intensity pattern generation exists, a digital micromirror device.

3.8 Digital micromirror device

Digital micromirror devices (DMD) offer arbitrary pattern control through the use of an array of individually controllable mirrors. DMDs are a well established technology that is primarily used in digital light projection applications such as in digital projectors that are found in classrooms or in cinemas. The development of high resolution and high refresh-rate DMDs makes them competitive options for advanced light control in atomic physics applications. We have implemented a DMD to replace the AOM described above. The DMD is used to easily generate arbitrary differential potential patterns.

A DMD is constructed as an array of individually controllable micron-sized mirrors, as shown up close as a cartoon in Fig. 3.25. Patterns are generated by switching each mirror to either an “on” or “off” tilt position that correspond to the mirrors

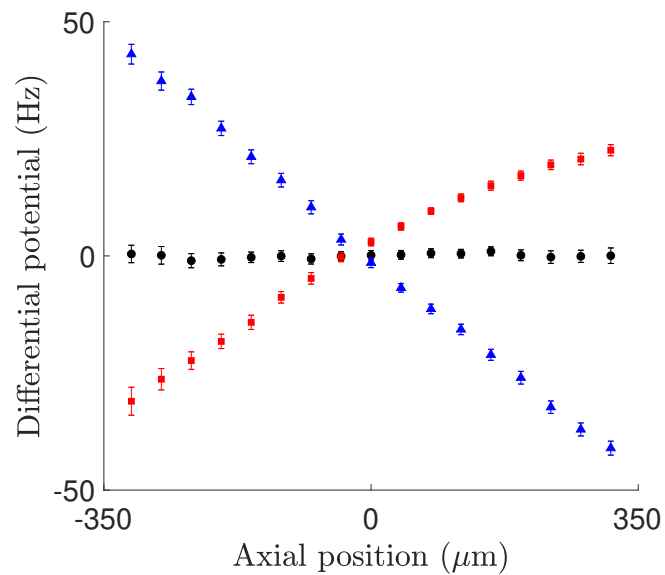


Figure 3.24: Linear differential potentials generated using AOM laser painting are measured with Ramsey spectroscopy to detect the differential potential across the cloud. The three measured differential potentials are: the unmodified differential potential (black circles), a positive linear gradient of ~ 100 Hz/mm (red squares), and a negative linear gradient of ~ -165 Hz/mm (blue triangles). Error bars represent fit uncertainties.

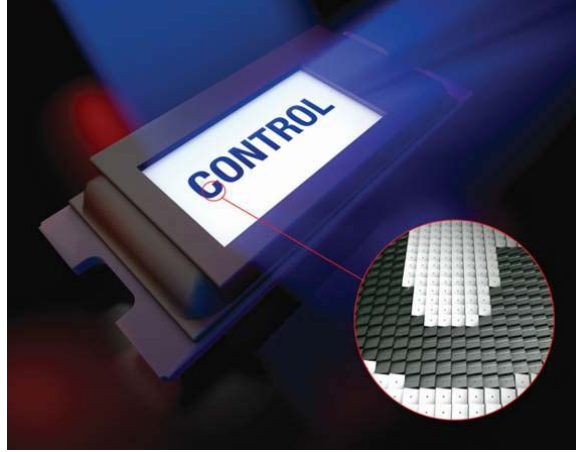


Figure 3.25: Digital micromirror devices are an array of individually controllable micron-sized mirrors. The reflected light pattern is controlled by setting the tilt of each mirror through an electrostatic interaction with nearby cathodes. The dot in the center of each mirror is a via that electrically connects the mirror to the rest of the device. This device is used to shape a light profile that creates the differential potential and initial spin preparation. Figure from Ref. [100], courtesy of Texas Instruments Incorporated.

tilting by $\pm 12^\circ$. A third mirror state with a tilt of 0° is called the float state and is used for long-time storage of the mirrors, but only the whole pattern can be switched into the float state. Each mirror is individually controlled through an electrostatic interaction, where the mirror is electrically charged, and two nearby electrodes are used to attract or repel the corners of the mirror to tilt it. The switching rate of individual mirrors can be 30 kHz or higher, but there is a settling time of around $8 \mu\text{s}$ as the mirror rings down after tilting to a new state.

Texas Instruments is currently the only manufacturer of DMDs, and their Discovery 4100 kit is a bare DMD with the accompanying control devices [101]. This kit is designed to be easy to set up for use with custom optics and control software. The Discovery 4100 DMD can be controlled through a USB connection, which is controlled by a Cypress CY7C68013A USB controller [102]. All pattern control logic is performed with a field programmable gate array (FPGA) that is programmable with custom firmware. This FPGA is called the applications FPGA and is a Xilinx Virtex 5 LX50 [103]. The DMD panel is directly controlled with another FPGA that Texas Instruments programmed and is called a DLPC410 [104]. The applications FPGA must communicate with the DLPC410 to display any DMD patterns. This kit comes with 16 general purpose input/outputs (GPIOs), eight for the USB controller and eight for the applications FPGA. These GPIOs can be used to communicate with the

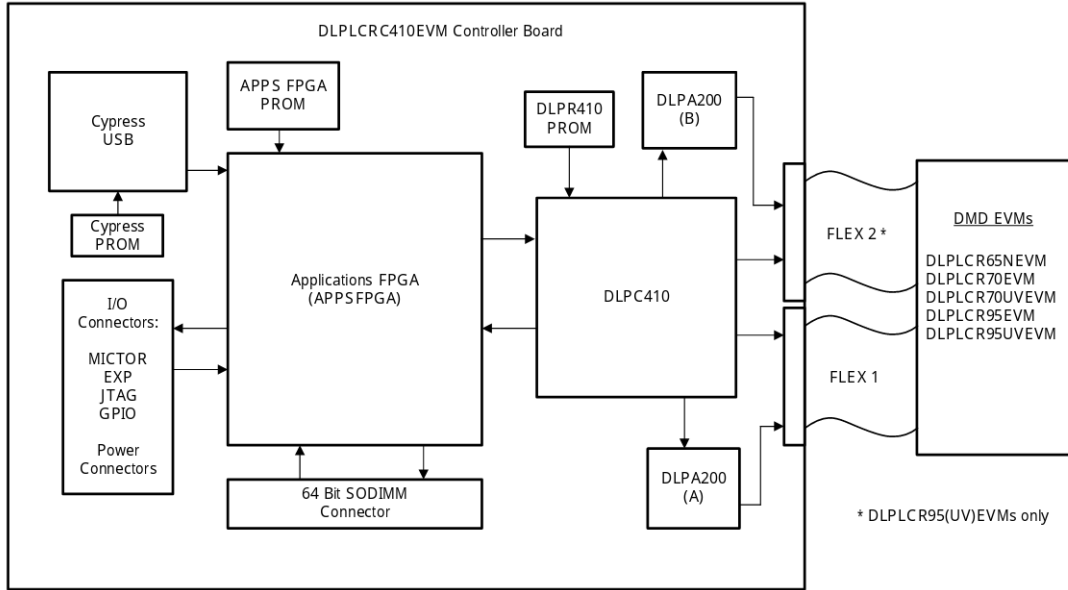


Figure 3.26: Schematic of the Discovery 4100 control board, where the main control device is the applications FPGA. The DMD pattern is updated through communication with the DLPC410 and pattern loading is performed over USB with an external computer. Figure from Ref. [101], courtesy of Texas Instruments Incorporated.

main sequencing device used in our apparatus. This GPIO signalling allows precise pattern swaps that are customizable for different experimental sequences. For pattern storage, the Discovery 4100 includes a DDR2 SODIMM slot to add up to 4 GB of RAM that can be used to store and access up to 40,000 DMD patterns at full image refresh rates of 22 kHz. An overview schematic of the Discovery 4100 control board is shown in Fig. 3.26.

3.8.1 Firmware

The applications FPGA firmware for controlling the DMD is custom and was written from scratch, so it is important to know the operation, capabilities, and limitations of this custom firmware. As an overview, the applications FPGA reads images from RAM and tells the DLPC410 to display each image on the DMD based on a specified trigger for each image. The FPGA can read and write full images to RAM on 30 μ s timescales, but when transferring images from a computer the USB connection slows this process down significantly. A custom USB driver and program is used to send images to the FPGA and into the onboard RAM, where fast pattern refresh rates are possible. The Cypress USB controller facilitates the transfer of image data and RAM location to the applications FPGA, where the pattern data is stored in RAM until

Table 3.1: USB endpoints used by the Cypress USB controller on the Discovery 4100 control board.

Endpoint	Description
0 OUT	Control endpoint for sending vendor commands
0 IN	Control endpoint for reading vendor commands
2 OUT	Sending pattern data to RAM
6 IN	Verifying pattern data in RAM
8 OUT	Programming the applications FPGA

overwritten or the power is turned off. Once given a start signal, the applications FPGA will asynchronously wait for a trigger to switch to the next DMD pattern, where the trigger can be performed with software, hardware or a time-based trigger.

The rest of this section covers the operations of the custom firmware and USB communication details. The USB protocol is well documented in Refs. [105, 106] and FPGA details are found in Xilinx’s public reference manuals [103]. The languages used to control the DMD are a mix of C/C++ [107, 108], LabVIEW [109], and VHDL [110]. Each of these technologies have a plethora of documentation that can be used to learn the operations of these technologies.

The USB driver is built with libusb, which is an open-source library for communicating over USB on all platforms [111]. The Cypress USB controller, which is a 8051 microcontroller that includes a USB peripheral, is preprogrammed with a custom USB class that opens 3 bulk USB endpoints for communications. These endpoints are summarized in Table 3.1, where the control endpoint (0 IN/OUT) was added for completeness. Endpoint 8 OUT is for programming the applications FPGA, where only the firmware needs to be sent since the Cypress controller handles the programming sequence. Endpoint 2 OUT is for writing data to the applications FPGA and is used to write pattern data to the applications FPGA that is stored in RAM. Endpoint 6 IN is used to read data from the applications FPGA, which is used to verify the patterns in RAM.

In some cases, a vendor command is required to be sent on endpoint 0 before reading or writing on another endpoint. The currently known vendor commands can be found in Table 3.2. To program the applications FPGA, the vendor command 0xBB is first sent on endpoint 0 OUT, and then the program binary is sent on endpoint 8 OUT. The binary write is immediately followed with continuous reading of the vendor command 0xBC on endpoint 0 IN until a 0x01 is read, which signals that FPGA programming is complete.

Table 3.2: USB vendor commands that can be written or read on endpoint 0 OUT or IN.

Vendor command	Description
0xBA	Read or write a custom register
0xBB	Prepare to program applications FPGA
0xBC	Check if programming is complete

Table 3.3: Custom register addresses that are sent to the applications FPGA with the 0xBA vendor command. These custom registers are user defined and could be expanded to control anything to which the FPGA is connected.

Register address	Description
0x00A1	RAM column # to read
0x00A2	RAM row # to read
0x00A3	RAM bank # to read
0x00A4	RAM rank # to read
0x00A8	Number of USB transfers to read
0x00B1	RAM column # to write
0x00B2	RAM row # to write
0x00B3	RAM bank # to write
0x00B4	RAM rank # to write
0x00B8	Number of USB transfers to write
0x00C1	Start reading from RAM
0x00C2	Start writing to RAM
0x00D3	DMD software trigger
0x00E1	FPGA software reset

The 0xBA vendor command provides control over custom registers that are listed in Table 3.3. The FPGA writes to a register when an address and value are received over USB, and the FPGA must supply the register's value when only a register address is received. These custom registers are used to tell the FPGA where in RAM the incoming pattern data should be written. The pattern data then would be sent on endpoint 2 OUT and copied into RAM. A custom register is used as a software trigger (0x00D3) for changing DMD patterns and a reset trigger (0x00E1) for resetting the FPGA logic. Custom registers can be expanded to control any electronic device the applications FPGA can access through the eight GPIOs.

The applications FPGA only communicates over USB for configuring the specific patterns to display. After sending the pattern data, the DMD can operate independently of the USB connection during an experiment. The firmware on the FPGA is responsible for the high-speed control of the DMD image. This firmware is written

with a hardware description language that is programmed with a series of digital logic blocks that are stitched together and mapped onto real logic gates in the FPGA. This firmware is in charge of reading and writing data to the USB controller, the RAM, and the DLPC410 FPGA. It must also monitor the relevant GPIO to react quickly to when an image change signal is received. Two of the eight GPIOs are used, one for hardware triggering to switch to the next image and the other GPIO for resetting the DMD to the first pattern in the sequence. Each pattern is stored in 13 rows of RAM, where the first row is configuration data and the remaining 12 rows are the pattern data. The 13 rows for each pattern corresponds to 104 KB of RAM, where there is 8 KB of configuration data and 96 KB of pattern data. The slow part of using all 40,000 patterns is the long time required for that many patterns to be transferred over USB to the RAM used by the applications FPGA. Typically, we only need a few images to perform an experiment and this takes about one second to transfer the pattern data. There are some optimizations that could be made to speed up the USB communication protocol if a larger pattern sequence is needed. The USB connection was tested using a known pattern until the pattern was displayed on the DMD. Using our custom firmware, the first pattern displayed on the DMD at the full 22 kHz refresh rate is shown in Figure 3.27.

During a typical experimental run, a list of patterns and triggers are first loaded onto the DMD and the main control software sends hardware triggers to control the DMD patterns. Two GPIOs are used for two hardware triggers, one to trigger the DMD to advance to the next image and another to trigger the DMD to return to the first image. After sending a trigger to the DMD, a new pattern is displayed within 50 μ s for the next pattern trigger, and 100 μ s for the return to first image trigger.

3.8.2 Optics

There are two main ways to image a DMD: direct imaging [112] and Fourier imaging [113, 114]. Direct imaging treats the DMD as the object plane and the DMD pattern is focused directly onto the atom cloud so that the pattern at the DMD is similar to the pattern at the atoms. In Fourier imaging, the DMD is the object plane, but the atoms are placed in the Fourier plane one focal length away from a lens so that the pattern at the atoms is the Fourier transform of the DMD pattern. While Fourier imaging has the advantage of maximizing power delivery, the DMD in this thesis is imaged directly because of the simplicity of pattern control and optics.



Figure 3.27: The first pattern displayed on the DMD at a 22 kHz refresh rate. A custom USB driver and FPGA firmware was required to achieve the specified DMD pattern refresh rates.

The available optics for our system are constrained because of the lack of physical space around the science cell. The MOT coils need enough space to surround the science cell when transferring atoms, and the only empty side is already used for imaging atoms. While it is possible to share the imaging lens for imaging and DMD pattern purposes, it is not optimal because the light used in both paths have a similar frequency. This limits the possibility of using a dichroic mirror to combine the optical paths, and one optical path would have to enter at an angle, reducing the quality of that image. Instead, a new optical path was used that places the last lens at least 7 inches away from the science cell to give the MOT coils enough clearance. The 7-inch working distance limits the focal length of the DMD imaging lens to focal lengths larger than 7 inches (178 mm). The other requirement is to obtain a magnification of the DMD image that makes the most use of the available resolution. A magnification of $1/12$ maps the DMD pattern onto a 1.4 mm length of the atomic cloud. For a cloud at $T = 650$ nK, a DMD pattern that is 1.4 mm long covers an axial distance of $7z_0$, which is 99.95% of the cloud. At this magnification each DMD mirror maps onto a $1.1 \mu\text{m}$ pixel in the image plane.

Given the restrictions described above there are not many valid optical configurations to image the DMD. Optical systems consisting of one, two or three lenses were explored and optimized numerically by considering the fraction of captured light and the tunability of the magnification. While two or three lens configurations do increase the tunability of the magnification, a single lens always captures the most light in this case. This may seem counter-intuitive, but the reflected light from the DMD is specu-

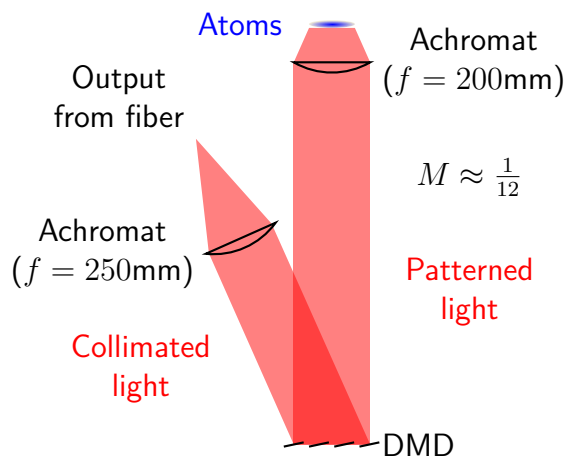


Figure 3.28: Direct imaging of the DMD pattern onto atoms using two achromatic doublets to reduce spherical aberrations. Laser light exits a single-mode fiber and is collimated with a $f = 250$ mm doublet and incident on the DMD at 24° . This collimated light is reflected off of the DMD mirrors, where the mirrors in the “on” state reflect the light normal to the DMD panel surface. This light is collected and imaged by a second doublet lens with $f = 200$ mm that is placed 2600 mm away from the DMD. The DMD pattern is imaged onto the atoms 217 mm away and with a magnification of $1/12$.

lar and not diffuse, so the reflected light is roughly collimated since the incoming light is collimated. Diffraction effects, scattering, and Gaussian beams not being perfectly collimated lead to some spread in the light profile over long distance, but it is minimal over the distances used here. A single lens is used to image the DMD pattern since it provides the highest amount of light captured and best optical resolution possible.

The single lens is placed 2,600 mm away from the DMD and about 217 mm from the atoms for a magnification of $1/12$. A schematic of the DMD optics is shown in Fig. 3.28, where the DMD is illuminated with a collimated Gaussian beam that has a $1/e^2$ width around 23 mm and an incident angle near 24° . The illuminating light is formed with light exiting a single-mode fiber that then expands into a 250 mm focal length lens used to collimate the expanded light. Both the imaging and collimating lenses are achromatic cemented doublets, which reduces the amount of spherical aberrations in addition to chromatic aberrations. Spherical aberrations are a significant limiting factor here since the images fill the majority of the lens, making gradient index lenses a reasonable upgrade path in the future. The imaging lens is mounted onto a translation stage with a micrometer to control the translation. The process of focusing the DMD image is detailed in Section 4.6, where typical FWHMs are $25 \mu\text{m}$ in the plane of the atoms.

The small mirrors on the DMD act as a grating that can lead to significant diffraction effects. The DMD diffraction should be optimized to line up the reflected DMD pattern with a diffraction peak, obtaining the most laser power possible in the reflected path. When the diffraction pattern and reflected light are aligned, this configuration is called a blazing condition [115, 116] for the diffraction grating. The m^{th} diffraction order is peaked at an outgoing angle of

$$\theta_m = \arcsin \left(\frac{m\lambda}{d} - \sin(\theta_i) \right), \quad (3.29)$$

with λ the wavelength of light, d the spacing between mirrors, and θ_i the incident angle. The DMD is a 2D grating with mirrors that rotate on an axis at 45 degrees to the mirror grid, so there are two angles that should be considered: θ_m and θ_n for the two dimensions. Because of this rotated geometry, the specular reflection can only be peaked for diffraction orders with the same order in both directions, $m = n$. The angles of the diffracted orders can be computed for $\lambda = 780$ nm after converting the mirror spacing size $d \rightarrow d/\sqrt{2}$ to accommodate for the 45° axis rotation. For an incident angle of $\theta_i = 24^\circ$, the 5th order diffraction peak is reflected at 0.2° from the panel normal, which is close enough to 0° that minimal power is lost for this configuration.

3.8.3 Error diffusion

Binary images can only toggle the intensity of each pixel on or off, making it difficult to smoothly vary the image pattern. By increasing the number of bits stored for each pixel, an 8-bit image can have pixels with values ranging from 0 to 255. An 8-bit image allows for smoothly varying patterns. Using the DMD to display an 8-bit pattern requires fast pattern switching through eight images to time average the intensity pattern and have resolution of the laser intensity at the atoms. An 8-bit pattern completes a full eight image pattern cycle in about 10 ms, which is too close to the spin diffusion timescales, so time averaging is not appropriate. Binary patterns are static patterns with each mirror either on or off, and can be toggled 256 times faster. This section discusses a technique that uses binary patterns to generate N -bit intensity patterns at the atoms, where N can easily vary from 1 to 8. This error diffusion process requires the DMD imaging resolution to be larger than a single mirror, so that a group of mirrors can be used to generate discrete intensities across the pattern.

The imaging lens is mounted onto a translation stage with a micrometer to control the translation. To focus the DMD image, the lens position is adjusted until the feature size on the atoms is the smallest possible, see Section 4.6 for DMD focus details. The best DMD focus achieved so far had a point spread function (PSF) with a FWHM of $25\ \mu\text{m}$ (see Section 4.6).

Since the DMD focus can reach FWHMs of about $25\ \mu\text{m}$, the point-spread-function is spread over approximately 20 by 20 mirrors. These 400 pixels are averaged by using error diffusion to apply greyscale light with a binary DMD pattern, at the cost of spatial resolution. This process is used to convert greyscale images into binary images that can be displayed at a faster rate on the DMD. For example, using error diffusion and averaging over an area of 400 mirrors is effectively a $\log_2(400) \sim 8$ -bit greyscale image, but the pattern displayed on the DMD would be a single binary image. Without the use of error diffusion, 8-bit greyscale images would be displayed at 86 Hz, 256 times slower than the binary pattern refresh rate. Greyscale images and error diffusion can be combined together to tune the effective bit depth of each DMD pattern. Higher bit depths should be used for DMD patterns with large intensity variations while low bit depths are appropriate for patterns that require a single pattern or fast refresh rate.

The error diffusion process rounds each pixel value to a minimum and maximum value and then keeps track of the difference or error the rounding caused. This error is propagated to adjacent pixels that have not yet been rounded. A kernel describes the way the error is diffused to neighbouring pixels and typically the errors diffuse from the one corner of the image to the other corner. One of the most well-known error diffusion protocols is the Floyd-Steinberg algorithm [117] with kernel

$$k = \frac{1}{16} \begin{pmatrix} - & \# & 7 \\ 3 & 5 & 1 \end{pmatrix}, \quad (3.30)$$

where # represents the current pixel whose error is being propagating, - represents the pixel to the left of the current pixel and has already been processed. The kernel k is normalized $\sum_{i,j} k_{ij} = 1$ so that the total error is conserved. The kernel only has elements for pixels that have not yet been rounded. It is assumed that the rounding procedure starts in the top left corner and works towards the bottom right corner of an image.

The Floyd-Steinberg kernel and other kernels [118] were tested and all work relatively well for a region of 20×20 arrays of pixels. Unfortunately, many of the kernels

that were tried produced image artifacts that were noticeable by eye. The Sierra kernel [119] eliminated most of these artifacts in the relevant sample images used in this work. The Sierra kernel is

$$k = \frac{1}{32} \begin{pmatrix} - & - & \# & 5 & 3 \\ 2 & 4 & 5 & 4 & 2 \\ 0 & 2 & 3 & 2 & 0 \end{pmatrix}. \quad (3.31)$$

The effect of using Sierra error diffusion for a spin preparation DMD pattern generated from a hyperbolic tangent function is shown in Fig. 3.29. Zoomed out, it is hard to notice any effect of error diffusion, but when zoomed in to where individual pixels can be resolved, an error diffusion pattern is visible. The light profile at the atoms is effectively blurred over 20 mirrors by the imaging resolution, which causes the atoms to experience the smoothed intensity pattern.

Improvements on error diffusion could be made by changing the direction of error propagation [120, 121] or using a kernel designed for optimizing around 20×20 macropixels called block error diffusion [122]. Block error diffusion could improve the error within a user-specified shape and could be changed if the PSF of the DMD optics is changed.

Linear differential potentials were tested with the DMD and measured with Ramsey spectroscopy as in Fig. 3.30. The quality of differential potentials created with the DMD is comparable or better than the differential potentials created with the AOM (Fig. 3.24). In this thesis, the DMD is used to create spin profiles and differential potentials in Section 6.4. In Chapters 5 and 6, the AOM (Section 3.7) and masking (Section 3.2) techniques are used for generating differential potentials and spin preparation, respectively.

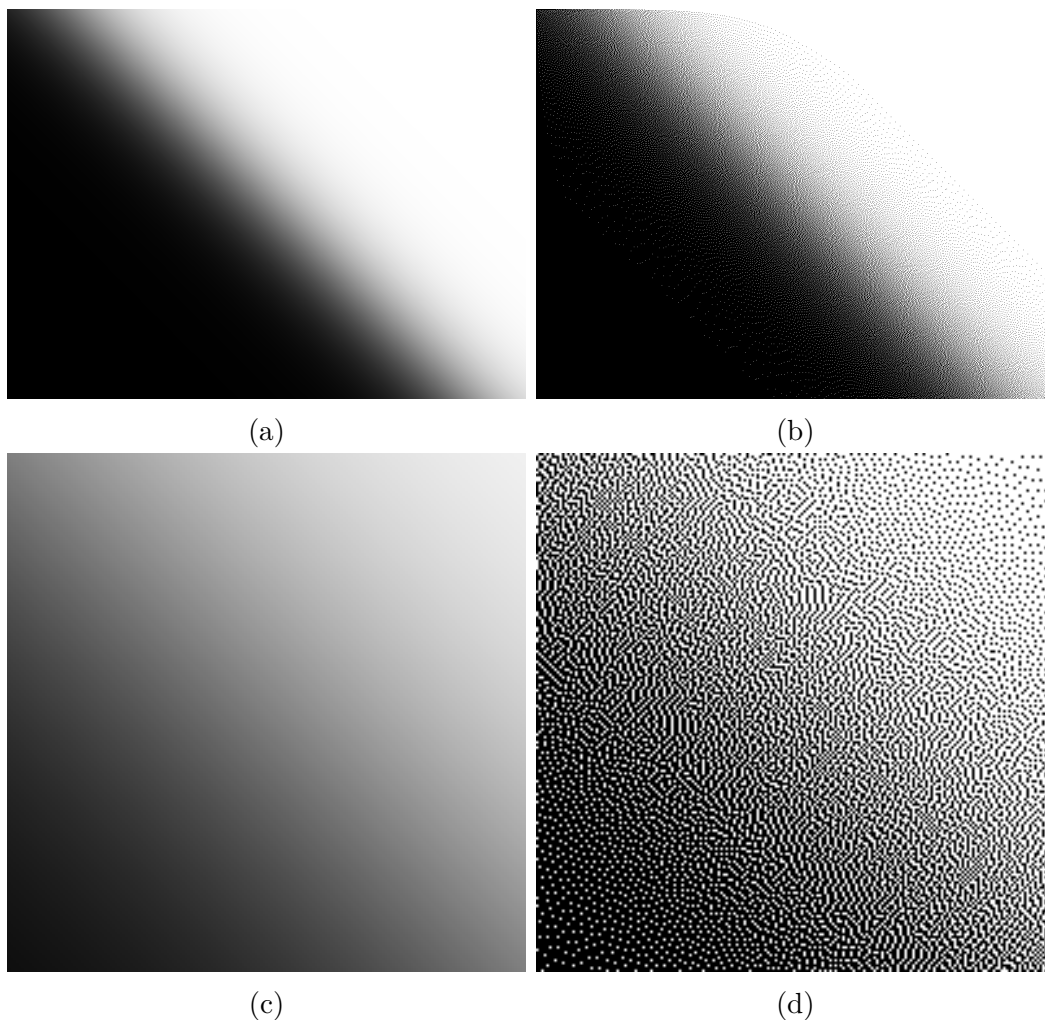


Figure 3.29: Sierra kernel error diffusion with a typical spin preparation pattern. (a) The full 8-bit image and (b) full dithered image look approximately the same when the individual pixels are not resolvable. Zooming in to an area of 200×200 pixels highlights the difference between the (c) 8-bit and (d) dithered image. Each pixel in the dithered image is either on (white) or off (black), where each pixel in the 8-bit image has a greyscale value of 0-255. The dithered image can be displayed at binary pattern refresh rates with a light profile that is roughly the same as the 8-bit image.

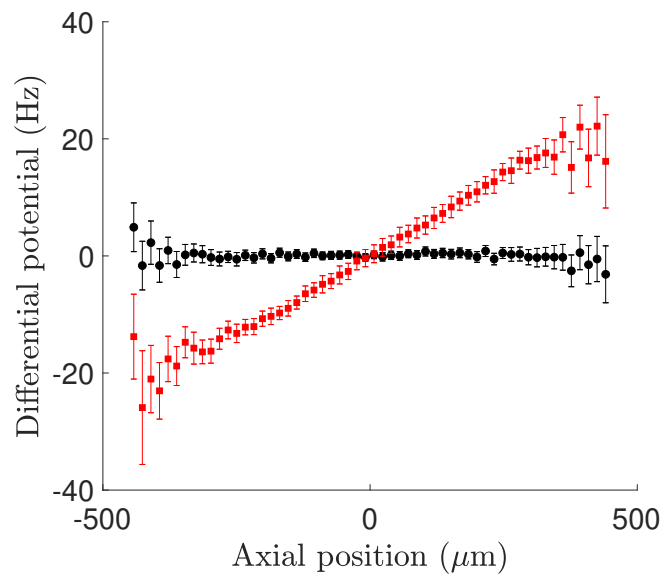


Figure 3.30: A DMD generated linear differential profile (red squares) using binary patterns that were created from error diffused greyscale patterns. The differential potential without light is shown with black circles. The quality of the linear potential is typically better than the differential potentials generated with the AOM technique. The DMD pattern could be further tweaked to correct for minor discrepancies in the potential.

Chapter 4

Calibrations

There are a few calibrations that should be occasionally performed for smooth operation of the experiment. When done correctly, these calibrations will optimize the efficiency and reliability of the experiment, making it easier to consistently study atomic clouds at a particular temperature and density. Occasional recalibration is required because of thermal drifts that change optical alignments, fiber coupling efficiencies, and the magnetic bias field. This section is meant to be used as a reference to look up how and when to perform these calibrations and to ensure the experiment is operating smoothly. Calibrations in this experiment are iterative since each calibration depends on another, and regular checks go a long way to help stability and quality of calibrations and data collection.

4.1 Magnetic trap frequencies

Calibration of the axial and radial magnetic trap frequencies is crucial for calculating the temperature and density of a trapped gas (see Eqns. 3.11 and 3.12). The trap frequencies are measured by briefly shifting the center of the magnetic trap and observing the oscillation frequency of the center of mass of the cloud in the original trapping potential. The momentary shift of the trap center provides a momentum kick to the center of mass of the cloud, which starts an oscillation that is large enough to be detected. The momentum kick is applied with a small magnetic field coil placed close to the atoms as shown in Fig. 4.1. The difference between the axial and radial trap frequency measurements is the orientation of the coil, which changes the magnetic field shift and the direction the trap center shifts. Since the radial component of the magnetic field is a quadrupolar field, a magnetic field offset is only required to shift the radial cloud center. This is an important distinction as we apply a magnetic field

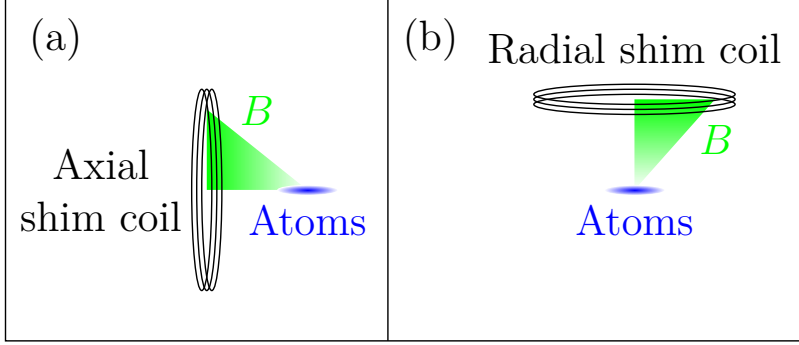


Figure 4.1: Magnetic field coil placement to measure the radial and axial trap frequencies. A momentary magnetic field bias (gradient) kicks the atomic center of mass along the radial (axial) coordinate. The cloud then oscillates in the original trap and the center of mass is measured. An (a) axial or (b) radial coil is placed a few centimeters from the atoms to provide both a field gradient and a field bias.

gradient along the radial coordinate, but the cloud is radially small so the field is approximately constant. In contrast, a magnetic field gradient is required to shift the axial cloud center because the axial component of the magnetic field has no zero-crossing. The radial trap frequency measurement uses the same shim coil used to prevent atoms falling due to gravity during free expansion (Section 3.3.1). For the axial trap frequency, a temporary coil is added close to the science cell to provide the momentum kick in the axial direction. One should be careful that the momentum kick is large enough to measure and small enough that the gas remains in the harmonic region of the magnetic trap. Additionally, the oscillations should be small enough that the cloud remains within the field of view of the imaging camera and a full oscillation can be observed.

The axial and radial center of the cloud are measured by fitting the atomic density with a Gaussian and extracting the Gaussian center fit parameter. The center of the cloud is tracked in time, and the oscillation within the trap is fitted to a sine. An example of a radial and axial trap frequency measurement is shown in Fig. 4.2, where an oscillation of the center of mass is observed. This oscillation is fitted to a sine function $A \sin(2\pi ft + \phi) + y_0$ using a four parameter fit for A , f , ϕ , and y_0 . Typical fitting errors on the trap frequency are lower than one percent. From these fits the radial and axial trapping frequencies are $f_\rho = 247.8(1)$ Hz and $f_z = 6.723(6)$ Hz.

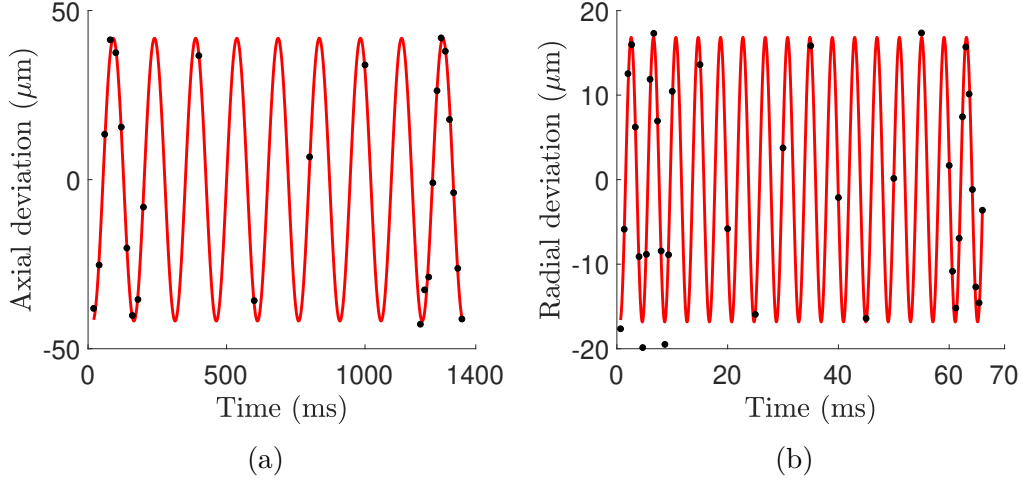


Figure 4.2: An example of (a) axial and (b) radial trap frequency measurement. The center of mass motion is plotted after receiving a small kick in either direction, and then fitted for a sine function. The fitted frequency of the center of mass motion is the trap frequency in each direction.

In addition to better accuracy in measuring the density and temperature, the radial trap frequency is used to calculate the magnetic field gradient of the trap [84, 95]

$$B' = 2\pi f_\rho \sqrt{\frac{mB_0}{m_F g_F \mu_B}}, \quad (4.1)$$

where B_0 is the bias field. This parameter is useful for camera magnification in Section 4.7. Note that this equation also shows how the bias field changes the radial frequency $2\pi f_\rho = \sqrt{\frac{\mu_B m_F g_F}{m}} \frac{B'}{\sqrt{B_0}}$. Any changes in the bias field will require a recalibration of the radial trap frequency. The bias field can drift over time, but usually it is intentionally changed to operate at the cancellation spot, requiring a radial trap frequency calibration.

The axial trap frequency is used throughout the rest of the experiment for obtaining the temperature of the cloud. The axial trap frequency should not change with bias field because the relationship is [95]

$$2\pi f_z = \sqrt{\frac{g_F m_F \mu_B B''}{m}}, \quad (4.2)$$

where $B'' = \frac{\partial^2 B}{\partial z^2}$ is the axial curvature of the magnetic field. Periodic checks on the axial trap frequency ensure that the cloud temperature measurements are accurate, and can be helpful when diagnosing coil integrity. The axial trap frequency drifts

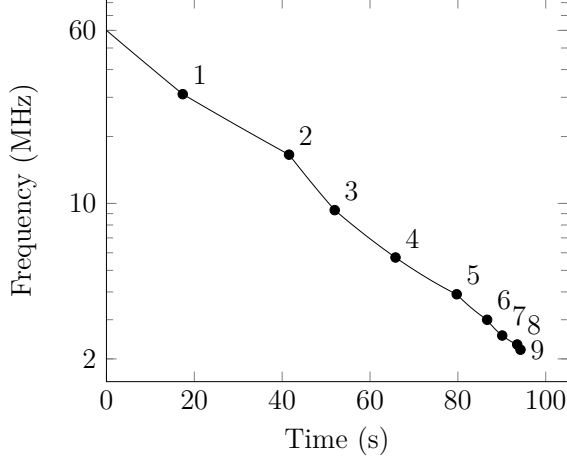


Figure 4.3: Evaporation frequency as a function of time over 9 stages, where the end of a stage is labelled with a number and circle. Each stage reduces the evaporation frequency by half of the frequency difference to the trap bottom. During each stage, the frequency is reduced along an exponential sweep to allow time for thermalization between stages. The y-axis is log-scaled.

when the axial curvature drifts, which is a rare occurrence that only happens when the coils shift position or the current through them is changed. Since the value of the axial trap frequency rarely drifts, recalibration is performed less often than the radial trap frequency calibration.

4.2 Radio frequency evaporation and trap bottom

Obtaining a consistent temperature and density requires the optimization of the radio frequency (RF) evaporation parameters, namely the frequencies, timing, and power applied at each evaporation stage. Each evaporation stage applies a frequency sweep from an initial frequency to halfway to the specified trap bottom. Evaporation includes 9 evaporation stages, starting at 60 MHz and cutting down to around 2.20 MHz with a trap bottom of $\nu_{\text{bottom}} \sim 2.09$ MHz. The final frequency of each evaporation stage is calculated using

$$\nu_i = \frac{\nu_{i-1} - \nu_{\text{bottom}}}{2}, \quad (4.3)$$

and the frequency cuts in time are shown in Fig. 4.3.

The trap bottom is measured by lowering the last evaporation cut until no atoms remain in the trap. The trap bottom is the energy difference between the $|F = 1, m_F = -1\rangle$ and $|F = 1, m_F = 0\rangle$ states, which is given by $h\nu_{\text{bottom}} = \mu_B m_F g_F B_0$.

For a typical bias field of $B_0 \sim 3$ G, the trap bottom is near $\nu_{\text{bottom}} \sim 2$ MHz. The trap bottom requires adjusting every time the bias field changes.

To calibrate the evaporation parameters, the power and timing of each stage is optimized for a cloud with maximized atom number. The stage that is being tuned for maximum atom number should be the penultimate evaporation stage so that the cloud temperature is fixed by the final stage. The RF power and cut timing of the tuned stage should be changed by factors of 2, since evaporation is insensitive to smaller changes. All nine stages are tuned in this manner, where a tenth stage is added to fix the temperature for optimizing the ninth evaporation stage.

Sometimes it is beneficial to operate away from the optimized evaporation parameters, such as when the experimental cycle time must be reduced or when operating at temperatures near degeneracy. About 20 seconds per cycle could be saved if evaporation was less efficient during the first few cuts, but then the highest cloud densities would be out of reach. Near degeneracy, a fast linear cut limits the time for three-body recombination in a BEC, which dominates the losses at those higher densities.

4.3 Magnetic bias field

Calibrating the magnetic bias field is required to ensure operation at the cancellation spot when working at different cloud densities and temperatures. The cancellation spot shifts by a small amount when the density or temperature of the cloud is altered since these changes modify the density profile, altering the mean-field shift. The bias field scales linearly with the applied current to the bias coils, which is controlled with a voltage signal. The bias field is parameterized with the bias voltage signal $B_0 = a_1 + a_2 V_{\text{bias}}$, where a_1 and a_2 correspond to the bias field at zero current and the sensitivity of the bias current, respectively. The units of a_1 and a_2 are gauss and gauss/volt.

The parameters a_1 and a_2 are determined by varying the bias voltage and measuring the quadratic Zeeman shift between the $|F = 1, m_F = -1\rangle$ and $|F = 2, m_F = 1\rangle$ states using Ramsey spectroscopy. The energy difference from zero field is calculated and subtracted from the frequency obtained by adding up the frequencies of the two-photon transition and the measured Ramsey frequency. The measured Ramsey frequency is the two-photon detuning of the two-photon transition, so this summed frequency is the difference between the two states at the current magnetic field. The

frequency difference between the two states as a function of magnetic field B is

$$\Delta\nu(B) = \nu_{\text{Ramsey}}(B) + \nu_{\text{RF}} + \nu_{\mu\text{W}} - \Delta\nu_{2-1}(B=0), \quad (4.4)$$

where ν_{RF} and $\nu_{\mu\text{W}}$ are the frequencies of the RF and microwave fields used in the two-photon Ramsey sequence, ν_{Ramsey} is the measured Ramsey frequency, and $\Delta\nu_{2-1}(B=0)$ is the $|1\rangle$ to $|2\rangle$ transition frequency at zero field. One needs to be careful here to ensure that the sign of ν_{Ramsey} is correct. The parameters a_1 and a_2 are found by fitting the data to

$$\Delta\nu(B) = \Delta\nu_{2-1}(B = a_1 + a_2 V_{\text{bias}}) - \Delta\nu_{2-1}(B = 0), \quad (4.5)$$

where $\Delta\nu_{2-1}(B)$ is the $|1\rangle$ to $|2\rangle$ transition frequency at magnetic field B . This transition frequency is calculated with the Breit-Rabi formula (Eqn. 3.22). The result of one instance of this calibration is shown in Fig. 4.4, where the measured transition frequency relative to the zero-field transition at the center of the cloud is plotted and fitted. From the data shown, $a_1 = 47.4(2)$ G and $a_2 = -10.69(5)$ G/V where the uncertainties are from fitting uncertainties. These calibration parameters are used to quickly adjust the bias field to the cancellation spot when changing density or temperature. Each change in bias field is confirmed to be at the cancellation spot with Ramsey spectroscopy.

4.4 Adiabatic rapid passage

The adiabatic rapid passage (ARP) frequency must be set correctly for efficient transfer of $|F = 1, m_F = -1\rangle$ atoms to $|F = 2, m_F = -2\rangle$. The ARP microwave frequency is tuned to a maximum in atom number as measured in Fig. 4.5, where a frequency near 6828.85 MHz corresponds to the peak. The width of the atom number plateau depends on the width of the bias field sweep, where a larger bias field sweep corresponds to a less sensitive ARP frequency. Narrow bias field sweeps are more sensitive to the exact microwave frequency, but can quickly transfer atoms. This is useful for limiting the time before imaging. Whenever the bias field changes, the ARP frequency needs to be recalibrated. Typically, we sweep the bias field by about 0.4 G in 0.6 ms.

The bias field sweep should be large enough that the entire cloud undergoes an ARP and not just a portion of the cloud at higher or lower magnetic field. For sweeps that only address a portion of the cloud, the measured temperature will increase or

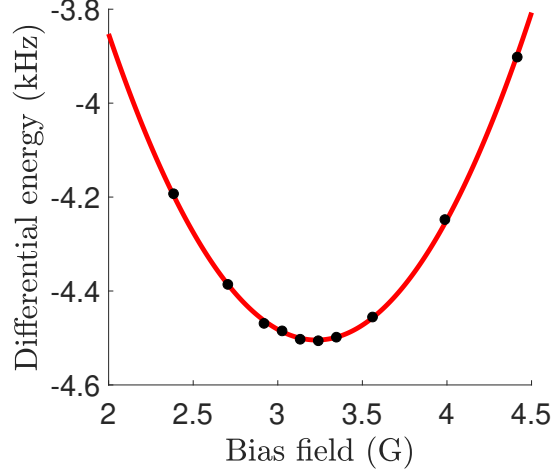


Figure 4.4: Calibration of the magnetic bias field using the change in the differential potential U_{diff} between the $|F = 1, m_F = -1\rangle$ and $|F = 2, m_F = 1\rangle$ states compared to the zero-field energy difference. Each point is from a fit to Ramsey fringes at the center of the cloud, where the fitted frequency is combined with synthesizer frequencies and subtracted from the zero-field transition frequency. The line is a fit to the Breit-Rabi formula with $B_0 = a_1 + a_2 V_{\text{bias}}$, where the fit parameters are found to be $a_1 = 47.4(2)$ G and $a_2 = -10.69(5)$ G/V.

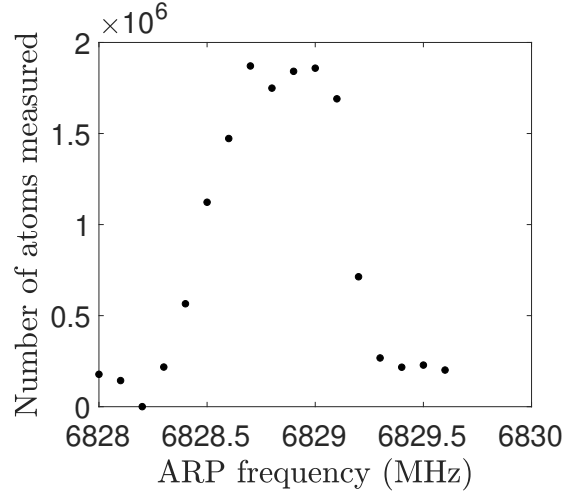


Figure 4.5: Calibration of the microwave frequency used for adiabatic rapid passage. As the frequency is tuned, the measured atom number is maximized when the entire cloud is transferred to the $|F = 2, m_F = -2\rangle$ state. The width of the peak in atom number depends on the range of a bias field sweep. The ARP frequency should be set in the middle of the plateau, which is around $\nu_{\text{ARP}} = 6828.85$ MHz in this example.

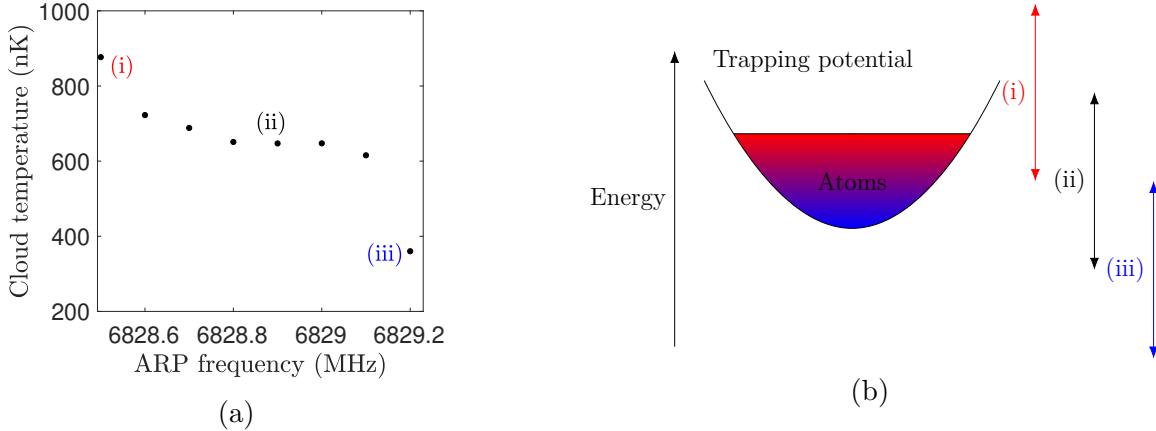


Figure 4.6: (a) The measured cloud temperature as a function of tuned ARP frequency. The measured temperature of the cloud is either (i) cooler, (ii) the same, or (iii) hotter than the true cloud temperature. (b) The three measured temperature cases are illustrated for harmonically trapped atoms, where the energetic atoms venture further from the trap center. The energy of atoms selected for ARP frequencies that are (i) low, (ii) central, and (iii) high. The atoms corresponding to these ranges are transferred with an ARP and imaged. The entire cloud should be transferred for an optimal ARP and correct temperature measurements.

decrease as shown in Fig. 4.6(a). The measured temperature is hotter at a low ARP frequency and colder at a high ARP frequency. When the ARP frequency is slightly off, the atoms that undergo an ARP are selected by their potential energy. The magnetic trapping potential with atoms populating the harmonic oscillator energy levels is shown in Fig. 4.6(b), where the hotter atoms spend more time at higher potentials and the colder atoms are typically closer to the potential minimum. For the three different ARP frequencies (i,ii,iii) a different energy range of atoms undergoes an ARP. For (i) a low ARP frequency, the higher energy atoms are selected leading to a higher measured temperature. For (iii) a high ARP frequency, the lower energy atoms are selected and the cloud is measured to be colder than the actual temperature. For (ii) a middle ARP frequency, all of the atoms are transferred to $|F = 2, m_F = -2\rangle$ and the true temperature is measured. The ARP frequency and bias field sweep size must be calibrated to ensure temperature and atom number measurements are accurate.

4.5 Probe local oscillator frequency

The probe laser is frequency-locked using a beatnote lock with the cooling laser, which allows fine control over the probe frequency by tuning the frequency of an RF local

oscillator (LO). The probe frequency must be resonant with the cycling transition during imaging to ensure detection of all of the atoms in the cloud. This resonance is found by varying the LO frequency to locate the resonant probe frequency that detects the maximum number of atoms. The number of atoms measured as a function of LO frequency is a Lorentzian

$$N(f_{\text{LO}}) = N_0 \frac{\left(\frac{\Gamma}{2}\right)^2}{(f_{\text{LO}} - f_c)^2 + \left(\frac{\Gamma}{2}\right)^2}, \quad (4.6)$$

where the data is fitted for the center LO frequency f_c , the transition width Γ , and the number amplitude N_0 . The transition width corresponds to the natural linewidth for ^{87}Rb , $\Gamma = 6.06$ MHz, and the center frequency sets the probe LO frequency for future imaging. Figure 4.7 shows an example of this process, where the fitted center that the probe LO is set to is $f_c = 316.2(1)$ MHz. The fitted width of the Lorentzian was $6.7(5)$ MHz. While this example uses a thermal cloud at 650 nK, any other thermal cloud or a BEC could be used to measure the center probe LO frequency. Calibration of the probe LO frequency should be performed anytime there is a drift in the magnetic bias field during imaging or when the cooling laser lock changes the relative frequency between the cooling and probe laser.

4.6 Imaging camera and DMD image focus

The image quality of the atomic cloud is important for accurately measuring cloud temperature and density. The image is blurred if the camera is out of focus, and larger temperatures and lower densities than the true values will be measured. The depth of focus for the imaging system is large (~ 20 mm), by design, so that the exact position of the camera does not require fine positioning. To locate the camera focus with atoms, we image the smallest atomic cloud and minimize the cloud size by moving the camera position. This process minimizes the point-spread function of the optical path by searching for the minimum cloud size. The cloud is smallest when imaged within the trap and with no expansion, and a small feature size to minimize around is the radial cloud width. Any improvement in focus should reduce both the radial and axial widths. While one could optimize around the axial width, the relative change in size is higher with the radial width so we focus on minimizing the radial width.

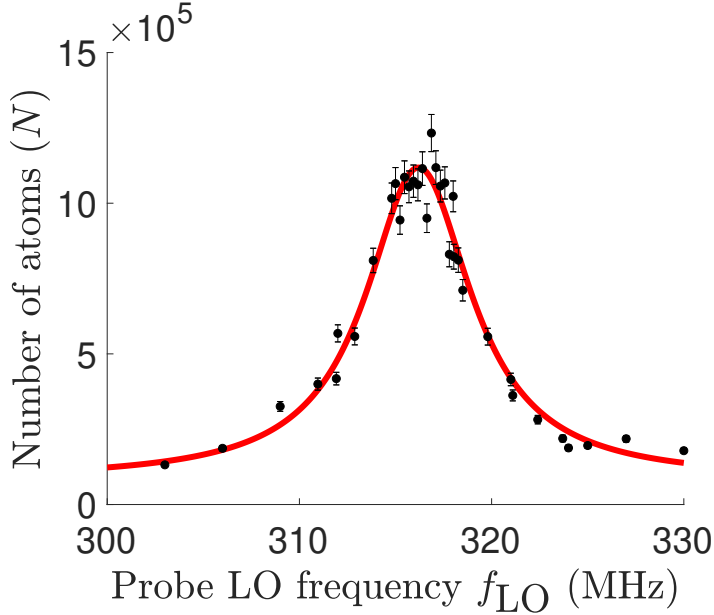


Figure 4.7: Calibration of the local oscillator (LO) used to lock the probe laser frequency. The LO frequency is varied and the number of atoms is measured. The maximum number of atoms is the optimal LO frequency. A fit to Eqn. 4.6 is shown, where the center frequency was found to be $f_c = 316.2(1)$ MHz. Error bars on each point are $\pm 5\%$, which represents the shot-to-shot noise.

The imaging camera is on a translation stage, which is used to move the camera until the radial width is minimized. An example of this camera focus calibration is shown in Fig. 4.8. Far away from focus there is a clear trend in the radial width, where the camera is moved to minimize the radial width. Near the focus there is minimal change in the radial width over 15 mm, so the placement of the camera is not important over that range of distances. The camera was placed at the focal point in roughly the center of this 15 mm region with constant radial width. The temperature of the thermal cloud used here was 650 nK, which corresponds to a radial width of $\sim 5 \mu\text{m}$, which is smaller than the measured radial widths. Image focus calibration requires low noise on the measured cloud size, which provide low noise on the location of the focal point. Calibrations of the evaporation, trap bottom, ARP, and probe all help to reduce shot-to-shot noise and should be updated before starting to calibrate the camera focus.

The depth of focus for the DMD is much smaller (~ 0.38 mm) than the imaging camera, so focusing the DMD image onto the atoms is more sensitive to the lens position. To focus the DMD pattern, the light intensity from the DMD pattern is mapped to an atomic profile that can be imaged with the already-focused camera.

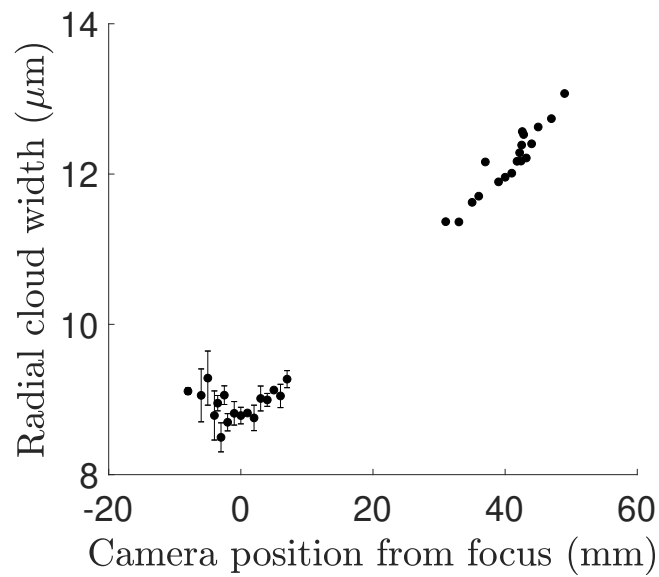


Figure 4.8: Camera focus calibration by moving the camera position and measuring the radial size of a thermal cloud. Optimal focus is found where the radial width of the cloud is minimized. Near focus, the radial width of the cloud is insensitive to camera movement of ± 10 mm. The error bars correspond to a standard deviation of three repeated measurement near focus, whereas away from focus only single measurements were collected.

This mapping is performed by using the DMD pattern to create a spin-dependent potential that alters the transverse phase precession during Ramsey spectroscopy (see Sections 2.5 and 3.5.2). By applying the DMD light to the atoms in between the two $\pi/2$ -pulses in Ramsey spectroscopy, the transverse phase will wrap faster (or slower) where light is present in the cloud. This phase wrapping frequency is controlled by the DMD laser intensity and the DMD pattern. The quality of focus controls the spatial extent of where light is present at the atoms. For a DMD pattern with a small feature size, the spatial extent of the phase wrapping is minimized to find optimal DMD focus.

The measurement of the spatial extent of the phase wrapping is performed with a single shot of Ramsey spectroscopy. In the final $\pi/2$ -pulse of Ramsey spectroscopy the wrapped phases are rotated in the Bloch sphere, converting the phase variations to longitudinal spin variations and projected onto the $|1\rangle$ state. The unperturbed spins are specifically rotated so that they end up in the $|2\rangle$ state by wrapping the phases of these spins by $2n\pi$, where $n = 1, 2, \dots$ is a nonzero integer. These spins that are not illuminated by the DMD pattern do not contribute to the measurement of a single shot of Ramsey spectroscopy. Instead, the spins that have been phase shifted by the light from the DMD pattern are measured, since they are rotated to a spin state with a non-zero $|1\rangle$ component. The amount of atoms measured depends on the acquired phase and the spatial intensity profile of the DMD pattern. Because this atomic profile is obtained with a single shot of Ramsey spectroscopy, it requires accuracy with setting the transverse phase evolution so that unperturbed phases have zero projection onto the $|1\rangle$ state. A FSK frequency of 2 kHz is used during the Ramsey time so that the spatially varying phase wrapping due to the differential mean-field and magnetic-field is negligible. This technique also requires a DMD light shift that is significant enough to shift the phases far enough to be observed, but not too far to wrap past π .

Figure 4.9 shows an example of a focused phase profile obtained from a single shot of Ramsey spectroscopy, where the most intense DMD light wraps the largest amount of phase. The DMD pattern was a narrow column of two mirrors, so that a small feature could be observed. The spatial width of the DMD pattern is fitted to a Gaussian for the full-width at half-max (FWHM) that quantifies the focus quality. Typical fitted FWHMs for our setup are around $25 \mu\text{m}$ at focus, about seven times larger than the diffraction limit of $\sim 4 \mu\text{m}$ (see Sec. 3.8.2 for optical setup). This measurement of a fitted FWHM is limited by atomic motion that occurs between the final $\pi/2$ -pulse and image collection, corresponding to about 1 ms for motion. Atomic

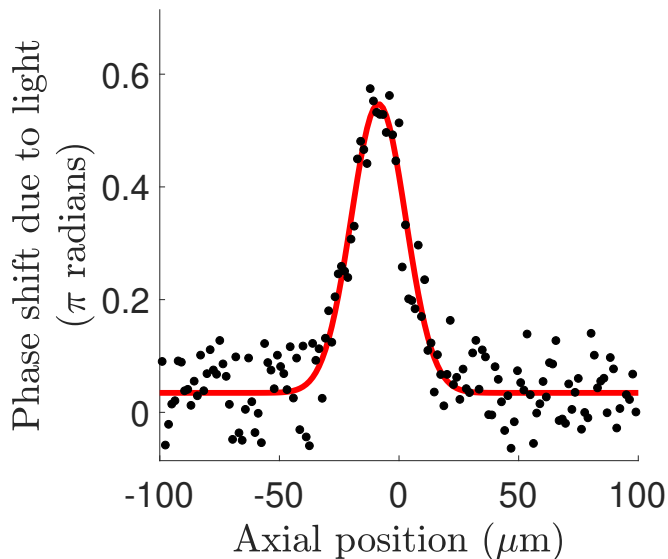


Figure 4.9: Ramsey snapshot mapping the DMD light intensity to the atomic density for focusing the DMD. The phase of the spins will shift when light is present, and the shifted transverse spins are measured. The light pattern used is a column of two DMD mirrors wide, and the Ramsey time is one period of the Ramsey or FSK frequency. The atomic profile is fitted with a Gaussian and the width of the Gaussian is the metric to minimize for best focus. The fitted FWHM is $26.7(7) \mu\text{m}$.

motion widens the measured FWHM so that the reported FWHM of $25 \mu\text{m}$ is an upper bound on the quality of focus of the DMD. A smaller FWHM could be measured by preparing a colder cloud of atoms that have a lower average velocity, or by shortening the time between the final $\pi/2$ -pulse and image collection.

The DMD alignment process has a total of three stages: coarse alignment to have some light on the atoms, centering the DMD pattern on atoms, and fine alignment with single Ramsey spectroscopy images. The coarse alignment of the DMD lens was accomplished by turning all DMD mirrors on and coarsely aligning the full intensity pattern to maximize atom loss during evaporation. The photon scattering rate is large enough to excite all of the atoms out of the magnetic trap during evaporation. The single shot Ramsey spectroscopy technique was used to center the DMD pattern on the atoms. This was done with a wide column of mirrors turned on and fine alignment of the pattern to center the pattern. The alignment steps discussed thus far have all been done with mirror alignment, and the imaging lens has not been touched. Now the imaging lens is moved to minimize the width of the Gaussian in the Ramsey snapshot. Depending on how far off the alignment is, the mirrors might need to be

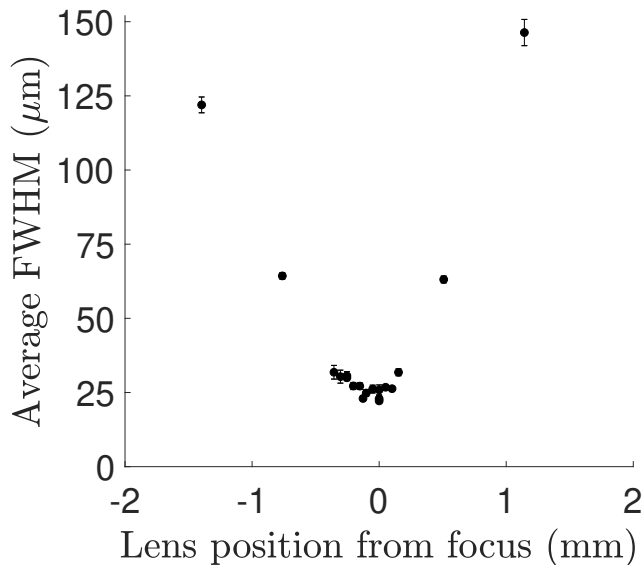


Figure 4.10: Focusing the DMD image onto the atoms by measuring single Ramsey spectroscopy images for various lens positions. The average fitted Gaussian full width at half max (FWHM) is extracted at each lens position over three shots. The minimum in FWHM is the optimal focus and the lens is placed there, giving a FWHM of $24(2) \mu\text{m}$. Error bars are fit uncertainties

realigned again if moving the imaging lens also translates the pattern at the atoms. Significant translation of the image implies the lens is tilted or the image is not centered on the lens. The DMD pattern is changed to a small strip of “on” mirrors with a width varying from 2 to 100 mirrors depending on how close the DMD lens is to being focused. The further away from focus, the more mirrors need to be on for a significant phase shift in one Ramsey period. The lens is translated on a translation stage until the FWHM is minimized. See Fig. 4.10 for an example of the fitted FWHM being minimized by adjusting the DMD imaging lens.

4.7 Magnification

The magnification of the imaging camera is required to correctly measure the spatial quantities of the atomic cloud since the magnification relates pixels to physical units. The magnification of the image is measured by observing a cloud fall due to gravity, which is the same for all objects in a vacuum. The atoms are initially in the state $|F = 1, m_F = -1\rangle$ and are transferred to the weakly trapped state $|F = 2, m_F = 0\rangle$ by using the ARP technique (Section 3.3.1). Since the $|F = 2, m_F = 0\rangle$ state is weakly

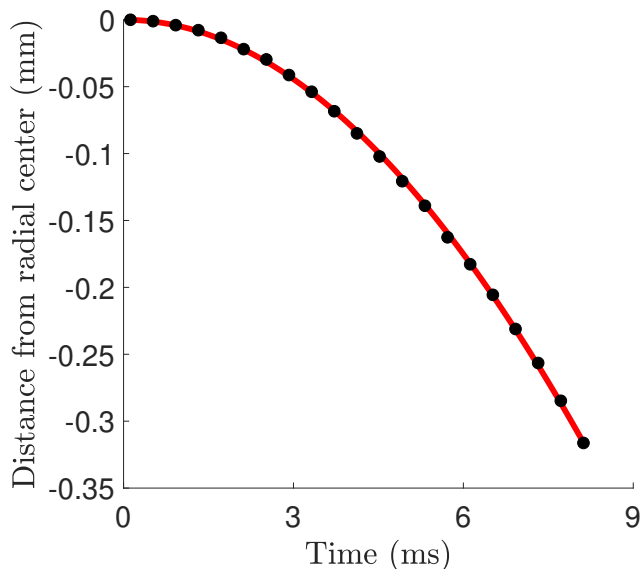


Figure 4.11: Atoms in the $|F = 2, m_F = 0\rangle$ state falling under the influence of gravity. The center of the cloud is plotted and fitted to $z(t) = \frac{1}{2}at^2 + z_0$ to calculate the magnification of the imaging camera using $M = g/a$. Here $M = 1.34(2) \mu\text{m}/\text{pixel}$, where errors are fit uncertainties.

magnetically trapped, the atoms will immediately fall under the influence of gravity. The short-time position of the atomic cloud at a time t after transferring to the state $|F = 2, m_F = 0\rangle$ can be modelled with kinematics, $z(t) = \frac{1}{2}at^2 + z_0$, where a is the acceleration in image units (pixels/s^2), and z_0 is the initial position in pixels. The magnification is $M = g/a$, where $g = 9.81 \mu\text{m}/\text{ms}^2$ is the acceleration due to gravity. Figure 4.11 shows the short time behaviour of the center of the cloud falling under gravity and is fitted for a to obtain a magnification of $1.38(6) \mu\text{m}/\text{pixel}$.

The atoms fall out of the view of the camera after about 10 ms, but since the $|F = 2, m_F = 0\rangle$ atoms are weakly trapped, the cloud will oscillate back at the weak trap frequency. The state $|F = 2, m_F = 0\rangle$ is affected by the quadratic Zeeman shift. This small shift is enough to weakly magnetically trap this state, but since gravity shifts the weak trap center the atoms will oscillate. The atoms travel 1.65 cm down and then return into the view of the camera about 80 ms later. Measurement of the atoms return provides a slightly better measurement of the image magnification. The center of mass motion of the cloud in this weak trap is [84]

$$z(t) = \frac{a}{c} \left(\cos(\sqrt{c}t) - 1 \right) + z_0, \quad (4.7)$$

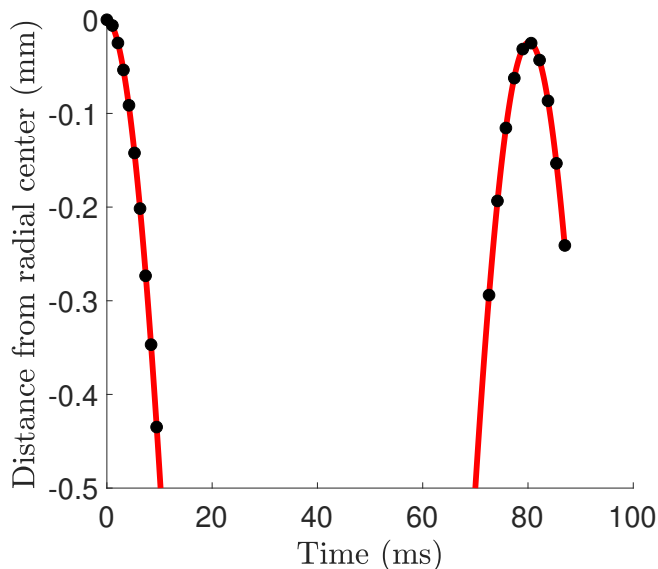


Figure 4.12: Atoms in the $|F = 2, m_F = 0\rangle$ state oscillating within a weak magnetic trap used to measure the magnification of the imaging camera. Fitting for the oscillation of the atomic cloud in Eqn. 4.7 improves the magnification measurement over just measuring the drop. However, if atoms explore the anharmonic region of the trap then this model breaks down. Here the magnification is found to be $M = 1.349(5)$ and the atoms fall 1.6 cm before returning back to the trap center.

where $c = \left(\frac{4\pi\hbar}{m}\right) fB'^2$ and $f = 287.57 \text{ Hz/G}^2$ is the quadratic Zeeman shift for rubidium-87. The magnetic field gradient B' is known from measuring the radial trap frequency and thus c is a known quantity. Figure 4.12 is an example of the atomic cloud center oscillating back into the field of view of the camera. This data is fitted for a and the magnification is $M = 1.349(5)\mu\text{m/pixel}$, an improvement over the short-time data. Measuring the magnification requires the camera to be focused first. The magnification of the imaging camera should be updated every time the camera optics are modified.

The magnification of the DMD can be measured with the same Ramsey snapshots as in Section 4.6, with two spatially separated columns of mirrors turned on. The distance between these mirror columns in the object plane is known from the DMD specifications, and the Ramsey snapshot provides the distance between these columns in the plane of the atomic cloud, the image plane. Magnification is then the usual $M = -d_{\text{image}}/d_{\text{object}} = -d_{\text{atom}}/d_{\text{DMD}}$. The magnification is measured to be about $\frac{1}{12}$. To measure the DMD magnification, the DMD and the camera must be focused and the camera magnification must be known.

4.8 Probe intensity

The probe intensity is used in Eqn. 3.6 to correct the measured OD for saturation effects when imaging the cloud. Each image measures the quantity I/I_{sat} and there must be a conversion factor to convert from pixel counts to intensity mW/cm^2 . Calibration of the probe intensity is the process of calculating this conversion factor I_{cal} . A photodiode with a 13 mm^2 active area is placed in the probe beam path about 5 cm in front of the science cell. The laser power on the photodiode is measured and the average intensity of the probe beam I_{probe} is calculated to be roughly $0.28 \text{ W}/\text{cm}^2$. Next, the camera takes two images, one with the probe light on and one without probe light, where the mean difference in pixel values is $\bar{I}_{\text{L-D}}$. The calibration parameter $I_{\text{cal}} = I_{\text{probe}}/I_{\text{L-D}}$ is calculated and used on every image afterwards to determine I/I_{sat} for OD correction. This calibration should be performed when the fiber coupling efficiency of the probe beam drifts or when imaging timings or laser power is changed.

4.9 Atomic cloud density

Calibration of the cloud density helps to limit the systematic errors in cloud number measurements, and is a great way to confirm that all other calibrations are working correctly. There are numerous ways that can lead to a decrease in cloud number or density, as shown in most of the previously discussed calibrations, but there are few errors that lead to an increase in measured number or density. Here a method to calculate a correction factor to estimate the systematic errors in density measurements is presented, where the correction factor will nearly always be one that increases the measured densities. The condensate fraction $N_{\text{BEC}}/N_{\text{total}}$ as a function of relative temperature T/T_c near degeneracy ($T/T_c = 0.5$ to 1.5) is used to check the density measurement. The transition from a thermal cloud to a BEC is easy to observe, and T_c depends on the number of atoms in the cloud. The condensate fraction for a trapped BEC with a correction for finite size is [96]

$$\frac{N_{\text{BEC}}}{N_{\text{total}}} = 1 - \left(\frac{T}{T_c}\right)^3 - \frac{3\bar{\omega}\zeta(2)}{2\omega_{\text{ho}}[\zeta(3)]^{2/3}} \left(\frac{T}{T_c}\right)^2 N^{-1/3}, \quad (4.8)$$

where $\bar{\omega}$ and ω_{ho} are the arithmetic and geometric means of the trap frequency, and ζ is the Riemann-Zeta function. The condensate fraction can be measured by processing the collected absorption images. The images can be processed in 2D or the radially

averaged 1D profiles can be processed, and both techniques should obtain the same result. These two processing methods are described in this section.

4.9.1 Density calibration with 2D images

Directly processing the images retains the most information about the cloud, but fitting large 2D images can be computationally slow. To help speed up computation time, the image is binned into 4×4 macropixels at the cost of spatial resolution. The cloud data are fitted for all three possible distributions: purely classical, purely degenerate, and finite temperature BEC. For a purely classical gas, the cloud is fitted to a 2D Gaussian

$$f_{\text{Gaussian}} = n_0^{2D} \exp\left(-\frac{z^2}{2z_0^2} - \frac{y^2}{2y_0^2}\right), \quad (4.9)$$

where z and y are the axial and radial coordinates, and the image is averaged over the third dimension x during collection. For a purely degenerate gas, the cloud is fitted to a 2D Thomas-Fermi (TF) distribution

$$f_{\text{TF}} = n_0^{2D} \left(1 - \left(\frac{z}{s_z}\right)^2 - \left(\frac{y}{s_y}\right)^2\right)^{3/2}. \quad (4.10)$$

For a finite temperature BEC, the BEC portion of the cloud follows a Thomas-Fermi distribution, but the thermal component cloud is modified by Bose statistics and is a 2D Boseian distribution

$$f_{\text{Boseian}} = n_0^{2D} g_2 \left(\exp\left(-\frac{z^2}{2z_0^2} - \frac{y^2}{2y_0^2}\right) \right). \quad (4.11)$$

The geometric function $g_\gamma(x) = \sum_{n=1}^{\infty} \frac{x^n}{n^\gamma}$ shows up in the statistics of Bose gases because of a series expansion for small fugacity (see Refs. [123, 96, 124] for details). This function reduces to the Riemann-Zeta function ζ if the argument is one, i.e. $g_\gamma(x=1) = \zeta(\gamma)$. Measuring the condensate fraction is only possible if the cloud has both a thermal and condensate fraction, so the Boseian and Thomas-Fermi distributions are fitted at the same time. Since the BEC and thermal cloud exist in the same trap, their centers are identical. The peak densities in the 2D distributions n_0^{2D} relate

to the 3D peak densities n_0 with

$$n_0^{2D} = \begin{cases} \sqrt{2\pi}x_0n_0 & \text{Gaussian} \\ \sqrt{2\pi}x_0n_0\frac{\zeta(2)}{\zeta(3/2)} & \text{Boseian} \\ \frac{4}{3}s_xn_0 & \text{Thomas-Fermi.} \end{cases}$$

The 3D peak density is calculated from the fit parameters: z_0 , y_0 , n_0 , and centers. The trap geometry of our apparatus sets the two radial sizes to be equal ($x_0 = y_0$ and $s_x = s_y$).

An example of density calibrations using 2D images is shown in Fig. 4.13, where the thermal component is colored red, and the condensate component is blue. The temperature is computed from the fitted axial width of the thermal cloud with $k_B T = m\omega_z^2 z_0^2$, and using the correction for the expansion time (see Eqn. 3.8). The total number of atoms in the thermal cloud and the condensate are

$$N_{\text{Gaussian}} = n_0^{2D}(2\pi)y_0z_0 \quad (4.12)$$

$$N_{\text{Boseian}} = n_0^{2D}(2\pi)y_0z_0\frac{\zeta(3)}{\zeta(2)}, \quad (4.13)$$

$$N_{\text{BEC}} = n_0^{2D}s_y s_z \frac{2\pi}{5}, \quad (4.14)$$

where $N_{\text{total}} = N_{\text{BEC}} + N_{\text{Thermal}}$. After performing fits to all three possible distributions, the fitted distribution with the lowest residuals decides the classification of the cloud. Sometimes the residuals do not get the cloud classification right, so the classification is selected manually based on visual inspection of the image. The condensate fraction is then calculated for each cloud, where for pure condensates and pure thermal clouds the condensate fraction is 1 and 0, respectively. The slow fitting time, loss of spatial resolution from binning, and higher difficulty in separating between the three cloud classifications makes it difficult to quickly perform a density calibration with this processing method.

4.9.2 Density calibration with 1D density profiles

Measuring the condensate fraction requires three numbers to be accurately measured and compared to theory: the temperature T , number of atoms in the thermal cloud N_{thermal} , and number of atoms in the condensate N_{BEC} . The critical temperature T_c is calculated from the total number of atoms in the cloud. The computationally quickest

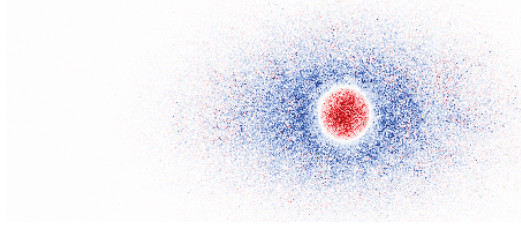


Figure 4.13: False-colored image as an example of locating the BEC (red) and thermal cloud (blue) components from a 2D image of a cloud. The white circle between the BEC and thermal cloud is where an equal amount of each component exists, which is different than the white surrounding the thermal cloud where there is a negligible number of atoms. The identification of BEC and thermal clouds can be used to calibrate the density of the system by comparing to the expected condensate fraction.

method to compute these numbers is with 1D axial density profiles that come from averaging over the other radial direction y in the absorption image. Computation time for the three fits is significantly faster in 1D and does not require spatial binning.

Examples of these 1D profiles with their corresponding fits are shown in Fig. 4.14, where the cloud classification is based on the lowest fitted residuals with occasional correction based on visually inspecting the 2D image. The 1D density distributions are obtained by integrating Eqns.4.9, 4.10, and 4.11 over the y direction to obtain

$$f_{\text{Gaussian}} = n_0^{1\text{D}} \exp\left(-\frac{z^2}{2z_0^2}\right) \quad (4.15)$$

$$f_{\text{Boseian}} = n_0^{1\text{D}} g_{5/2}\left(\exp\left(-\frac{z^2}{2z_0^2}\right)\right) \quad (4.16)$$

$$f_{\text{TF}} = n_0^{1\text{D}} \left(1 - \frac{z^2}{s_z^2}\right)^2. \quad (4.17)$$

The number of atoms in each component is obtained by integration over z

$$N_{\text{Gaussian}} = n_0^{1\text{D}} \sqrt{2\pi} z_0 \quad (4.18)$$

$$N_{\text{Boseian}} = n_0^{1\text{D}} \sqrt{2\pi} z_0 \frac{\zeta(3)}{\zeta(5/2)} \quad (4.19)$$

$$N_{\text{TF}} = n_0^{1\text{D}} s_z \frac{16}{15}. \quad (4.20)$$

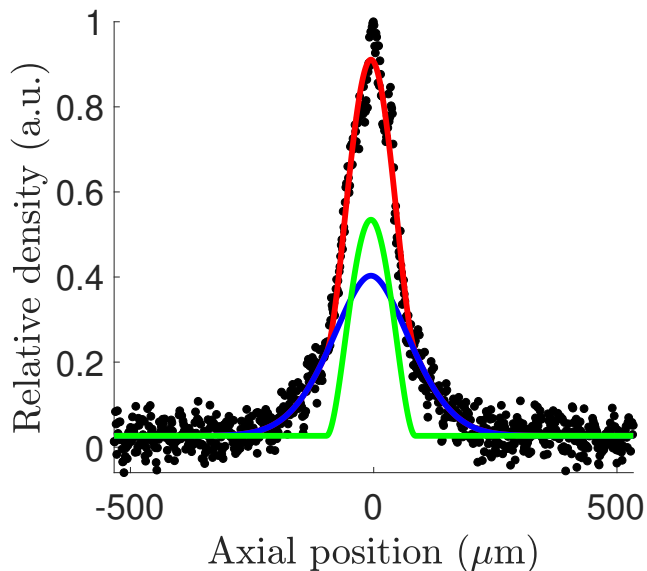


Figure 4.14: Example of a fit to a 1D Boseian-TF profile used for density calibrations. The Boseian (blue) and Thomas-Fermi (green) contributions are fitted simultaneously to obtain the combined distribution (red). The relative number of atoms in each component and the temperature of the gas are extracted from the fits. In this example, $T/T_c = 0.76$ and $N_{\text{BEC}}/N_{\text{total}} = 0.39$. The density at the center of the BEC typically does not fit well because the density is highest there and the saturation OD correction factor is large (see Eqn. 3.4).

Lastly, the 1D peak density is related to the 3D peak density by

$$n_0^{1\text{D}} = \begin{cases} 2\pi x_0 y_0 n_0 & \text{Gaussian} \\ 2\pi x_0 y_0 \frac{\zeta(5/2)}{\zeta(3/2)} n_0 & \text{Boseian} \\ \frac{\pi}{2} s_x s_y n_0 & \text{Thomas-Fermi.} \end{cases}$$

The temperature and number of atoms in the cloud are varied and the condensate fraction is computed for each point as illustrated in Fig. 4.15. The condensate fraction is fitted to Eqn. 4.8 and a density correction factor A is calculated. This density correction factor is an estimate of the systematic errors in measuring cloud densities or total number. The actual atom number is modified by $N_{\text{actual}} = AN_{\text{measured}}$, where the correction factor A alters the value of T_c and N appearing on the right side of Eqn. 4.8. The correction factor is estimated to $A = 1.09(2)$, meaning that the reported densities could be around 10% too low. A more accurate correction factor could be obtained by averaging over more points, but density shifts of 10% do not drastically change the behaviour of spin diffusion.

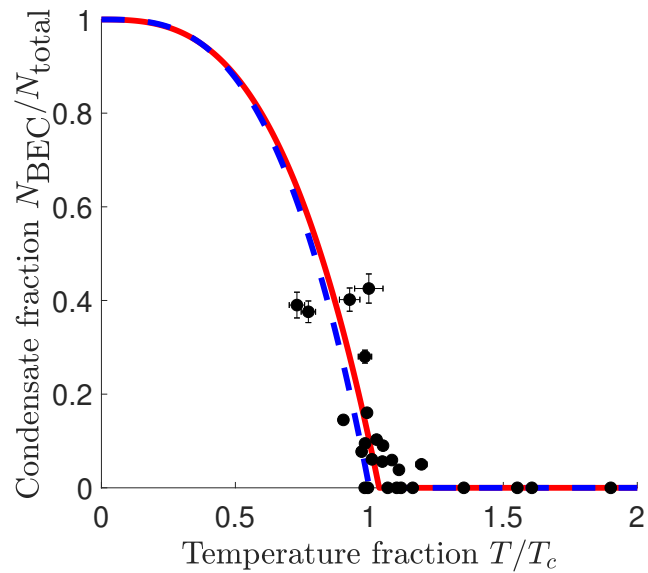


Figure 4.15: Density calibration using radially-averaged density profiles to measure the condensate and temperature fractions of a cloud near the critical temperature. The dashed blue line is the prediction of Eqn. 4.8 without the finite size term and agrees well with the data. The solid red line represents a fit of Eqn. 4.8 to the data and allowing for a number correction $N \rightarrow AN$. The fitted number correction $A = 1.09(2)$ hints that all reported number measurements could be systematically low by about 10%.

4.10 Optimizing the initial spin profile

The initial spin profile is prepared by detuning one half of the cloud during a cloud-wide π -pulse as discussed in Section 3.2. The applied detuning can alter the Rabi frequency significantly on the detuned half of the cloud (see Section 2.1.3). During the cloud-wide π -pulse, the spin vector of the detuned half of the cloud rotates around the effective Rabi vector. Since the applied detuning increases the effective Rabi frequency by ten times or more, the spin vector will typically wrap ten times around the Bloch sphere or more during a resonant π -pulse.

An example of this wrapping in the Bloch sphere is shown in Figure 4.16(a), where the colored line represents the final Bloch vectors across the cloud. The red shading of the line represents the Bloch vector of the detuned half, and the blue shading signifies the zero-detuned half. These colors are interpolated between domains to produce a purple shading corresponding to the domain wall. The multiple wrappings of the spin vector are purely due to the large applied detuning of order $38\Omega_R$. This wrapping in the Bloch sphere shows up as a spatially varying spin density in Fig. 4.16(c), where there are longitudinal spin modulations in the $|1\rangle$ domain since transverse spin exists when $M_z \neq \pm 1$.

This large detuning for initial preparation is used for the results presented in this thesis (Chapters 5 and 6). These spatial modulations of the spin profile do not significantly modify spin diffusion, because the modulations will quickly diffuse and smooth out the domain wall. However, the significant wrapping of the transverse phase leads to an initial dephasing once motion occurs and scrambles phases. This dephasing process is similar to the forced dephasing described in Section 5.1, except here the dephasing comes from the initial preparation and limits the peak transverse amplitude.

The detuning used in preparation is optimized by performing optical Bloch simulations (Section 2.1.1) to locate the optimal detuning, and then experimentally locating that detuning. The simulations reveal that a detuning of $\Delta = \sqrt{3}\Omega_R$ reduces the amount of Bloch sphere wrapping during preparation. The effective Rabi frequency of the detuned half of the cloud is then $2\Omega_R$, so the timing of the resonant π -pulse corresponds to a 2π -pulse on the detuned half of the cloud. This 2π -pulse rotates around a Rabi vector that is tilted down 60° from the x-y plane of the Bloch sphere. The rotation about this Rabi vector does not oscillate entirely through the $|2\rangle$ state. However, the spin vector does rotate exactly once around the effective Rabi vector and ends up in the same initial state. The final optimized spin state across the cloud

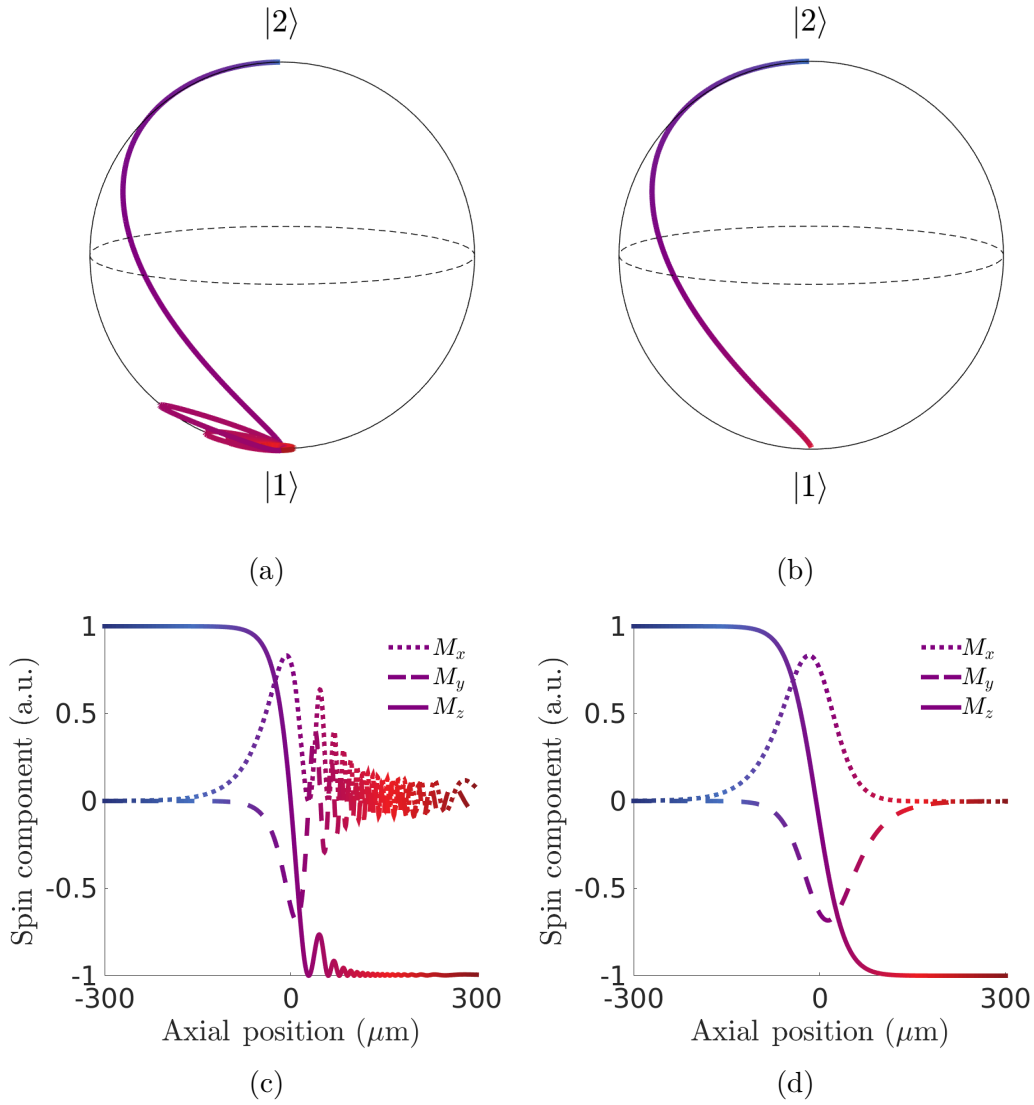


Figure 4.16: Optical Bloch simulations showing the spatial variation of the spin components after initial state preparation with a hyperbolic tangent detuning profile. The detuning Δ peaks at (a,c) $38\Omega_R$ and (b,d) $\sqrt{3}\Omega_R$, where the spin vector wraps around the Bloch sphere significantly more at larger peak detunings. (a,b) Spatial variation of the initial spin state in the Bloch sphere, where blue (red) corresponds to the left (right) side of the cloud. (c,d) The individual spin components are shown, with shading that corresponds to varying axial position. The shading is identical to what was used for the spin states in the Bloch sphere. Minimal initial dephasing is obtained when $\Delta = \sqrt{3}\Omega_R$.

is shown in the Bloch sphere in Fig. 4.16(b), where a minimal amount of wrapping is present.

The spatial variation of the spin components using these two detunings during spin preparation is shown in Fig. 4.16(c) for $\Delta = 38\Omega_R$ and Fig. 4.16(d) for $\Delta = \sqrt{3}\Omega_R$. The optimized detuning of $\sqrt{3}\Omega_R$ generates a smoothly varying spin profile. The additional spin wrapping with the larger detuning of $38\Omega_R$ disrupts the smooth spin profile, and the spin components oscillate within the $|1\rangle$ domain. While the magnitude of the longitudinal spin oscillations are relatively small, the transverse spin oscillations are significant. The tightly wrapped transverse spin is effectively a dephasing, where spin preparation with large detuning can reduce the initial coherence by up to 20%.

The optimal detuning is experimentally located by varying the applied detuning with the power of the laser that provides the detuning. Each domain wall is fitted for domain balance parameter ϵ using

$$f_{\text{spin profile}} = A \tanh\left(-\frac{(z - z_c)}{\lambda}\right) \left(1 - \epsilon \mathcal{H}(z - z_c)\right) n(z), \quad (4.21)$$

where A is the domain amplitude, z_c is the domain center, λ is the domain width, $\mathcal{H}(z)$ is the Heaviside step function, and $n(z)$ is the atomic density. The domain balance ϵ modifies the domain amplitude on one side of the cloud, where $\epsilon = 1$ corresponds to an equal balance between the spin domain amplitudes. The domain balance modifies the amplitude of the right ($|1\rangle$) domain by the factor ϵ since the extra spin vector wrapping occurs within that domain (see Fig. 4.16). In the limiting case of when the detuning approaches zero, the entire cloud is transferred to $|2\rangle$ during preparation and ϵ approaches zero.

Figure 4.17 shows the fitted domain balance as a function of applied detuning. The first peak corresponds to the optimal detuning of $\sqrt{3}\Omega_R$ and secondary peaks correspond to the next integer multiples of the effective Rabi frequency, i.e. $\Delta = \sqrt{8}\Omega_R$, $\sqrt{15}\Omega_R$, etc. The optical Bloch simulations in Fig. 4.17 show good agreement with the fitted domain balance. At large detunings, the fits to experimental data benefit from atomic motion smoothing out the domains. This smoothing causes the spin wrapping to be averaged and the spin profile is still well fitted with Eqn. 4.21. In simulations, the spin profile fits break down at high detunings where the multiple wrappings around the Bloch sphere modify the spin profile significantly from Eqn. 4.21. Since the simulation does not include motion of atoms in the cloud, the spin profile is better represented by Fig. 4.16(c) than (d). At these large detunings, the simulation is not

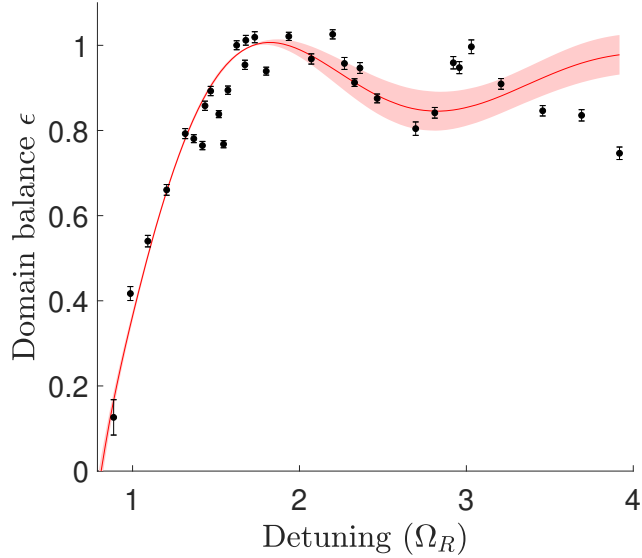


Figure 4.17: Optimizing initial spin preparation detuning by fitting for the spin domain balance of longitudinal spin profiles (see text). The domain balance is plotted with fit uncertainties for error bars. The first peak corresponds to a detuning of $\sqrt{3}\Omega_R$, which is the optimal detuning. Optical Bloch simulations of the spin preparation are used to generate a simulated spin domain that is fitted to Eqn. 4.21 for domain efficiency ϵ in red. The shaded region is the 3σ confidence band showing that the fits break down past the optimal detuning of $\sqrt{3}\Omega_R$.

well fitted by Eqn. 4.21. This is shown by the increasing 3σ confidence bands on the fitted domain balance at large detunings.

The optimal detuning corresponds to the peak in domain balance at the lowest detuning. This peak corresponds to a detuning of $\Delta = \sqrt{3}\Omega_R$ and maximizes the initial coherence in the domain wall. This calibration not only identifies the optimal detuning, but also confirms the tunability of the laser power used with DMD patterns. This calibration should be performed whenever the laser power drifts or if the initial spin domain drifts.

This chapter covered the most relevant calibration methods used to optimize the spin profile and to ensure smooth operation of the apparatus. The results shown in the next two chapters made use of these calibrations to ensure the reported densities, temperatures, and spin components are accurate.

Chapter 5

Diffusion of a dipolar spin profile

This chapter is adapted from the article “Longitudinal spin diffusion in a nondegenerate trapped ^{87}Rb gas” published in Physical Review Letters [125], in which longitudinal and transverse spin diffusion were observed for the helical spin domain discussed in Section 3.2. The dynamics of the spin profile were investigated for different initial coherences in the domain wall. We found that coherence in the domain wall leads to transverse-spin-mediated longitudinal spin diffusion that is slower than expected based on classical predictions. Spin diffusion of a sharp longitudinal spin gradient showed an instability in the longitudinal spin dynamics because the longitudinal and transverse spin components couple. A conversion of longitudinal spin to transverse spin was observed, resulting in an increase of the total amount of coherence in the system.

5.1 Spin diffusion with high initial coherence

The initial spin domain structure was prepared using the procedure stated in Section 3.2. This two-domain spin profile has transverse spin between the domains, and the amount of coherence in this domain wall can be reduced by rapid dephasing. This rapid dephasing was performed by applying a sharp differential potential that spatially varies the Larmor precession of the transverse spin phases. From one side of the domain wall to the other, the transverse phases can be wrapped by 50π in 0.4 ms. This large amount of phase wrapping could be undone with a quick spin-echo procedure, but any motion of spins will effectively scramble the phases. This scrambling of phases is decoherence and lowers the overall coherence in the domain wall.

The transverse spin coherence is calculated with $c = M_{\perp}/M_{\perp}^{\text{max}}$, where M_{\perp} is the measured transverse spin amplitude and M_{\perp}^{max} is the maximum possible transverse

spin. This initial coherence varies from 0 for no coherence to 1 for maximum coherence. A max coherence of $c = 1$ corresponds to locally all of the individual transverse spins having the same phase, and no coherence ($c = 0$) corresponds to transverse spins with random phases or zero transverse spin. The coherence across the cloud is measured by combining the individually measured spin components just as in Section 3.6. The maximum amount of transverse spin is given by $M_{\perp}^{\max} = 2\sqrt{N_1 N_2}$, where $N_1 = |\langle m|1\rangle|^2$ and $N_2 = |\langle m|2\rangle|^2$ are the modulus square of the projections of the spin density distribution state ($|m\rangle$) onto the longitudinal spin states ($|1\rangle$ and $|2\rangle$). The transverse spin M_{\perp} is measured with Ramsey spectroscopy and the coherence is obtained by the ratio $M_{\perp}/M_{\perp}^{\max}$. Figure 5.1 shows an example of the coherence across the cloud for the helical spin domain. The coherence is peaked in the center of the domain wall where only transverse spin exists. This peak corresponds to the initial coherence c_{init} , which is $c_{\text{init}} \approx 0.55(5)$ in this example. Further from the center of the cloud the coherence decreases since the relative transverse spin amplitude is lower where longitudinal spin exists. This peak coherence can be reduced through rapid dephasing, which is discussed in Section 5.2.

First, spin diffusion for the maximum obtainable initial coherence of $c_{\text{init}} = 0.74$ is explored. The temporal evolution of the normalized longitudinal spin for $c_{\text{init}} = 0.74$ is shown in Fig. 5.2, in which multiple images of state $|1\rangle$ and state $|2\rangle$ distributions are temporally stitched together to track spin evolution (see Section 3.5). The helical domain was initially prepared with $|2\rangle$ on the left and $|1\rangle$ on the right of the cloud, and after 250 ms the spin domain structure flips while continuing to decay slowly. The atoms oscillate in the trap at the trapping frequency ($\omega_z = 2\pi \cdot 6.71$ Hz), so a complete spin oscillation should occur in 150 ms in the collisionless limit. Instead the observed spin-domain oscillation time is about three times slower than the trapping frequency. Considering only elastic collisions, classical diffusion predicts that diffusion should occur on the timescale of $z_0^2/D_z \sim 25$ ms. Here the longitudinal spin diffusion constant is $D_z = \frac{1}{3}\ell v_T$, with mean free path $\ell = (\sqrt{2}n4\pi a^2)^{-1}$ and mean thermal velocity $v_T = \sqrt{16k_B T/(3\pi m)}$. This classical prediction is ten times faster than the observed spin diffusion timescale, and highlights that spin diffusion can be significantly different than classical diffusion.

The observed slowing of spin diffusion when compared to classical diffusion is due to the identical spin rotation effect (ISRE), as discussed in Section 2.2. The slowed diffusion is primarily caused by the presence of transverse spin, because the ISRE can only modify spin diffusion if transverse spin is present. The ISRE rotates spins about

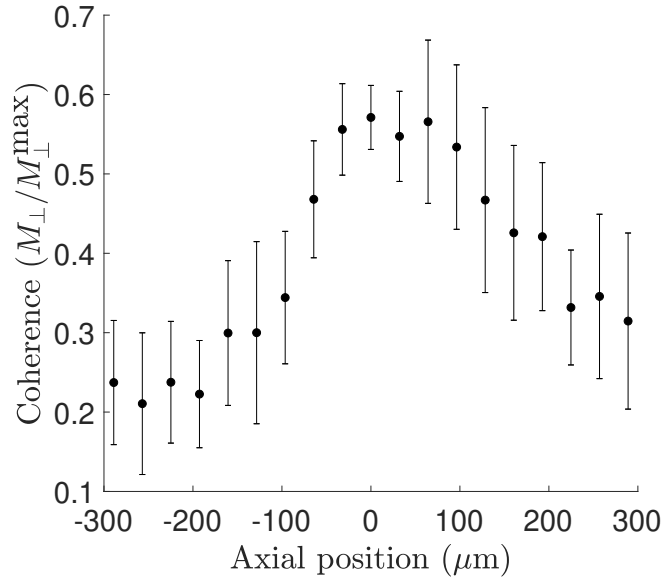


Figure 5.1: The coherence is calculated with $c = M_{\perp}/M_{\perp}^{\text{max}}$ across the helical spin profile prepared with a medium detuning of $\Delta = 9\Omega_R$ (see Sections 3.6 and 4.10). The transverse amplitude M_{\perp} was measured with Ramsey spectroscopy and the maximum transverse spin is given by $M_{\perp}^{\text{max}} = 2\sqrt{N_1 N_2}$. The coherence peaks at the center of the domain wall, between the two spin domains. In this example, the initial coherence corresponds to the peak coherence of $c_{\text{init}} \approx 0.55(5)$. The error bars are a combination of the fit uncertainty and the statistical noise for each axial bin.

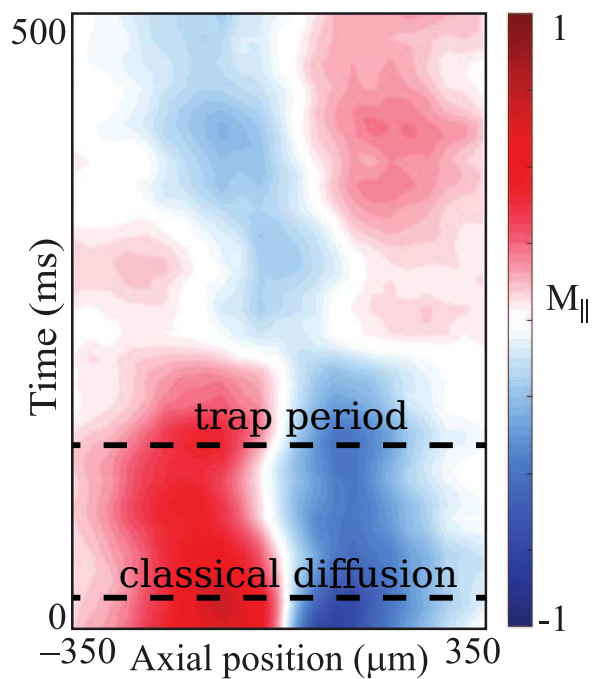


Figure 5.2: The evolution of spin diffusion with initial coherence of $c_{\text{init}} = 0.74$. Spin states $|2\rangle$ (red) and $|1\rangle$ (blue) are initially prepared in a dipolar domain and after about 250 ms the domains oscillate. The timescale for this oscillation is much longer than classical diffusion predicts, $z_0^2/D_z \sim 25$ ms, and the trap frequency that atoms oscillate at is $\tau \sim 150$ ms. The temperature of the cloud is $T = 650$ nK ($T/T_c \sim 1.5$) and the peak density is $n_0 = 2.6 \times 10^{13} \text{ cm}^{-3}$.

the mean spin, partially converting the spin of an atom moving between domains, so that spin $|2\rangle$ atoms are rotated to spin $|1\rangle$ and vice versa. The spins that travel between domains are rotated about the helical local spin, where frequent collisions allow the moving spin to follow the local spin. For many collisions through the domain wall, this spin following is identical to an adiabatic following, where the travelling spin never deviates far from the local spin. However, the density of the cloud used here is between the collisionless and adiabatic following regimes, and so spins that travel through the domain wall are partially rotated as they enter the other spin domain. This partial transfer of spins from one longitudinal state to the other through the ISRE is the primary effect that slows spin diffusion relative to classical diffusion.

The temporal evolution of transverse spin for $c_{\text{init}} = 0.74$ initial coherence is displayed in Fig. 5.3. The transverse phase profile is largely static during diffusion because the longitudinal spin gradient sets up the phase profile. However, the transverse spin amplitude spreads out from the center of the domain wall and decoheres until nearly zero transverse amplitude is detected. The Ramsey fringes used to generate the transverse amplitude and phases at the center of the cloud and at slightly off-center are in Fig. 5.3(c) and (d) and show a clear distinction of the short-time behaviour at these two axial positions. These figures show the transverse spin amplitude in the center of the cloud is roughly constant over 100 ms, while the off-center position sees a steady increase in transverse amplitude over the 100 ms. On first glance, this looks like a typical diffusion process where the high concentration of transverse spin in the center diffuses to the edge of the cloud. However, the transverse spin amplitude does not decrease in the center, so the total transverse spin amplitude across the cloud is increasing. The effect of this initially nondecaying transverse spin in the center of the cloud is discussed in Section 5.3.

The spin diffusion of the initial dipolar spin profile at the cancellation spot was shown to be different than classical diffusion. To summarize, the longitudinal spin oscillates and decays at a timescale that is slower than classical diffusion timescales. Meanwhile, the transverse spin spreads out and dephases, but the amplitude of the transverse spin in the center of the cloud remains constant. Because these experiments are performed at the cancellation spot, the only modification to spin diffusion was the ISRE, where indistinguishable spins collide and rotate about their combined spin. The ISRE is shown here to cause a significant slowing effect on the diffusion of the helical spin domain.

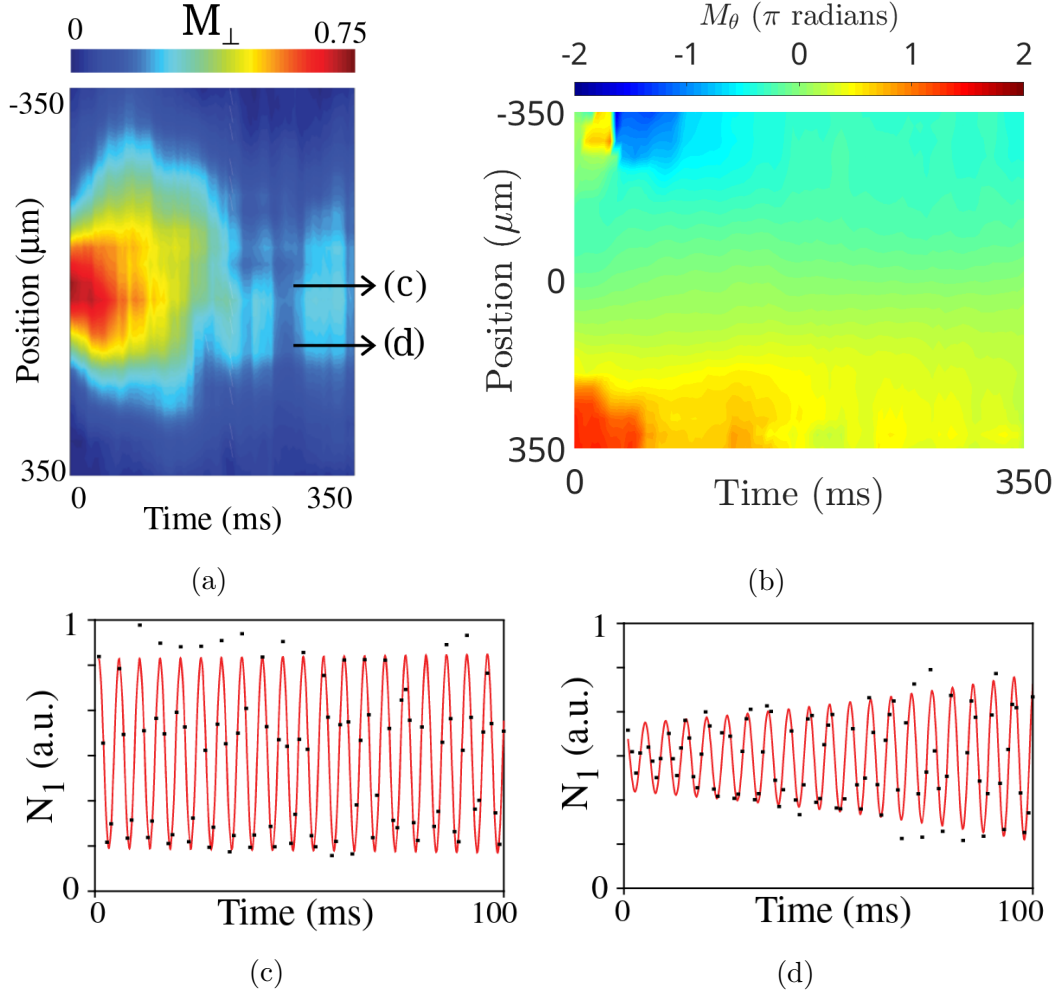


Figure 5.3: Transverse spin diffusion of the dipolar spin profile with an initial coherence of $c_{\text{init}} = 0.74$. (a) The transverse amplitude M_{\perp} showing diffusion of transverse spin from the center of the cloud. (b) The transverse phase M_{θ} is static during diffusion, with the exception at the beginning when the initialized phase profile quickly changes to the static phase profile. Examining the Ramsey fringes at (c) the cloud center $z = 0$ and (d) off-center at $z = 0.3z_0$ shows that the transverse spin is roughly constant in the center and increases away from the center. The red curve is meant as a guide for the eye and a moving window would be fitted to these fringes.

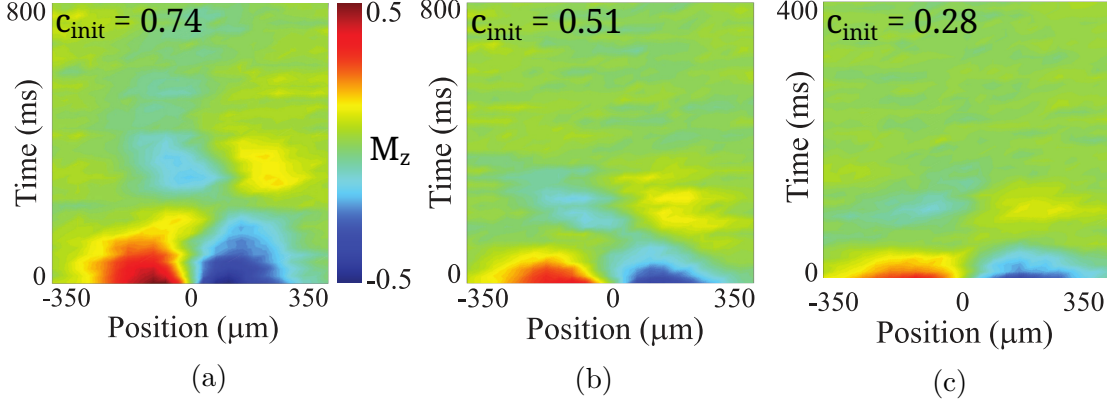


Figure 5.4: Longitudinal spin diffusion for initial coherences of (a) $c_{\text{init}} = 0.74$, (b) $c_{\text{init}} = 0.51$, (c) $c_{\text{init}} = 0.28$. The longitudinal spin domains oscillate and damp faster as the initial coherence is reduced. The initial coherence in the domain wall plays a significant role in modifying spin diffusion since the longitudinal spin diffusion in case (a) is about 3 times slower than in case (c).

5.2 The effect of coherence on longitudinal spin diffusion

The longitudinal spin diffusion for initial coherences of $c_{\text{init}} = 0.74, 0.51$, and 0.28 is shown in Fig. 5.4. At low initial coherences the spin diffusion timescale is decreased since the oscillation of the spin domains is faster. At large initial coherences the collisions between spins preserve the domains longer since the moving spins adiabatically follow the local spin when they cross domains. The reduction of initial coherence in the domain wall limits the effectiveness of the ISRE interactions since the local transverse phases are randomized, and spins cannot adiabatically follow the local spin. The ISRE's contribution to spin diffusion is removed when the coherence approaches zero, leading to spin diffusion times that approach classical diffusion times.

Spin diffusion of this helical domain is dominated by the dipole mode, so diffusion timescales can be quantified by examining the dipole moment of the spin density $\langle zM_z \rangle$. The time-varying dipole moment is shown in Fig. 5.5 for the same three initial coherences. The difference in diffusion timescales is evident as the lowest coherence case has oscillated and damped before the highest coherence has had a single oscillation. These dipole moments are fitted to a damped sine $\exp(-\Gamma t) \sin(2\pi f t)$ for the longitudinal spin damping rate Γ , and the domain oscillation frequency f .

The damping rate and oscillation frequency for various initial coherences are shown in Fig. 5.6. At high initial coherences both the damping rate and oscillation frequency

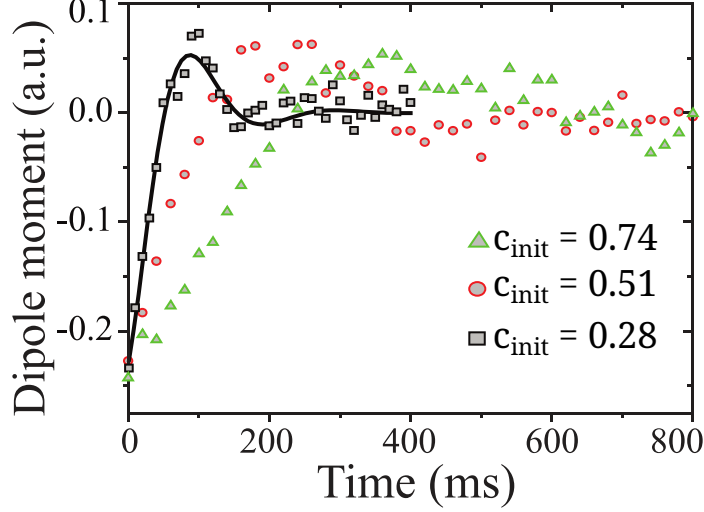


Figure 5.5: The dipole moments $\langle zM_z \rangle$ for three initial coherences that summarizes the longitudinal spin diffusion in Fig. 5.4. Spin diffusion is slowed at high coherences and sped up at low coherences. The line is a fit to a damped sine for the $c_{\text{init}} = 0.28$ case, where an oscillation frequency and damping rate can be extracted from the fit.

decrease. Here the ISRE interactions lead to spins being mostly rotated from one longitudinal spin to the other as they cross the domain wall. At low initial coherences the damping rate and oscillation frequency are increased because the ISRE is reduced. The damping and oscillation rates are limited by the classical diffusion damping rate $\Gamma_{\text{classical}} = \tau_{\text{elastic}}^{-1} = 40$ Hz and trap oscillation $f_{\text{classical}} = \omega_z/2\pi = 6.71$ Hz, where ω_z is the trapping frequency and τ_{elastic} is the elastic collision rate between atoms.

The dipole moment fits are compared with spin diffusion theory through numerical simulations (Sections 2.3 and 2.4). The shaded regions in Figs. 5.6(a) and (b) represent 1σ confidence bands from Monte Carlo simulations of the 1D quantum Boltzmann equation Eqn. 2.46, including statistical fluctuations in temperature, density, and domain wall size, as well as a systematic density calibration uncertainty. The data agree well with the theoretical predictions. Discrepancies in the oscillation frequency f at low coherence are likely due to challenges in fitting critically damped oscillations, where the quality factor drops. Overdamping should occur for $c_{\text{init}} < 0.2$, but these small coherences are hard to measure accurately and reducing the coherence to this level without altering the longitudinal spin domains is challenging.

The initial coherence plays a critical role in modifying spin diffusion. Coherence is required between spin domains for spin diffusion to deviate from nonclassical behaviour. Through analysis of the dipole moment, spin diffusion times were shown to be between 4 – 10 times slower due to the ISRE converting spins as they travel

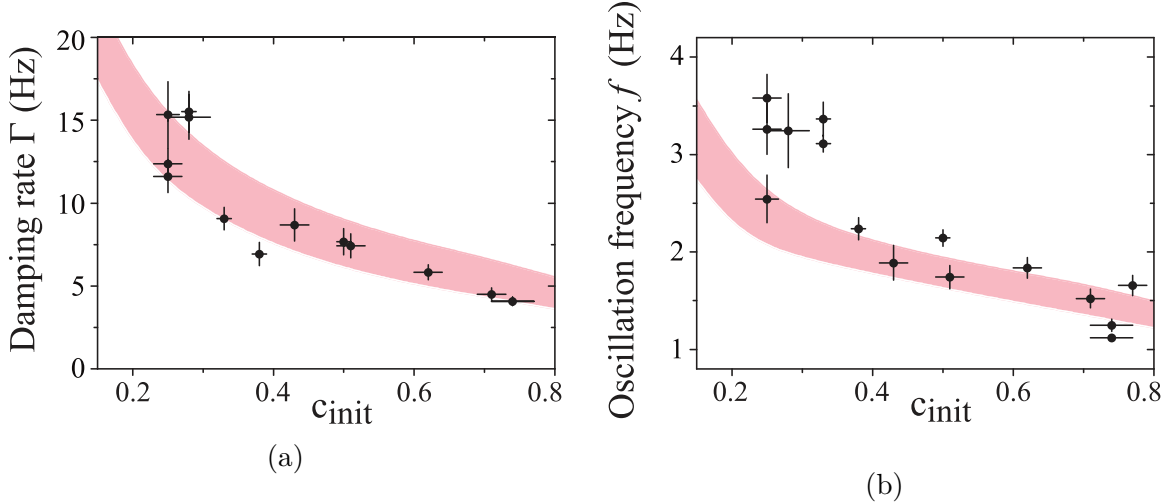


Figure 5.6: The (a) damping rate and (b) oscillation frequency are found through fits of the dipole moments to a damped sine. Error bars correspond to fit uncertainties of the dipole moment oscillation and the initial coherence c_{init} measurement. The shaded band is the result of numerical simulations of Eqn. 2.46.

through the coherent domain wall. This slowing is the main effect of coherence on spin diffusion, but while exploring diffusion of the helical spin domain, a spin instability was observed and is discussed in the next section.

5.3 A spin instability

The effect of coherence on transverse spin diffusion is shown in Fig. 5.7. The transverse amplitude is shown for approximately the same initial coherences as the longitudinal diffusion examples displayed in Fig. 5.4. In all three cases the transverse spin quickly spreads from the domain wall and then decays around 100 – 200 ms later, with the largest initial coherence corresponding to the longest-lived transverse spin. For the highest initial coherence, the transverse amplitude at three different axial positions along the cloud is shown in Fig. 5.7(b). These transverse amplitudes are obtained via fits to a moving window that is described in Section 3.5.2. The transverse amplitude at all three axial positions initially increases with time. However, for purely classical diffusion, a decrease in the transverse amplitude at the center of the cloud is expected as transverse spin diffuses to the edges of the cloud. This increase hints that the total transverse spin amplitude in the cloud is increasing.

Figure 5.8 shows the total transverse spin amplitude $\sum_i M_{\perp}(z_i)$ for the three initial coherences. In all three cases, the total transverse spin amplitude, or ensemble

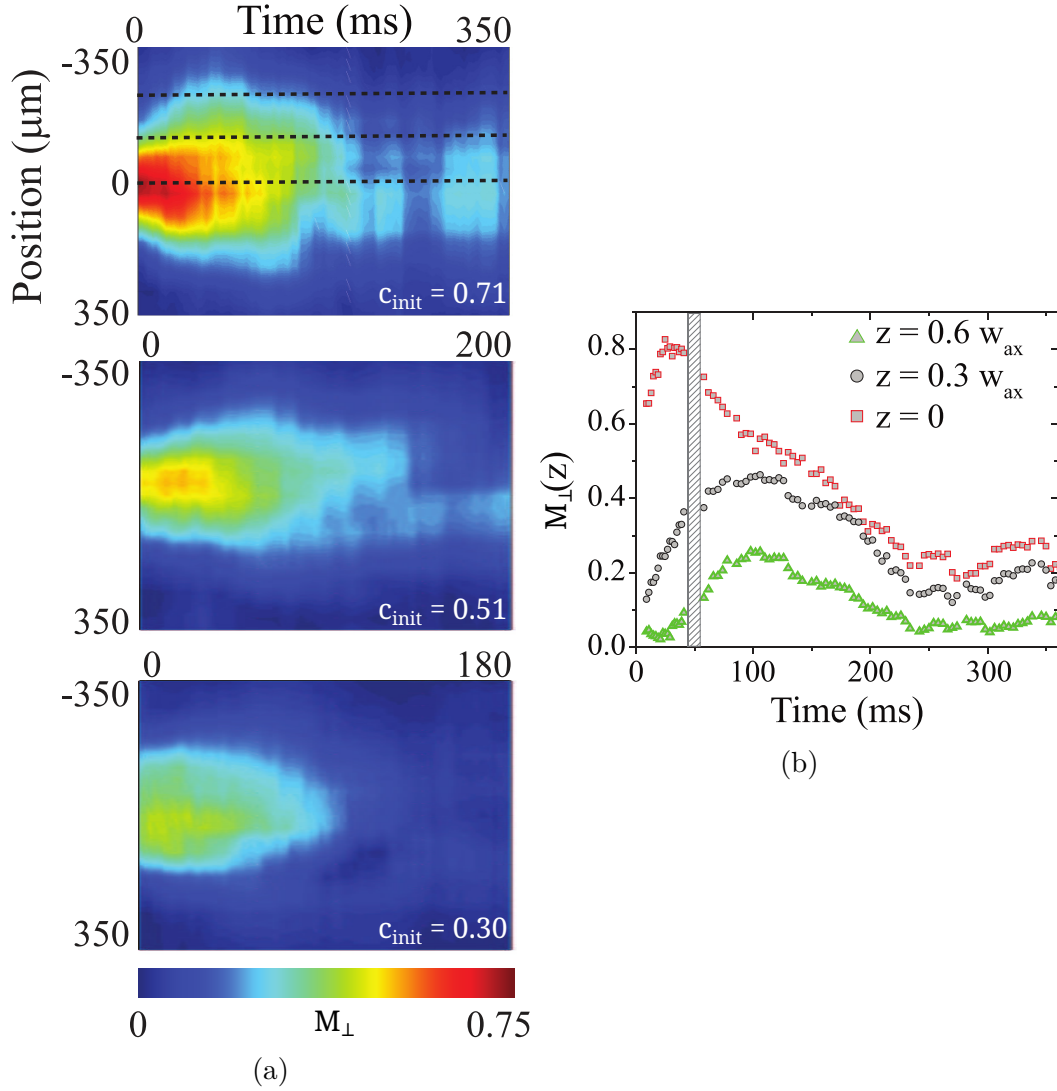


Figure 5.7: (a) Time evolution of the transverse spin M_{\perp} for different initial domain wall coherences $c_{\text{init}} = 0.71, 0.51, 0.30$ in the cloud center. (b) Time evolution of the transverse amplitude M_{\perp} in different spatial regions, denoted by $z = (0, 0.3, 0.6) \times z_0$ and corresponding to the dashed lines in (a). The hatched box indicates a change in sampling rate to measure both the fast initial rise of coherence and the longer relaxation to equilibrium.

coherence, increases to a maximum before a gradual decrease starts. The timescale to reach the peak increases at higher coherences, and the peak in total transverse spin amplitude increases with the initial coherence. A numerical simulation for the highest initial coherence of $c_{\text{init}} = 0.71$ is shown, where there is good qualitative agreement with data.

This increase in the total transverse spin amplitude demonstrates that the transverse spin is not just undergoing classical diffusion. The appearance of coherence near the cloud edges is not due to spin diffusion, but rather to conversion of longitudinal to transverse spin as a result of an instability in the longitudinal spin current. This effect has been observed in spin-polarized gas systems [56, 126] and was described as an experimental manifestation of the Castaing instability [127]. Although the trapped atomic system possesses different experimental parameters, the physics governing the phenomenon are similar [59, 58, 128].

To explain this instability, we consider the case of transverse spin confined to the domain wall with a flat differential potential. Here the transverse spin quickly dephases because of the longitudinal spin gradient. This longitudinal gradient then decays via ordinary longitudinal diffusion since for large dephasing the quantum Boltzmann equation decouples for longitudinal and transverse spin components [59, 129]. However, if the ISRE is large enough, the longitudinal spin current becomes unstable, and coupling between longitudinal and transverse spin diffusion occurs. The longitudinal gradient then decays via transverse diffusion across the coherent domain wall. The longitudinal spin diffusion timescale is lengthened by coupling to the slower transverse spin diffusion through the ISRE. The conversion of longitudinal spin, through this coupling, increases the total transverse spin amplitude by up to a factor of two (see Fig. 5.8).

To be clear, this instability does not violate conservation of spin, because the total transverse spin amplitude is not a conserved quantity. The total longitudinal spin $\sum_i M_z(z_i)$ is conserved, and it is approximately zero after the initial spin state preparation. In a rotating frame with zero dephasing, the two transverse spin components $\sum_i M_x(z_i)$ and $\sum_i M_y(z_i)$ are also conserved, and both quantities are approximately zero after the initial spin state preparation. The total transverse spin amplitude is a measure of the ensemble coherence, which increases at early times and approaches zero at long times.

To understand how cloud parameters change the strength of the spin instability, we numerically simulated spin diffusion for various cloud temperatures T , peak density n , s-wave scattering lengths a , and domain width λ . The strength of the instability

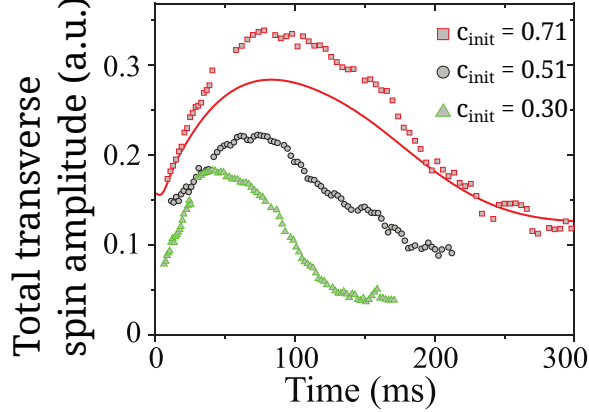


Figure 5.8: The time evolution of the total transverse spin amplitude (or ensemble coherence) for Fig. 5.7. The solid curve is a numerical simulation of Eqn. 2.46 for $c_{\text{init}} = 0.71$, showing good qualitative agreement. Quantitative agreement is limited by challenges extracting Ramsey fringe amplitudes in the presence of noise, dephasing, and a small signal in the cloud wings.

is characterized by the ratio of the initial coherence to the peak coherence, which is around two in Fig. 5.8. In Figure 5.9, the strength of the instability is shown for varying temperature, s-wave scattering, and domain width. The instability is strongest at low s-wave scattering lengths, small domain widths, and high temperatures. At low s-wave scattering lengths, the ISRE strengthens as $\mu \propto 1/a$ (see Eqn. 2.40), and the domain-crossing longitudinal spins are adiabatically rotated through the transverse plane. For small domain widths, there are fewer collisions as spins move across the domain wall, so the spins do not follow the local spin. Instead, a longitudinal spin acquires a transverse component after passing through the domain wall, because only a few collisions occurred. Similarly, for higher temperatures the instability is increased because atoms move faster through the domain wall. For the spin instability to manifest, the system must have strong spin-exchange interactions ($\mu > 1$ of Eqn. 2.40) and a small number of collisions when crossing the domain wall ($\ell \sim \lambda$).

5.4 Summary

In this chapter, spin diffusion of a helical spin domain was explored in the nondegenerate regime. The presence of transverse spin between spin domains, and the ISRE, leads to slower than classical diffusion time. When spins cross the domain, the ISRE-mediated collisions rotate the spins so that they approximately follow the local spin. This following of local spin was shown to be less effective by reducing the initial

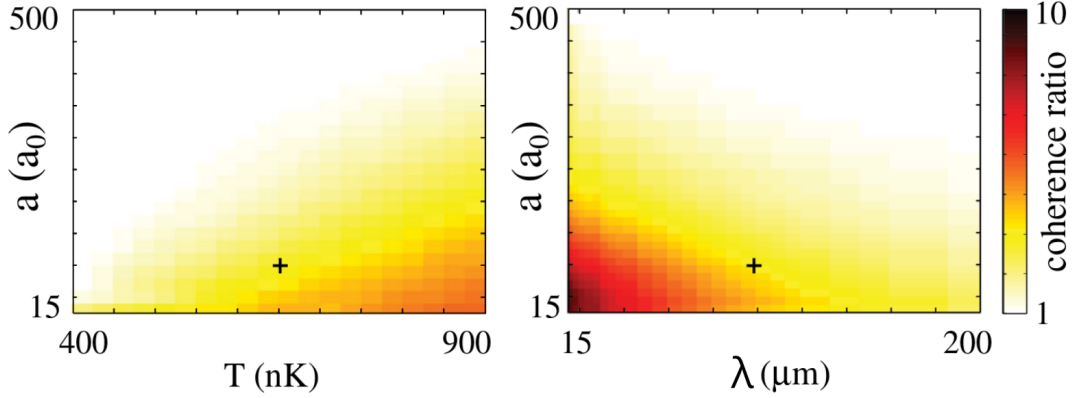


Figure 5.9: Instability onset seen in the ratio of the maximum ensemble coherence to initial coherence, $c_{\max}^{\text{tot}}/c_{\text{init}}^{\text{init}}$, from simulations of Eqn. 2.46, plotted logarithmically to highlight the instability threshold. The s-wave scattering length a is varied with (a) cloud temperature T or (b) domain width λ . All other parameters are set to the conditions of Fig. 5.7(a) and $c_{\text{init}} = 0.51$. Since the ISRE strength scales as $\mu \propto 1/a$, increasing a diminishes the instability, as collisional damping grows faster than exchange scattering. Decreasing T or increasing λ stabilizes the spin current as expected, through increasing adiabatic rotation during domain wall crossing. Crosses represent the experimental conditions used in our study.

spin coherence, where spin diffusion sped up at low coherence. A spin instability in the longitudinal spin current was found that converts longitudinal spin to transverse spin. This conversion of spin increases the total ensemble coherence, and numerical simulations suggest that higher temperatures and smaller domain widths can increase the magnitude of this instability. The initial coherence was shown to be an important factor in modifying spin diffusion, where high coherence slows spin diffusion. However, the differential potential also plays an important role in spin diffusion, so the effects of the differential potential are explored in the next chapter.

Chapter 6

Stable spin domains

This chapter presents the stabilizing effect that a linear effective magnetic field gradient has on spin diffusion. The chapter is adapted from the article “Stable spin domains in a nondegenerate ultracold gas” published in Physical Review A [130]. The linear differential potentials are created using the AOM technique described in Section 3.7 that makes use of the spin-dependent potentials discussed in Section 2.5. An initial helical spin domain is prepared in a cloud of varying temperature and peak density. Then spin diffusion is measured with various linear differential potentials applied to the spin domains. For certain positive gradients, the spin domain is stabilized and a method to experimentally determine these stabilizing gradient is described. The stabilizing gradients show good agreement to theoretical predictions for the stabilizing gradient in the hydrodynamic limit.

6.1 Effect of linear differential potentials

A laser detuned ~ 3.4 GHz from the D_2 excited-state transition creates a differential energy shift that locally alters Larmor precession, analogous to a magnetic field gradient torquing real spins (see Sec. 2.5). The applied linear differential potential is characterized by $U_{\text{diff}} = Gz$, where z denotes the axial position along the cloud, and G is the gradient of the potential. The AOM-generated potentials discussed in Section 3.7 are used to create these linear potentials. The gradient G can be adjusted with laser intensity and the sign is adjusted with relative phase between the amplitude- and frequency-modulation to the AOM. In all experiments, laser intensity is low enough that loss from spontaneous emission is below other loss processes, such as dipolar relaxation in $|2\rangle - |2\rangle$ collisions. While the previous chapter presented the slowing of longitudinal spin diffusion caused by the presence of coherence in the do-

main wall, the addition of a small linear differential potential modifies spin diffusion further.

Spatially varying differential potentials modify the ISRE and can generate collective spin behaviour because collisions between spins depend on their relative phase. In particular, Figure 6.1 shows that the addition of a small differential potential gradient ($G = 54$ Hz/mm) stabilizes the domains against both diffusion and trap oscillations. This stabilizing effect extends diffusion timescales further than the slowing caused by adiabatic following that was discussed in Section 5.1. The observed spin domain stabilization cannot be due to differential mechanical forces because the differential potential is much smaller than the trapping potentials. For instance, a 50 Hz/mm field gradient shifts the relative trap centers by only $0.1 \mu\text{m}$, less than 0.1% of the Gaussian half width of the distribution z_0 . Instead, the stabilizing effect is driven by coherent spin interactions via the ISRE that are modified by the linear differential potential. The spatially varying precession rate of transverse phase counteracts the phase precession caused by the longitudinal spin profile (see Eqn. 2.46).

The sign of the differential potential gradient plays an important role in modifying spin diffusion. Figure 6.1(c) shows the longitudinal spin evolution for a negative gradient and spin diffusion has been sped up compared to the zero gradient case in Fig. 6.1(a). The initial helical spin profile generates a spin current that drives the system to equilibrium, leading to an oscillation at 250 ms as in Fig. 6.1(a). The spatially varying Larmor precession also ends up generating a spin current through ISRE collision events. The longitudinal component of these two spin currents can be in the same direction ($G < 0$) and speed up spin diffusion, or the currents can act in the opposite direction ($G > 0$) and slow spin diffusion. For a specific positive gradient, spin diffusion can be stopped and the spin domains are stabilized for up to 600 ms. After that time, losses in the system lead to a change in the spin profile. These losses lower the effectiveness of the applied gradient, and the spin profile is further damped.

6.2 Tracking domain stability

The addition of a linear differential potential can significantly modify spin diffusion, and even stop it. In stable domains, the longitudinal spin diffusion is stopped and the longitudinal spin profile is constant in time. In this section, the stability of these spin domains is explored experimentally and theoretically to identify the conditions required to stabilize spin domains.

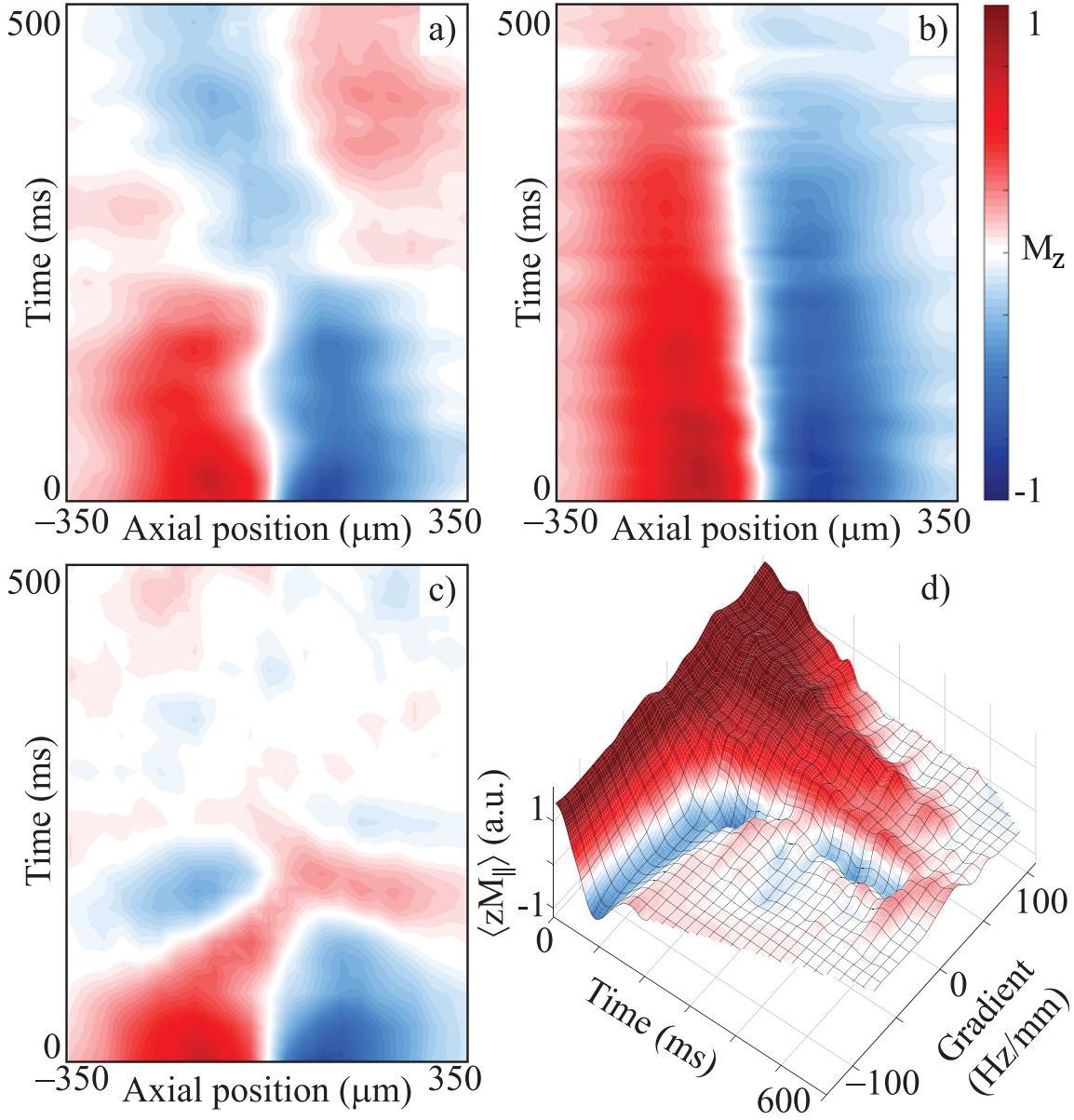


Figure 6.1: Spatiotemporal evolution of radially averaged M_z for $T = 650$ nK and peak density $n_0 = 1.4 \times 10^{13} \text{ cm}^{-3}$ at $G = 0$ Hz/mm (a), 54 Hz/mm (b), and -19 Hz/mm (c). The initial domain undergoes dipole oscillations at $G = 0$, which increase in frequency and damping rate for $G < 0$. Positive gradients stabilize the initial domain wall configuration. The domain wall drifts toward the $M_z = 1$ domain over time, since the $|2\rangle$ state decays via dipolar relaxation. d) Time evolution of the spin dipole moment, $\langle zM_z \rangle$, in different effective field gradients. $\langle zM_z \rangle$ oscillates for $G \leq 0$, but stabilizes for positive gradients. Larger G also leads to faster damping, through decoherence from the inhomogeneous applied field.

Analysis of the quantum Boltzmann equation (Eqn. 2.46) with a linear differential potential, $U_{\text{diff}}/\hbar = Gz$, reveals the existence of steady-state solutions featuring two oppositely oriented longitudinal spin domains ($M_z = \pm 1$) joined by a narrow domain wall [131, 127, 132]. In the collisionless limit ($\tau \rightarrow \infty$), Fomin derived a relation between the applied field gradient G and the equilibrium size of the domain wall λ_{eq} in a normal Fermi liquid [131]. Following these predictions and the work in Ref. [59], the spin domain stabilizing gradient for a trapped gas of bosons in the hydrodynamic limit ($\tau \rightarrow 0$) is [133]

$$G_{\text{hydro}} = \frac{\omega_z}{z_0} \frac{1}{\mu M} \left(\frac{\pi/2}{1.1\lambda_{\text{eq}}/z_0} \right)^3 \omega_z \tau, \quad (6.1)$$

which scales as T/n . Here τ is the elastic collision time, which scales with the inverse of the cloud density $\tau \propto n^{-1}$. To provide the spin rotation required to maintain stable domains, the domain wall must be nearly fully polarized – that is, a helical domain wall where the spin smoothly rotates from one longitudinal orientation to another.

This hydrodynamic prediction was tested by studying the behaviour of the stable domains, specifically the dynamics of the domain wall. The domain wall is characterized by a fit to a phenomenological model, $M_z(z, t) = \exp(-z^2/2z_0^2) \tanh(z/\lambda(t))$, where the domain wall width $\lambda(t)$ varies in time. This phenomenological model is the atomic density profile multiplied by a sigmoid, and approximately describes the spin domain. The hyperbolic tangent was chosen due to ease of computing, integration, and differentiation, but another sigmoid could be used to describe the spin domain. With this model, the initial domain wall width is $\lambda_0 \simeq 73(3) \mu\text{m}$ and the fit to the spin profile is shown in Fig. 6.2(a). The dynamics of λ with different differential potentials applied is used to determine the relationship between the gradient G and stable domain-wall width λ_{eq} . Here we assume that the initial domain-wall width λ_0 is close to the stable domain-wall width λ_{eq} so that the spin profile will relax to the stable domain-wall width at short times. When the applied gradient is small, λ_{eq} is much larger than the initial domain wall width λ_0 , and the domain wall relaxes until it matches λ_{eq} for that gradient. For a large gradient, the opposite happens and the domain wall shrinks towards λ_{eq} . By applying a specific gradient such that $\lambda_{\text{eq}} = \lambda_0$, the domain wall width remains constant and no dynamics are observed. Eventually, dephasing from the linear differential potential removes enough coherence so that $\mu M < 1$. This dephasing can lead to faster damping of the longitudinal spin profile, and classical diffusion dominates once enough coherence is removed.

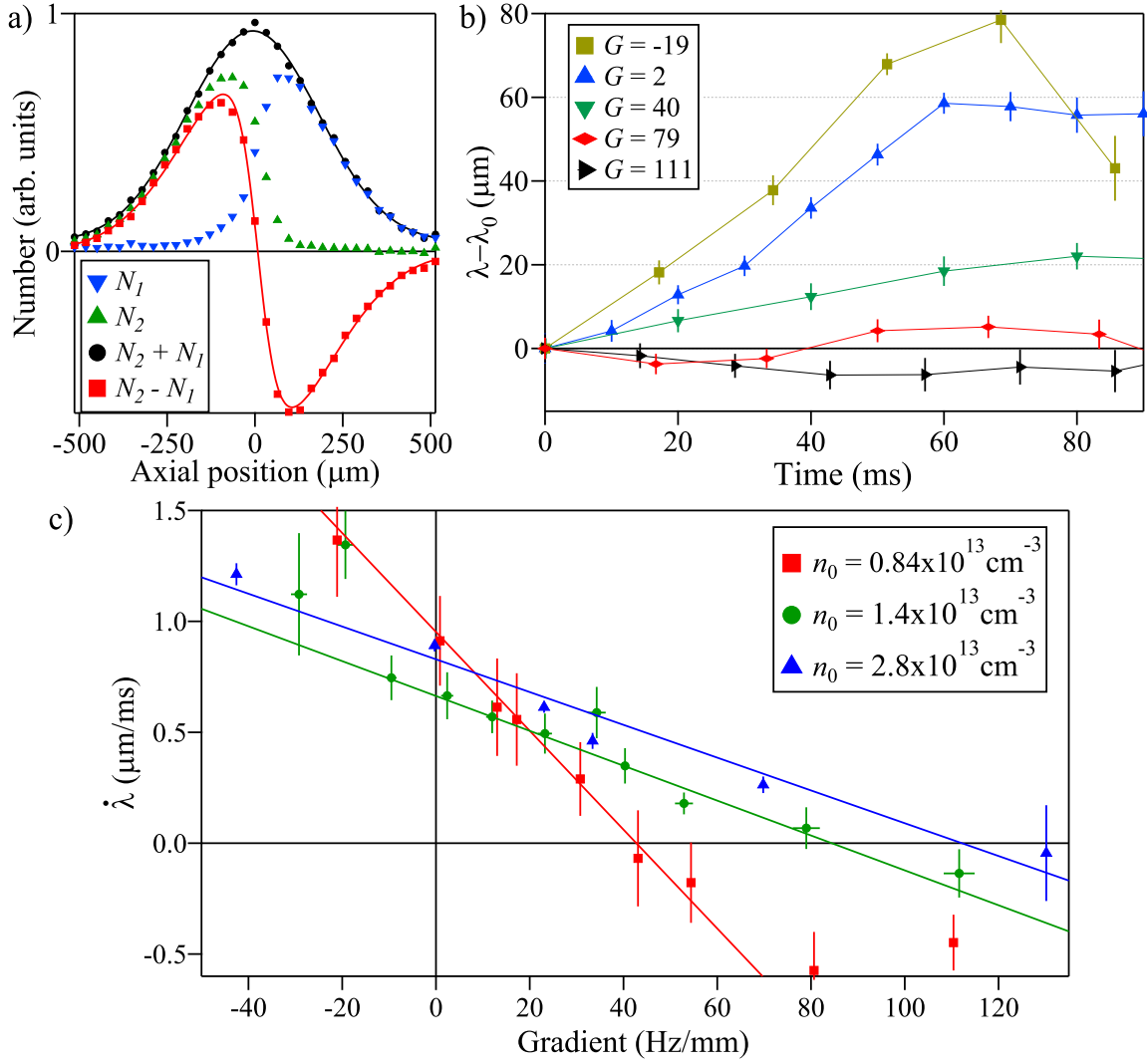


Figure 6.2: a) Normalized distribution of atoms in state $|1\rangle$ ($N_1(z)$, \blacktriangledown) and state $|2\rangle$ ($N_2(z)$, \blacktriangle) at $T = 650$ nK and $n_0 = 2.8 \times 10^{13} \text{ cm}^{-3}$. A Gaussian is fit to the sum (\bullet) to extract temperature. The difference $M_z = N_2 - N_1$ (\blacksquare) is fit with the same Gaussian multiplied by $\tanh z/\lambda$ to determine domain wall width λ . b) Time dependence of λ immediately after application of G (given in Hz/mm), exhibiting linear relaxation at short times. c) Initial domain-wall relaxation rate $\dot{\lambda}$ for three densities as a function of effective field gradient G . Uncertainties represent statistical uncertainty in fitting $\dot{\lambda}$ due to shot-to-shot temperature and density fluctuations. A linear fit is performed to determine the gradient G_0 that stabilizes the initial domain wall λ_0 .

The domain-wall dynamics are examined at short times to experimentally determine the stabilizing gradient G_0 . Significant transients are observed during relaxation to the steady state, and damping of those transients removes magnetization, as does decoherence driven by the inhomogeneous effective field. Waiting for equilibration reduces M , which changes the domain width at equilibrium λ_{eq} . The short-time behaviour is studied out to 100 ms after initial preparation, where μM is roughly constant. These times are much shorter than damping timescales so that the stabilizing gradient G_0 for the initial domain-wall width λ_0 is determined in a fully polarized system.

Figure 6.2(b) shows the initial behaviour of $\lambda(t)$ for several gradients, where again $\lambda(t)$ comes from phenomenological fits to $M_z(z, t)$. At short times, the domain width relaxes to the stable domain width λ_{eq} determined by the applied gradient (see Eqn. 6.1). Damping occurs at long times as the system relaxes to the true equilibrium state - a uniform spin distribution. In the short timescales where damping is negligible, $\lambda(t)$ is approximately linear, and the rate of relaxation $\dot{\lambda}$ depends on the difference between the initial domain width λ_0 and λ_{eq} . Figure 6.2(c) displays $\dot{\lambda}$ versus G ; the horizontal intercept gives the gradient G_0 that produces the stable domain solution where $\lambda_{\text{eq}} = \lambda_0$ and $\dot{\lambda} = 0$.

Density and temperature play important roles in the relationship between λ_{eq} and G_0 in Fig. 6.3. At high density, the system nears the hydrodynamic regime and diffusion is inhibited; thus, a smaller gradient G_0 is needed to counteract spin gradients. Fig. 6.3 shows the Knudsen number, $\text{Kn} = \ell/\lambda_0$, calculated at the domain-wall center using the mean free path ℓ and $\lambda_0 = 73 \mu\text{m}$. The Knudsen number is a dimensionless number that is used as a metric to classify the fluid flow of a system, with the limits corresponding to hydrodynamic flow ($\text{Kn} \ll 1$) and free atomic flow ($\text{Kn} \gg 1$). As Kn decreases to 1, though still in the crossover region between collisionless and hydrodynamic behaviour, the $1/n$ dependence of G_{hydro} agrees well with measured values of G_0 . Since the atom cloud is collisionally thick at high n_0 and atoms are more localized, the radially averaged density in G_{hydro} is used, instead of an ensemble average. Note that due to the λ_0^{-3} dependence in Eqn. 6.1, the uncertainty in G_{hydro} is 15%.

Furthermore, when the temperature is lowered at high density, the measured G_0 decreases. The quantitative agreement with G_{hydro} is better at $T = 650 \text{ nK}$ than at 425 nK , as assumptions contained within the hydrodynamic model (Eqn. 6.1) become more strained at lower temperature - namely, that $\lambda_0 \ll z_0$ and $\omega_z \tau \ll 1$. The former ensures slow, or unbounded, diffusion, while the latter is necessary for a large

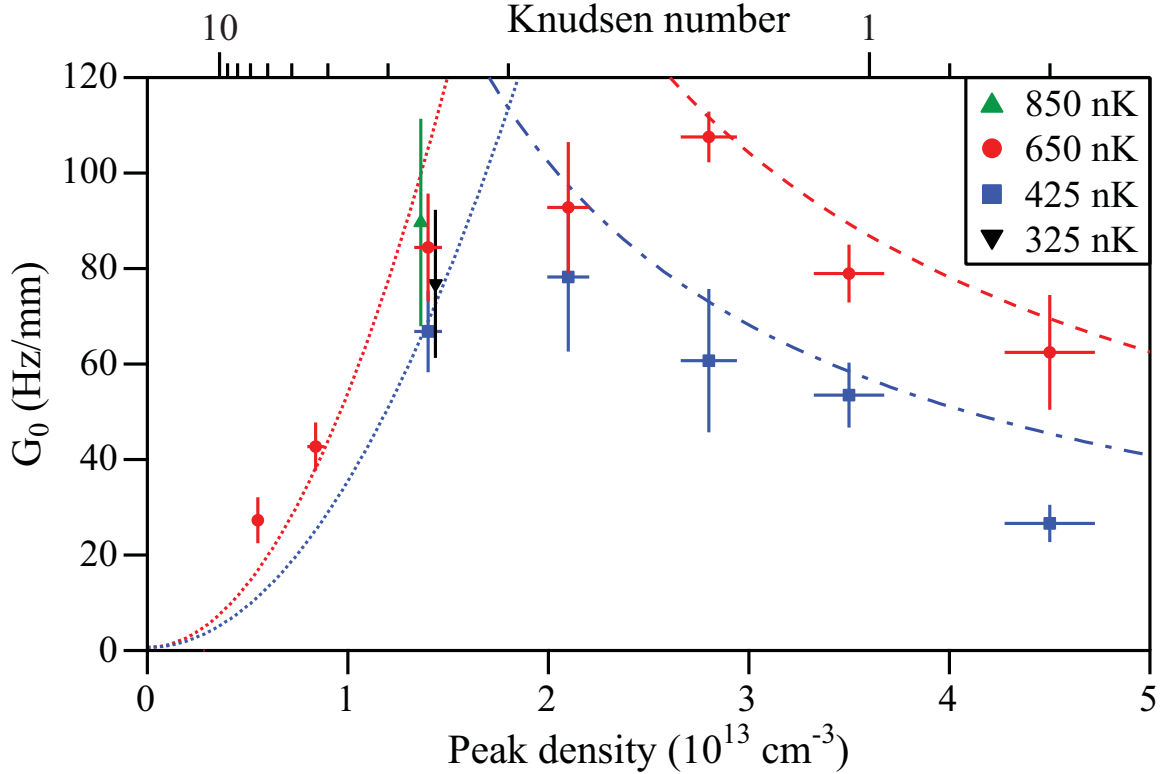


Figure 6.3: Stabilizing gradient G_0 as a function of peak density and temperature for $\lambda_0 = 73 \mu\text{m}$. Points at $n_0 = 1.4 \times 10^{13} \text{ cm}^{-3}$ have been horizontally offset for clarity. The data spans the crossover from collisionless to hydrodynamic regimes, as indicated by the Knudsen number for $\lambda_0 = 73 \mu\text{m}$. The data is described by G_{hydro} at high density for $T = 650 \text{ nK}$ (dashed) and 425 nK (dash-dot). Dotted lines show G_{hydro} for $\lambda_{\text{eq}} = \ell_{3\text{D}}$ ($\text{Kn} = 1$), demarcating the region where the hydrodynamic model's prediction of a steady-state solution for some λ_0 is expected to be valid.

enough collision rate to ensure local equilibrium in the spin current. However, since the ISRE strength μ increases at lower temperatures T , the approximation $\mu M \gg 1$ strengthens as collisions become more quantum in nature. The highest density point at $T = 425$ nK has $T/T_c = 1.08$, and shot-to-shot fluctuations may occasionally include small condensates, which are inclined to phase separate to minimize energy in even small field gradients.

At low densities of $n_0 \lesssim 2 \times 10^{13} \text{ cm}^{-3}$, the hydrodynamic approximation breaks down, and the measured gradient G_0 deviates from the predicted gradient G_{hydro} . The ultimate limits of the hydrodynamic model are shown by the dotted lines in Fig. 6.3, where G_{hydro} is evaluated for the largest λ_{eq} that satisfies $\text{Kn} = 1$ for a given n_0 and T , i.e. $\lambda_{\text{eq}} = \ell_{3\text{D}}$. Here $\ell_{3\text{D}}$ uses an ensemble-averaged density that is more appropriate in the low-density limit, instead of the radially averaged Kn shown on the Fig. 6.3 axis. The hydrodynamic model predicts that steady-state domains exist for the parameter space to the right of the dotted lines, but does not guarantee the existence of any stable domains to the left. These two dotted lines represent where the hydrodynamic prediction breaks down. For our narrow domain-wall widths, no analytic collisionless model for stabilizing gradients currently exists. Coincidentally, at low densities the measured value of the stabilizing gradient corresponds roughly to the limiting case of $\lambda_{\text{eq}} = \ell_{3\text{D}}$. R. Ragan performed [130] a linearized moment-method analysis of Eqn. 2.46 in the collisionless limit, which suggests that steady-state solutions do indeed exist for large domain walls ($\lambda_0 > z_0$) at small gradients. However, it is not clear that narrow domain-wall preparations such as initialized here can be stabilized in the collisionless regime.

Low density complicates the experimental technique of using domain-wall relaxation to find G_0 . The second-lowest density in Fig. 6.3, $n_0 = 0.84 \times 10^{13} \text{ cm}^{-3}$, shows unambiguous signatures of steady-state domains and behaviour consistent with higher values of n_0 , but the G_0 found for $n_0 = 0.55 \times 10^{13} \text{ cm}^{-3}$ may not truly represent a stable domain solution for $\lambda_0 = 73 \text{ }\mu\text{m}$. Large transients are observed here, where the initial spin current lies further from its equilibrium value, and rapid dephasing in the collisionless regime renders analysis of $\dot{\lambda}$ less reliable in determining G_0 . It is likely that the measurement of G_0 at this density is tainted by transients and also represents an average value for $0 < M < 1$ due to dephasing. Indeed, analysis of $\dot{\lambda}$ for very short times ($t < 8$ ms) and small gradients ($G < 40$ Hz/mm) suggests that G_0 should be several times higher; however, measurements at higher G reveal only rapid dephasing and even faster domain-wall relaxation rates. Thus it appears that

steady-state solutions, for our initial spin preparation and dephasing times, may not exist for narrow domain walls in the collisionless limit.

6.3 Transverse spin waves

So far only the longitudinal spin component has been shown, but spin diffusion happens in both the longitudinal and transverse spin channels. To understand the stability of the domains it is important to examine the behaviour of the transverse spin $\underline{\mathbf{M}}_{\perp} = M_{\perp}e^{i\phi}$. For the conditions in Fig. 6.1(b) the dynamics of $\underline{\mathbf{M}}_{\perp}$ are studied by applying a $\pi/2$ -pulse after a variable delay time to produce Ramsey fringes as in Section 3.5.2. The amplitude and phase of the Ramsey fringes are the transverse amplitude M_{\perp} and phase angle ϕ , respectively. There are several striking features in the behaviour of $\underline{\mathbf{M}}_{\perp}$ (Fig. 6.4). First, $\underline{\mathbf{M}}_{\perp}$ undergoes phase oscillations, i.e. a dipolar transverse spin wave. This represents a decoupling in dynamics between a purely transverse spin wave and the stable longitudinal spin domains, as opposed to the coupled transverse-longitudinal spin dynamics observed in Chapter 5 at $G = 0$. The frequency of this spin wave approaches ω_z , consistent with strongly driven, highly nonlinear dipolar spin waves [68]. Secondly, stable longitudinal domains trap the transverse spin wave within the domain wall because the transverse spin cannot diffuse into the stable longitudinal domains.

A confined purely transverse spin wave is necessary to support the steady-state domains. Atoms oscillate within the trap at the trap frequency of 6.71 Hz, so the longitudinal spins must coherently transfer between spin states as they pass through the domain wall. The precessing transverse spin wave mediates this longitudinal spin rotation as atoms move across the domain wall from $M_z = 1$ to -1 . Fig. 6.4 shows the oscillation of the transverse phase corresponding with the frequency of the motion of the atoms. Though the microscopic spins remain coupled via the ISRE, the macroscopic spin decouples completely. By contrast, in the absence of an effective field gradient, the longitudinal spin gradient induces spin currents that determine the transverse phase gradient. However, longitudinal domains are unstable at $G = 0$ and undergo dipole oscillations, dragging the transverse phase with them and leading to rapid collapse and revival of M_{\perp} as shown in Fig. 5.3.

In summary, this chapter has so far demonstrated the stabilization of spin domains in a nondegenerate gas using optically-induced effective magnetic field gradients. These gradients are used to modify spin diffusion by speeding, slowing, and stopping diffusion between domains. For specific gradients, the domain lifetimes are

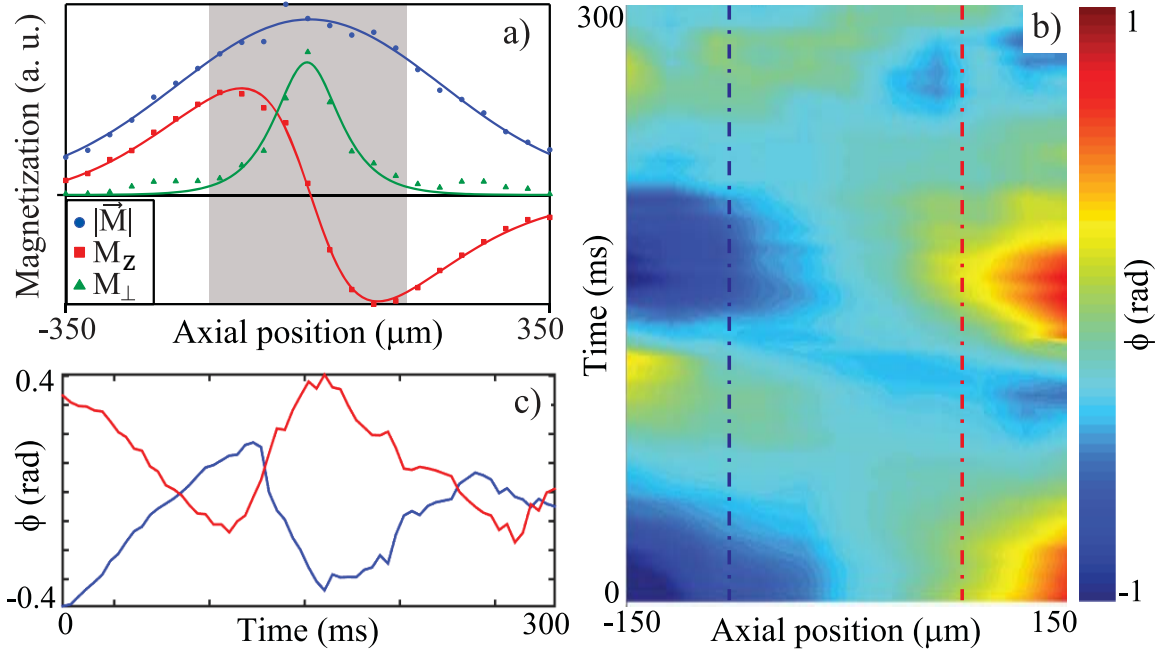


Figure 6.4: a) Initial transverse spin magnitude M_\perp as measured from Ramsey fringe amplitudes. Also shown are M_z and M . Minimal decoherence is expected during the short preparation sequence. Any discrepancies in $M \simeq \sqrt{M_z^2 + M_\perp^2}$ are attributed to noise degrading Ramsey fringe fits. Solid lines are fits to a Gaussian (M), and the same Gaussian multiplied by $\text{sech } z/\lambda$ (M_\perp) and $\tanh z/\lambda$ (M_z). b) Spatiotemporal evolution of the orientation of $\underline{M}_\perp(z, t)$, from the shaded region in a). c) The time evolution of ϕ exhibits dipolar spin wave oscillations, highlighted for two locations in the domain wall [dotted lines in (b)].

shown to be more than 30 times the classical diffusion time. This effect is driven by quantum symmetry in microscopic atom-atom interactions, and leads to decoupling of the dynamics of the longitudinal spin domains and a trapped transverse spin wave. These results show good agreement with a hydrodynamic approximation at high density and suggest limitations to steady-state domains in the collisionless limit.

6.4 Towards arbitrary control of 1D spin diffusion

The final section of this chapter presents our first steps towards generic control of spin diffusion in an ultracold gas. This arbitrary control is achieved using a digital micromirror device (DMD) to replace the acousto-optical modulator (Section 3.7) and masking method (Section 3.2). The DMD permits the generation of arbitrary initial spin profiles and arbitrary differential potentials. Specifically, we demonstrate temporal and spatial control of spin-dependent potentials. For temporal control the sign of the differential potential is flipped midway through the diffusion. And for spatial control a three-domain initial spin profile is stabilized.

In Fig. 6.5(a) a two-domain spin profile is prepared and spin diffusion is observed for an applied positive gradient for 25 Hz/mm. After 150 ms, the sign of the gradient characterizing the differential potential is flipped so that the gradient is -25 Hz/mm after the dashed line shown in Fig. 6.5(b). Spin diffusion occurring after 150 ms matches the case of initially applying a -19 Hz/mm gradient, as shown in Fig. 6.1(c). The timescale is slightly sped up by a small decrease in M over the first 150 ms and by the small increase in size of the negative gradient. This speed up is minimal as the spin domains oscillate and decay on the same timescale as if the gradient were initially negative. This test of the DMD shows that a single pattern change is fast enough that no additional dynamics are generated during the flip between positive and negative gradients. This means that when switching DMD patterns the scattered light from the mirrors flipping is insignificant because the new DMD pattern is the main modification to spin diffusion.

The spatial control of the DMD is tested by preparing a three-domain spin profile and watching the system evolve. At the cancellation spot the three domains evolve as in Fig. 6.6(a), where the spin domains oscillate and damp. The oscillation and damping rates here are about twice as fast as the rates for a two-domain profile and agrees with previous work with higher order spin domains [68]. A stabilizing differential potential is applied to the three-domain profile to observe simultaneous stabilization of three domains in Fig. 6.6(b). The stabilizing differential potential here

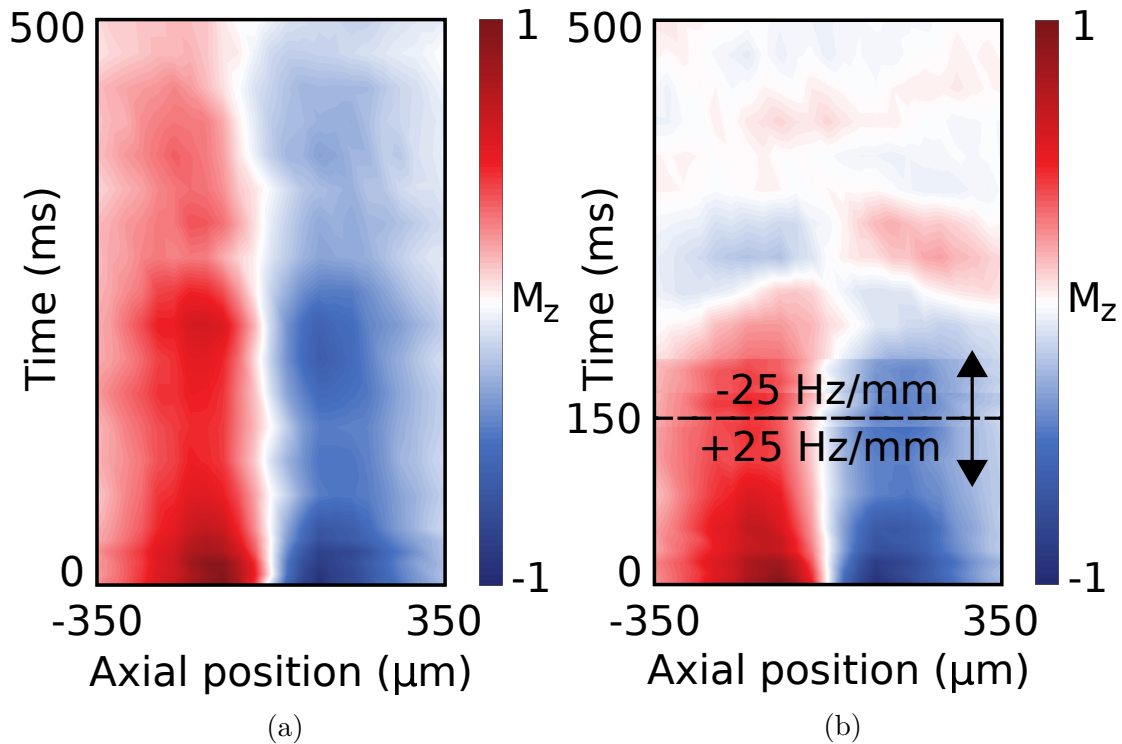


Figure 6.5: (a) A long-lived domain is shown with a differential potential gradient of 25 Hz/mm applied the entire time. (b) The gradient starts at 25 Hz/mm, but the DMD pattern is flipped at 150 ms to change the gradient to -25 Hz/mm. After flipping the gradient the spin domains oscillate and damp as expected. No additional dynamics were generated by the DMD pattern inversion, demonstrating that the pattern switching rate of 22 kHz is fast enough.

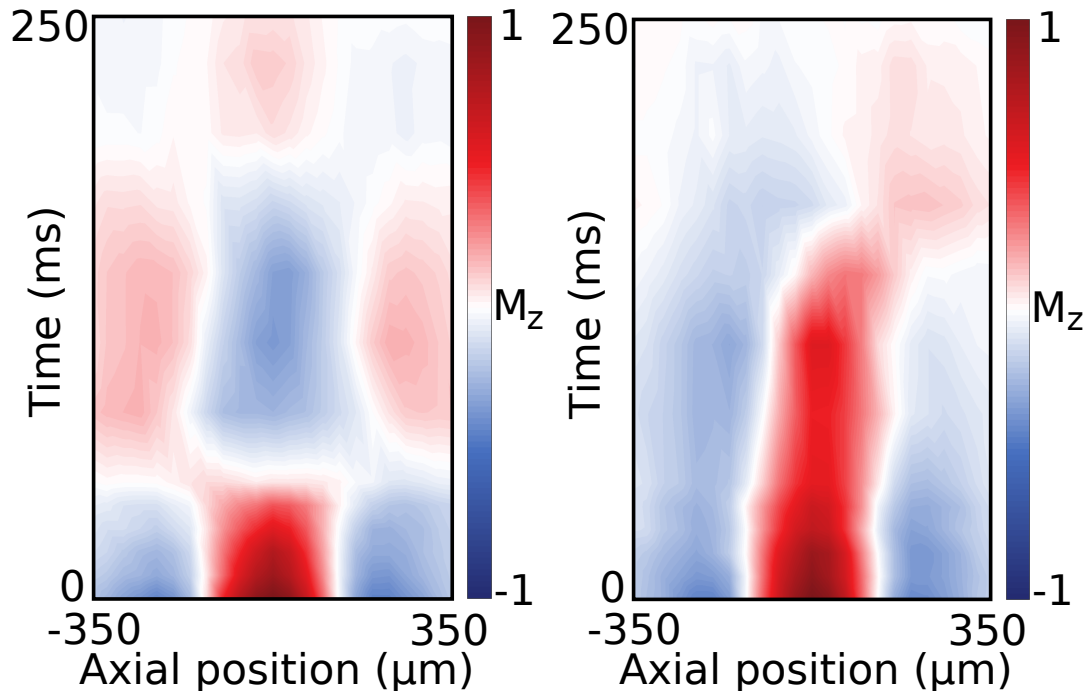


Figure 6.6: (a) Longitudinal spin diffusion of a three-domain initial spin profile at the cancellation spot. The quadrupolar spin domain oscillates and decays faster than the dipole spin profile. (b) Long-lived three-domain spin profile with an applied stabilizing differential potential. With better optimization of the differential potential, the lifetime could be extended and the drift of the domains could be corrected.

is two gradients of opposite sign, each centered on different spin domain walls. The stabilized domains persist longer than the domains in a flat differential potential, but should damp faster because of the higher spatial mode [68]. The stabilizing differential potential was not well optimized here, so the spin domains drift to the right and the three-domain lifetime may not be maximal. With more work to optimize the differential potential, it should be possible to stabilize three-domain spin profiles to at least 300 ms. This test of spatial control of the initial spin profile and differential potential demonstrates that arbitrary spin profiles and arbitrary differential potentials are now possible.

These two tests of arbitrary control over the initial spin profile and differential potential are crucial for full control over spin diffusion. More complex initial domains can be formed with feature sizes as small as the DMD focus of around $25 \mu\text{m}$, allowing for up to 14 spin domains across the cloud. The temporal and spatial control of the differential potential provides fine control over how fast and where in the cloud the spins precess. These domain manipulation techniques using the DMD demonstrate the

possibility of further spin diffusion studies where spin domains could be individually manipulated.

Chapter 7

Conclusion

In Chapter 2, the ISRE was shown to provide a spin rotation during collisions between atoms. A quantum Boltzmann transport equation was presented that describes spin diffusion in our experiments. The numerical simulation procedure was discussed and a dynamic time stepping protocol was presented. This protocol offers better stability of numerics during the simulation.

The apparatus was presented in Chapter 3, along with the a phase space of accessible temperatures and densities that can currently be achieved. The implementation of detecting longitudinal and transverse spin components was presented, along with two protocols for measuring transverse spin that improve upon the moving window method. Combining the spin components was shown to assist in creating and understanding the initial spin profiles. A masking technique that allows for two-domain spin profiles to be generated easily during spin preparation was presented. Followed by a discussion of the generation of simple spatially varying differential potentials using an AOM. Lastly, the replacement of the masking and AOM techniques with a single DMD was presented. The DMD makes it possible to create more complex initial spin profiles and differential potentials.

The apparatus requires consistent calibration to maintain ease of operation. Some of these calibrations were presented in Chapter 4. The typical ultracold atom calibrations were discussed as well as apparatus specific calibrations. A technique to optimize the detuning across the cloud during initial spin preparation was shown. This optimization technique was particularly useful for generating spin profiles that have minimal phase wrapping between longitudinal domains.

This thesis described two techniques that are demonstrated to modify spin diffusion in a weakly-interacting nondegenerate ultracold gas of rubidium-87. The diffusion

of a two-domain spin profile was modified by reducing the initial coherence in the domain wall and by applying linear differential potentials across the cloud.

By reducing the initial coherence of the initial spin profile, Chapter 5 showed that the presence of coherence between spin domains lengthens diffusion times via the ISRE partially converting spins as they move between domains. The reduction of the initial coherence increases spin diffusion until the classical diffusion limit is reached. A spin instability that converts longitudinal spin to transverse spin was also observed, leading to an increase in total ensemble coherence. Finally, numerical simulations of the instability predicted that its strength is increased at higher temperatures and for narrower domain-wall widths.

In Chapter 6 it was shown that differential potentials with a negative gradient speed spin diffusion, while positive gradients slow spin diffusion. For positive stabilizing gradients, the spin current generated from the spin profile was effectively cancelled by the current generated by the gradient. Spin diffusion was effectively stopped with this stabilizing gradient and spin domains were observed to persist for up to 600 ms. The stability of these spin domains was mapped out as a function of temperature and density, and short-time domain-wall dynamics were used to measure the stabilizing gradient. The measured stabilizing gradients were compared to a hydrodynamic prediction and showed good qualitative agreement. Lastly, a digital micromirror device was introduced and tested. It will allow the exploration of spin diffusion for arbitrary differential potentials and initial spin profiles.

The control of initial coherence and applied differential potential can be applied to other bosonic spin systems, where spin diffusion in those systems should be similarly modified. By demonstrating these fundamental methods of controlling spin diffusion, spin diffusion can now be explored for initial spin profiles with more domains and for temporally varying differential potentials. Some ideas for future experimental enhancements are discussed in Section 7.1 and suggestions for future experiments are discussed in Section 7.2.

7.1 Future enhancements

The observable in this thesis was the spin density $\underline{\mathbf{M}}(z, t)$, which depends on time and axial position. However, the quantum Boltzmann equation is a dynamical equation for the spin density distribution $\underline{\mathbf{m}}(z, p, t)$, which includes a dependency on the momentum distribution of the spins. Measuring the spin density averages over the momentum coordinate, but the momentum coordinate could be useful when comparing

spin diffusion to the quantum Boltzmann equation. The first suggestion is to design an easily switchable imaging setup that can observe the spin density averaged along either position or momentum. Imaging of the spin density averaged over momentum was used in this thesis, while imaging the spin density averaged over position requires longer time of flight images of 10 – 50 ms. This requires the camera field of view to be increased so the camera can view the expanded cloud. Additionally, the magnetic field must be flat over the size of the expanded cloud so that it does not alter the expansion. To be flexible in imaging the spin distribution, a mirror on a flip mount could be used to switch between the separate optical paths used to measure either the position- or momentum-averaged spin density. Alternatively, a computer controlled translation mount could be used to create a zoom lens that toggles between imaging the spatial- or momentum-averaged spin density. The main challenge of imaging the longer time of flight is that additional spin diffusion will occur during the expansion time, which will alter the measured spin density.

A second enhancement of the apparatus would be to develop a method to measure spin density non-destructively in situ, instead of destructively. In-situ imaging would reduce the number of experimental runs required to generate a single plot exploring the influence of some parameter on longitudinal spin diffusion. Other atomic physics groups have shown that, through the use of Faraday rotation effect, the density of atoms can be imaged with minimal action on the quantum state [134, 135]. In-situ imaging of a spin-1 atomic BEC was discussed in Ref. [136], in which the dielectric tensor was modified by altering the probe laser frequency to select a spin component. This process could be adapted to our pseudo-spin-1/2 system in order to measure longitudinal spin in situ, which would significantly speed up data collection. One thing to be cautious about this proposed enhancement is that applying any light to the atom cloud can alter the differential potential, which then unintentionally modifies spin diffusion. Extreme care should be taken to ensure the beam intensity and polarization are uniform so that additional contributions to the differential potential are spatially uniform.

The permanent magnets used in this system work well for field stability and for generating large magnetic field gradients with zero current. However, the permanent magnets restrict the geometry of the cloud to a quasi-1D configuration. Replacing the permanent magnets with magnetic field coils would allow for greater tunability in cloud geometries and permit studies of spin diffusion in higher dimensions. Spin diffusion in a 2D cloud geometry is particularly interesting for this experiment because

the second dimension of DMD patterns could be used to control the 2D differential potential to modify 2D spin diffusion.

Finally, the π - and $\pi/2$ -pulses used for state transfer could be made more efficient by using composite pulse techniques [137]. The efficiency of the pulses we currently use varies across the cloud because of the spatially varying Rabi frequency caused by the microwave power decreasing further from the waveguide. The Rabi frequency varies by about $\pm 3\%$ across the cloud. The cloud-wide efficiency of spin control pulses could be increased using a composite pulse that is insensitive to these variations in Rabi frequency. The most straightforward composite pulse that is equivalent to a π -pulse involves three sequential pulses comprising of a $\pi/2$ -pulse, a π -pulse with the Rabi vector rotated by 90° , and another $\pi/2$ -pulse. In addition to improving pulse efficiency, composite pulses could be used to sculpt the initial transverse phase profile created during spin preparation.

7.2 Future experiments

The first spin system to explore is a two-domain spin profile with a spatially offset domain wall, where the dynamics of the position of the domain wall would be the focus of this experiment. An oscillation of the domain wall is likely, but the spin diffusion process of this oscillation is not clear since the total spin must be conserved through an oscillation. In addition, the stabilizing gradient should be smaller for offset domains because the density at the domain wall is reduced since it is no longer centered at the peak of the Gaussian density profile. In the hydrodynamic regime, the density scaling of the stabilizing gradient with initial domain offset could be explored. A density scaling of n^{-1} must be observed in the hydrodynamic regime to agree with Eqn. 6.1. The offset domain may also offer more insight on stabilizing domains at low density since the density of the domain can be easily tuned with domain offset.

The three-domain profile studied in Section 6.4 had both domain walls stabilized simultaneously, but the interactions between domain walls could also be explored. For this study, one domain wall could be stabilized and the longitudinal and transverse spin evolution would be observed. The potential coupling between the two domain walls would be the focus of this study. The dynamics of the unstable domain wall could be modified by the presence of a nearby stable domain wall. Data from this study could help one understand if domain walls can interact with each other or if they are independent. By adjusting the spacing between the domain walls a crossover between interacting domain walls and independent domain walls might be found.

A spin-independent potential as discussed in Section 2.5 could be used to shape a 1D density profile into a uniform density profile by reshaping the trapping potential. A uniform density profile is closer to the systems in early theoretical studies [131, 138, 139, 140] and is better suited for studying instabilities of transverse spin [58]. A uniform density profile corresponds to uniform total spin through the cloud, which could be used to focus on exploring spin diffusion without any density variations. Further shaping of the density profile could be used to create regions of higher or lower density and the effect of density modulations or density diffusion on spin diffusion could be studied.

The spin instability discussed in Section 5.3 could be further explored at smaller domain-wall widths and higher temperatures, where the strength of the instability is expected to be larger. The effect of density on the instability could also be explored. At low densities, fewer than one spin-rotating collision occurs on average during a trap oscillation so spins diffuse classically. At high densities where 100s of spin-rotating collisions occur within a trap oscillation, diffusing spins always adiabatically follow the local spin. Between the low and high density regimes there should exist an optimal density that maximizes the strength of the instability, creating the largest coherence ratio in Fig. 5.9. The differential potential could also play a role in amplifying or suppressing the instability, and various spatial and temporal variations of the differential potential could be explored.

With the digital micromirror device described in Section 3.8, the differential potential can be switched at fast rates (see Section 6.4). The temporal variation of the differential potential could be leveraged to further modify spin diffusion. The strength of differential potential gradients could be decreased as a function of time to compensate for the loss of total spin. This temporal compensation could potentially lead to spin domains being stable for longer than the 600 ms reported in Section 6.1. Alternatively, collective behaviour driven by oscillating differential potentials might provide insight on other techniques for modifying spin diffusion. Numerical simulations should be performed to check a few different approaches for temporally varying the differential potential. For example, the differential potential can be varied by using a temporally oscillating differential potential strength or quickly toggling between two static differential potentials. These are two examples, but this parameter space is incredibly large and simulations could be used to quickly guide the experiment on developing specific temporal variations in the differential potential. A first goal of temporally varying differential potentials could be to optimize the process of flipping a spin domain with minimal loss in magnitude. This process could be performed by

a π -pulse, but achieving the same result with only the differential potential would demonstrate incredible control of spin diffusion.

The spatial variation of the differential potential across the cloud can be used to design more complex initial spin profiles with individually controllable spin domains. These spin profiles could be used to explore the functionality of 1D spin devices in an ultracold gas. These spin-based device analogs could be designed following the approach outlined in Ref [141], in which ultracold atoms in a lattice are discussed as analogs to electronic devices. For our apparatus, two straightforward spin devices to start with are the spin diode and the spin transistor [142]. Both spin devices act similarly to their electronic counterparts except instead of n- and p-doped materials, spin-up and spin-down domains are used. The spin diode would allow a spin current to pass in one direction and no spin current to pass in the opposite direction. The spin transistor would amplify or switch a spin current by using a smaller spin current that can be controlled with a local differential potential. To create such devices, four-domain and five-domain spin profiles would have to be initialized for the diode and transistor, respectively. Two (three) spin domains are for the diode (transistor) and the extra two spin domains are used as a spin up or spin down reservoir, which are analogous to positive and negative current sources. The realization of these 1D spin devices in an ultracold gas could represent an incredible leap forward toward manipulating and controlling spin diffusion, and could assist in the development of new industrial or consumer devices.

Bibliography

- [1] R. Boyle and C. Merret, *New Experiments and Observations Touching Cold, Or, An Experimental History of Cold Begun: To which are Added an Examen of Antiperistasis and an Examen of Mr. Hobs's Doctrine about Cold* (London: John Crook, 1665).
- [2] W. Thomson, "On an absolute thermometric scale founded on Carnot's theory of the motive power of heat, and calculated from Regnault's observations," *Philosophical Magazine* pp. 100–106 (1848).
- [3] M. Faraday, "XIV. On fluid chlorine," *Philosophical Transactions of the Royal Society of London* **113**, 160–165 (1823).
- [4] M. Faraday, "XVII. On the condensation of several gases into liquids," *Philosophical Transactions of the Royal Society of London* **113**, 189–198 (1823).
- [5] S. U. Wróblewski and S. K. Olszewski, "Liquid state oxygen and nitrogen," *Annalen de Physik* **20**, 256–260 (1883).
- [6] W. A. Tilden, *A Short History of the Progress of Scientific Chemistry in our own Times* (Longmans, Green and Company, 1899).
- [7] J. Dewar, "Liquid hydrogen," *Science* **8**, 3–6 (1898).
- [8] H. K. Onnes, "The liquefaction of helium," *Koninklijke Nederlandse Akademie von Wetenschappen, Proceedings* **11**, 1908–1909 (1908).
- [9] H. London, G. R. Clarke and E. Mendoza, "Osmotic pressure of He³ in liquid He⁴, with proposals for a refrigerator to work below 1 K," *Physical Review* **128**, 1992–2005 (1962).
- [10] P. Das, R. B. de Ouboter and K. W. Taconis, "A realization of a London-Clarke-Mendoza type refrigerator," in *Low Temperature Physics LT9* (Springer, 1965), pp. 1253–1255.
- [11] D. J. Wineland, R. E. Drullinger and F. L. Walls, "Radiation-pressure cooling of bound resonant absorbers," *Physical Review Letters* **40**, 1639–1642 (1978).
- [12] C. Wieman and T. W. Hänsch, "Doppler-free laser polarization spectroscopy," *Physical Review Letters* **36**, 1170–1173 (1976).

- [13] T. W. Hänsch and A. L. Schawlow, “Cooling of gases by laser radiation,” *Optics Communications* **13**, 68–69 (1975).
- [14] W. D. Phillips, “Nobel lecture: Laser cooling and trapping of neutral atoms,” *Reviews of Modern Physics* **70**, 721–741 (1998).
- [15] C. Cohen-Tannoudji and W. D. Phillips, “New mechanisms for laser cooling,” *Physics Today* **43**, 33–40 (1990).
- [16] S. Chu, “Laser trapping of neutral particles,” *Scientific American* **266**, 70–77 (1992).
- [17] C. Salomon, J. Dalibard, W. D. Phillips, A. Clairon and S. Guellati, “Laser cooling of cesium atoms below 3 μK ,” *Europhysics Letters (EPL)* **12**, 683–688 (1990).
- [18] K. B. Davis, M.-O. Mewes, M. R. Andrews *et al.*, “Bose-Einstein condensation in a gas of sodium atoms,” *Physical Review Letters* **75**, 3969 (1995).
- [19] M. H. Anderson, J. R. Ensher, M. R. Matthews, C. E. Wieman and E. A. Cornell, “Observation of Bose-Einstein condensation in a dilute atomic vapor,” *Science* **269**, 198–201 (1995).
- [20] S. N. Bose, “Plancks gesetz und lichtquantenhypothese,” *Zeitschrift für Physik* **26**, 178–181 (1924).
- [21] A. Einstein, “Quantentheorie des einatomigen idealen gases,” *Sitzungsberichte der Preussischen Akademie der Wissenschaften, Physikalisch-mathematische Klasse* pp. 261–267 (1924).
- [22] T. Kovachy, J. M. Hogan, A. Sugarbaker *et al.*, “Matter wave lensing to picokelvin temperatures,” *Physical Review Letters* **114**, 143004 (2015).
- [23] A. E. Leanhardt, T. A. Pasquini, M. Saba *et al.*, “Cooling Bose-Einstein condensates below 500 picokelvin,” *Science* **301**, 1513–1515 (2003).
- [24] W. G. Jenks, S. S. H. Sadeghi and J. P. Wikswo Jr, “SQUIDs for nondestructive evaluation,” *Journal of Physics D: Applied Physics* **30**, 293–323 (1997).
- [25] D. H. Lee, “Routes to high-temperature superconductivity: a lesson from FeSe/SrTiO₃,” *Annual Review of Condensed Matter Physics* **9**, 261–282 (2018).
- [26] T. D. Ladd, F. Jelezko, R. Laflamme, Y. Nakamura, C. Monroe and J. L. O’Brien, “Quantum computers,” *Nature* **464**, 45–53 (2010).
- [27] C. Lacroix, P. Mendels and F. Mila, *Introduction to frustrated magnetism: materials, experiments, theory*, Volume 164 (Springer Science & Business Media, 2011).

- [28] C. A. Regal, M. Greiner and D. S. Jin, “Observation of resonance condensation of fermionic atom pairs,” *Physical Review Letters* **92**, 040403 (2004).
- [29] B. J. Bloom, T. L. Nicholson, J. R. Williams *et al.*, “An optical lattice clock with accuracy and stability at the 10^{-18} level,” *Nature* **506**, 71–75 (2014).
- [30] M. Takamoto, F.-L. Hong, R. Higashi and H. Katori, “An optical lattice clock,” *Nature* **435**, 321–324 (2005).
- [31] P. Asenbaum, C. Overstreet, T. Kovachy, D. D. Brown, J. M. Hogan and M. A. Kasevich, “Phase shift in an atom interferometer due to spacetime curvature across its wave function,” *Physical Review Letters* **118**, 183602 (2017).
- [32] J. M. McGuirk, G. T. Foster, J. B. Fixler, M. J. Snadden and M. A. Kasevich, “Sensitive absolute-gravity gradiometry using atom interferometry,” *Physical Review A* **65**, 033608 (2002).
- [33] M. Greiner, O. Mandel, T. Esslinger, T. W. Hänsch and I. Bloch, “Quantum phase transition from a superfluid to a Mott insulator in a gas of ultracold atoms,” *Nature* **415**, 39–44 (2002).
- [34] A. Griesmaier, J. Werner, S. Hensler, J. Stuhler and T. Pfau, “Bose-Einstein condensation of chromium,” *Physical Review Letters* **94**, 160401 (2005).
- [35] J. Stuhler, A. Griesmaier, T. Koch *et al.*, “Observation of dipole-dipole interaction in a degenerate quantum gas,” *Physical Review Letters* **95**, 150406 (2005).
- [36] M. Lu, N. Q. Burdick, S. H. Youn and B. L. Lev, “Strongly dipolar Bose-Einstein condensate of dysprosium,” *Physical Review Letters* **107**, 190401 (2011).
- [37] K. Aikawa, A. Frisch, M. Mark *et al.*, “Bose-Einstein condensation of erbium,” *Physical Review Letters* **108**, 210401 (2012).
- [38] J. Baron, W. C. Campbell, D. DeMille *et al.*, “Order of magnitude smaller limit on the electric dipole moment of the electron,” *Science* **343**, 269–272 (2014).
- [39] W. B. Cairncross, D. N. Gresh, M. Grau *et al.*, “Precision measurement of the electron’s electric dipole moment using trapped molecular ions,” *Physical Review Letters* **119**, 153001 (2017).
- [40] V. Galitski and I. B. Spielman, “Spin-orbit coupling in quantum gases,” *Nature* **494**, 49–54 (2013).
- [41] Y. Kawaguchi and M. Ueda, “Spinor Bose-Einstein condensates,” *Physics Reports* **520**, 253–381 (2012).
- [42] M.-S. Chang, C. D. Hamley, M. D. Barrett *et al.*, “Observation of spinor dynamics in optically trapped ^{87}Rb Bose-Einstein condensates,” *Physical Review Letters* **92**, 140403 (2004).

- [43] I. Bloch, J. Dalibard and W. Zwerger, “Many-body physics with ultracold gases,” *Reviews of Modern Physics* **80**, 885–964 (2008).
- [44] W. Ketterle, D. S. Durfee and D. M. Stamper-Kurn, “Making, probing and understanding Bose-Einstein condensates,” in *Proceedings of the International School on Physics “Enrico Fermi” 1998, Bose-Einstein Condensation in Atomic Gases*, edited by M. Inguscio, S. Stringari and C. E. Wieman (IOS Press, 1999), pp. 67–176.
- [45] N. Hinkley, J. A. Sherman, N. B. Phillips *et al.*, “An atomic clock with 10^{-18} instability,” *Science* **341**, 1215–1218 (2013).
- [46] Y. Y. Jiang, A. D. Ludlow, N. D. Lemke *et al.*, “Making optical atomic clocks more stable with 10^{-16} -level laser stabilization,” *Nature Photonics* **5**, 158–161 (2011).
- [47] F. Scazza, C. Hofrichter, M. Höfer, P. C. De Groot, I. Bloch and S. Fölling, “Observation of two-orbital spin-exchange interactions with ultracold SU(N)-symmetric fermions,” *Nature Physics* **10**, 779–784 (2014).
- [48] T. Bourdel, L. Khaykovich, J. Cubizolles *et al.*, “Experimental study of the BEC-BCS crossover region in lithium 6,” *Physical Review Letters* **93**, 050401 (2004).
- [49] J. Vijayan, P. Sompet, G. Salomon *et al.*, “Time-resolved observation of spin-charge deconfinement in fermionic Hubbard chains,” *electronic preprint arXiv:1905.13638v1 [cond-mat.quant-gas]* (2019).
- [50] T. Enss and J. H. Thywissen, “Universal spin transport and quantum bounds for unitary fermions,” *Annual Review of Condensed Matter Physics* **10**, 85–106 (2019).
- [51] I. Bloch, J. Dalibard and S. Nascimbene, “Quantum simulations with ultracold quantum gases,” *Nature Physics* **8**, 267–276 (2012).
- [52] E. P. Bashkin, “Spin waves in polarized paramagnetic gases,” *Journal of Experimental and Theoretical Physics* **33**, 8–11 (1981).
- [53] C. Lhuillier and F. Laloë, “Transport properties in a spin polarized gas, I,” *J. Physique* **43**, 197–224 (1982).
- [54] C. Lhuillier and F. Laloë, “Transport properties in a spin polarized gas, II,” *J. Physique* **43**, 225–241 (1982).
- [55] G. Nunes Jr, C. Jin, A. M. Putnam and D. M. Lee, “Longitudinal spin diffusion and nonlinear spin dynamics in a dilute $^3\text{-}^4\text{He}$ solution,” *Physical Review Letters* **65**, 2149–2152 (1990).

- [56] G. Nunes, C. Jin, D. L. Hawthorne, A. M. Putnam and D. M. Lee, “Spin-polarized $^3\text{--}^4\text{He}$ solutions: Longitudinal spin diffusion and nonlinear spin dynamics,” *Physical Review B* **46**, 9082–9103 (1992).
- [57] B. Castaing, “Polarized ^3He ,” *Physica B* **126**, 212–216 (1984).
- [58] A. Kuklov and A. E. Meyerovich, “Precessing domains and the Castaing instability in confined alkali-metal gases,” *Physical Review A* **66**, 023607 (2002).
- [59] R. Ragan and J. Baggett, “Leggett-Rice systems in harmonic traps,” *Journal of Low Temperature Physics* **134**, 369–374 (2004).
- [60] J. M. McGuirk, H. J. Lewandowski, D. M. Harber, T. Nikuni, J. E. Williams and E. A. Cornell, “Spatial resolution of spin waves in an ultracold gas,” *Physical Review Letters* **89**, 090402 (2002).
- [61] C. Deutsch, F. Ramirez-Martinez, C. Lacroûte *et al.*, “Spin self-rephasing and very long coherence times in a trapped atomic ensemble,” *Physical Review Letters* **105**, 020401 (2010).
- [62] A. Sommer, M. Ku, G. Roati and M. W. Zwierlein, “Universal spin transport in a strongly interacting Fermi gas,” *Nature* **472**, 201–204 (2011).
- [63] M. A. Nichols, L. W. Cheuk, M. Okan *et al.*, “Spin transport in a Mott insulator of ultracold fermions,” *Science* **363**, 383–387 (2019).
- [64] S. Smale, P. He, B. A. Olsen *et al.*, “Observation of a transition between dynamical phases in a quantum degenerate Fermi gas,” *Science Advances* **5**, eaax1568 (2019).
- [65] S. A. Wolf, D. D. Awschalom, R. A. Buhrman *et al.*, “Spintronics: a spin-based electronics vision for the future,” *Science* **294**, 1488–1495 (2001).
- [66] I. Žutić, J. Fabian and S. D. Sarma, “Spintronics: Fundamentals and applications,” *Reviews of Modern Physics* **76**, 323–410 (2004).
- [67] J. M. McGuirk, “Spin transport in coupled spinor Bose gases,” *Physical Review A* **82**, 011612 (2010).
- [68] J. M. McGuirk and L. F. Zajiczek, “Optical excitation of nonlinear spin waves,” *New Journal of Physics* **12**, 103020 (2010).
- [69] J. M. McGuirk and L. F. Zajiczek, “Localized collapse and revival of coherence in an ultracold Bose gas,” *Physical Review A* **83**, 013625 (2011).
- [70] I. I. Rabi, “Space quantization in a gyrating magnetic field,” *Physical Review* **51**, 652–654 (1937).

- [71] H. J. Metcalf and P. van der Straten, “Laser cooling and trapping of atoms,” *Journal of the Optical Society of America B* **20**, 887–908 (2003).
- [72] N. F. Ramsey, “A molecular beam resonance method with separated oscillating fields,” *Physical Review* **78**, 695–699 (1950).
- [73] T. R. Gentile, B. J. Hughey, D. Kleppner and T. W. Ducas, “Experimental study of one- and two-photon Rabi oscillations,” *Physical Review A* **40**, 5103–5115 (1989).
- [74] A. F. Linskens, I. Holleman, N. Dam and J. Reuss, “Two-photon Rabi oscillations,” *Physical Review A* **54**, 4854–4862 (1996).
- [75] K. Miyake, W. J. Mullin and P. C. E. Stamp, “Mean-field and spin-rotation phenomena in Fermi systems: the relation between the Leggett-Rice and Lhuillier-Laloë effects,” *Journal de Physique* **46**, 663–671 (1985).
- [76] A. Leggett and M. Rice, “Spin echoes in liquid He^3 and mixtures: A predicted new effect,” *Physical Review Letters* **20**, 586–589 (1968).
- [77] J. N. Fuchs, D. M. Gangardt and F. Laloë, “Internal state conversion in ultracold gases,” *Physical Review Letters* **88**, 230404 (2002).
- [78] R. F. Snider, “Quantum-mechanical modified Boltzmann equation for degenerate internal states,” *The Journal of Chemical Physics* **32**, 1051–1060 (1960).
- [79] J. N. Fuchs, D. M. Gangardt and F. Laloë, “Large amplitude spin waves in ultra-cold gases,” *European Physical Journal D* **25**, 57–75 (2003).
- [80] F. Laloë and W. J. Mullin, “On the Snider equation,” *Journal of Statistical Physics* **59**, 725–744 (1990).
- [81] A. D. Baute, I. L. Egusquiza and J. G. Muga, “Moller operators and Lippmann-Schwinger equations for steplike potentials,” *Journal of Physics A: Mathematical and General* **34**, 5341–5353 (2001).
- [82] H. J. Groenewold, “On the principles of elementary quantum mechanics,” in *On the Principles of Elementary Quantum Mechanics* (Springer, 1946), pp. 1–56.
- [83] M. O. S. M. Hillery, R. F. O’Connell, M. O. Scully and E. P. Wigner, “Distribution functions in physics: fundamentals,” *Physics Reports* **106**, 121–167 (1984).
- [84] H. J. Lewandowski, *Coherences and correlations in an ultracold Bose gas*, Ph.D. thesis, University of Colorado (2002).
- [85] T. Nikuni, J. E. Williams and C. W. Clark, “Linear spin waves in a trapped Bose gas,” *Physical Review A* **66**, 043411 (2002).

- [86] W. H. Press, S. A. Teukolsky, W. T. Vetterling and B. P. Flannery, *Numerical recipes 3rd edition: The art of scientific computing* (Cambridge University Press, 2007).
- [87] R. Grimm, M. Weidemüller and Y. B. Ovchinnikov, “Optical dipole traps for neutral atoms,” in *Advances in atomic, molecular, and optical physics* (Elsevier, 2000), Volume 42, pp. 95–170.
- [88] T. M. Miller and B. Bederson, “Atomic and molecular polarizabilities—a review of recent advances,” in *Advances in atomic and molecular physics* (Elsevier, 1978), Volume 13, pp. 1–55.
- [89] K. D. Bonin and V. V. Kresin, *Electric-dipole polarizabilities of atoms, molecules, and clusters* (World Scientific, 1997).
- [90] E. G. M. Van Kempen, S. J. J. M. F. Kokkelmans, D. J. Heinzen and B. J. Verhaar, “Interisotope determination of ultracold rubidium interactions from three high-precision experiments,” *Physical Review Letters* **88**, 093201 (2002).
- [91] A. Widera, F. Gerbier, S. Fölling, T. Gericke, O. Mandel and I. Bloch, “Precision measurement of spin-dependent interaction strengths for spin-1 and spin-2 ^{87}Rb atoms,” *New Journal of Physics* **8**, 152–152 (2006).
- [92] K. M. Mertes, J. W. Merrill, R. Carretero-González, D. J. Frantzeskakis, P. G. Kevrekidis and D. S. Hall, “Nonequilibrium dynamics and superfluid ring excitations in binary Bose-Einstein condensates,” *Physical Review Letters* **99**, 190402 (2007).
- [93] M. Egorov, B. Opanchuk, P. Drummond, B. V. Hall, P. Hannaford and A. I. Sidorov, “Measurement of s-wave scattering lengths in a two-component Bose-Einstein condensate,” *Physical Review A* **87**, 053614 (2013).
- [94] E. A. Burt, R. W. Ghrist, C. J. Myatt, M. J. Holland, E. A. Cornell and C. E. Wieman, “Coherence, correlations, and collisions: What one learns about Bose-Einstein condensates from their decay,” *Physical Review Letters* **79**, 337–340 (1997).
- [95] D. Niroomand, *Observation of the Castaing Instability in a Trapped Ultracold Bose Gas*, Master’s thesis, Simon Fraser University (2013).
- [96] F. Dalfovo, S. Giorgini, L. P. Pitaevskii and S. Stringari, “Theory of Bose-Einstein condensation in trapped gases,” *Reviews of Modern Physics* **71**, 463–512 (1999).
- [97] G. Breit and I. I. Rabi, “Measurement of nuclear spin,” *Physical Review* **38**, 2082–2083 (1931).
- [98] A. Corney, *Atomic and laser spectroscopy* (Clarendon Press Oxford, 1978).

- [99] D. M. Harber, H. J. Lewandowski, J. M. McGuirk and E. A. Cornell, “Effect of cold collisions on spin coherence and resonance shifts in a magnetically trapped ultracold gas,” *Physical Review A* **66**, 053616 (2002).
- [100] Texas Instruments Incorporated, “Cartoon “DLP control chip shot” showing how DLP technology works,” <http://www.ti.com/content/dam/ticom/images/products/ic/dlp-products/chips/dlp-control-chip-shot-dm1987.png>. [Online; accessed 7-September-2019].
- [101] Texas Instruments Incorporated, “DLP Discovery 4100 Development Platform,” <http://www.ti.com/tool/DLPD4X00KIT>. [Online; accessed 7-September-2019].
- [102] C. S. Corporation, “EZ-USB® FX2LP™ USB Microcontroller High-Speed USB Peripheral Controller,” <https://www.cypress.com/file/138911/download> (2019). Rev. AC [Online; accessed 7-September-2019].
- [103] Xilinx Incorporated, “Virtex-5,” <https://www.xilinx.com/support/documentation-navigation/silicon-devices/mature-products/virtex-5.html>. [Online; accessed 7-September-2019].
- [104] Texas Instruments Incorporated, “DLPC410 DMD Digital Controller,” <http://www.ti.com/product/DLPC410> (2019). Rev. F [Online; accessed 7-September-2019].
- [105] J. Axelson, *USB complete: the developer’s guide* (Lakeview research LLC, 2015).
- [106] USB Implementers Forum (USB-IF), “USB 2.0 Specification,” <https://www.usb.org/document-library/usb-20-specification> (2000). Rev 2.0 [Online; accessed 7-September-2019].
- [107] ISO, *ISO/IEC 9899:2011 Information technology — Programming languages — C* (pub-ISO, pub-ISO:adr, 2011).
- [108] ISO, *ISO/IEC 14882:2011 Information technology — Programming languages — C++* (pub-ISO, pub-ISO:adr, 2011), third edition.
- [109] N. I. Corporation, “What is LabVIEW? - National Instruments,” <https://www.ni.com/en-ca/shop/labview.html>. [Online; accessed 7-September-2019].
- [110] P. J. Ashenden, *The designer’s guide to VHDL*, Volume 3 (Morgan Kaufmann, 2010).
- [111] “libusb – a cross-platform user library to access USB devices,” <https://libusb.info/> or <https://github.com/libusb/libusb> (2007–2019). [Online; accessed 7-September-2019].
- [112] G. Gauthier, I. Lenton, N. M. Parry *et al.*, “Direct imaging of a digital-micromirror device for configurable microscopic optical potentials,” *Optica* **3**, 1136–1143 (2016).

- [113] J.-Y. Zheng, R. M. Pasternack and N. N. Boustany, “Optical scatter imaging with a digital micromirror device,” *Optics Express* **17**, 20401–20414 (2009).
- [114] C. Kuang, Y. Ma, R. Zhou *et al.*, “Digital micromirror device-based laser-illumination Fourier ptychographic microscopy,” *Optics Express* **23**, 26999–27010 (2015).
- [115] A. Hessel, J. Schmoys and D. Y. Tseng, “Bragg-angle blazing of diffraction gratings,” *Journal of the Optical Society of America A* **65**, 380–384 (1975).
- [116] B. L. Lee, C. E. Tew and W. M. Duncan, “Two-dimensional blazed MEMS grating,” (2005). US Patent 6,943,950.
- [117] R. W. Steinberg and L. Floyd, “An adaptive algorithm for spatial greyscale,” in *Proceedings of the Society for Information Display* (1976), Volume 17, pp. 78–84.
- [118] J. F. Jarvis, C. N. Judice and W. H. Ninke, “A survey of techniques for the display of continuous tone pictures on bilevel displays,” *Computer Graphics and Image Processing* **5**, 13–40 (1976).
- [119] F. Sierra, in LIB 17 (Developer’s Den), CIS Graphics Support Forum (unpublished) (1989).
- [120] T. Riemersma, “A balanced dithering technique,” *C/C++ Users Journal* **16** (1998).
- [121] R. Ulichney, *Digital halftoning* (MIT Press, 1987).
- [122] N. Damera-Venkata and B. L. Evans, “FM halftoning via block error diffusion,” in *Proceedings 2001 International Conference on Image Processing (Cat. No. 01CH37205)* (IEEE, 2001), Volume 2, pp. 1081–1084.
- [123] C. J. Pethick and H. Smith, *Bose-Einstein condensation in dilute gases* (Cambridge University Press, 2008).
- [124] K. Huang, *Statistical Mechanics* (John Wiley and Sons, New York, 1987), 2nd edition.
- [125] D. Niroomand, S. D. Graham and J. M. McGuirk, “Longitudinal spin diffusion in a nondegenerate trapped ^{87}Rb gas,” *Physical Review Letters* **115**, 075302 (2015).
- [126] H. Akimoto, O. Ishikawa, G.-H. Oh, M. Nakagawa, T. Hata and T. Kodama, “Nonlinear effects on spin waves in ^3He - ^4He dilute solutions,” *Journal of Low Temperature Physics* **82**, 295–316 (1991).

- [127] R. J. Ragan and D. M. Schwarz, “Castaing instabilities in longitudinal spin-diffusion experiments,” *Journal of Low Temperature Physics* **109**, 775–799 (1997).
- [128] J. N. Fuchs, O. Prévoté and D. M. Gangardt, “Castaing’s instability in a trapped ultra-cold gas,” *European Physical Journal D* **25**, 167–171 (2003).
- [129] A. E. Meyerovich, “Quantum and nonlocal coherent effects in Boltzmann gases,” *Physical Review B* **39**, 9318–9329 (1989).
- [130] S. D. Graham, D. Niroomand, R. J. Ragan and J. M. McGuirk, “Stable spin domains in a nondegenerate ultracold gas,” *Physical Review A* **97**, 051603 (2018).
- [131] I. A. Fomin and V. V. Dmitriev, “Coherently precessing spin structure in a normal Fermi-liquid,” *Journal of Experimental and Theoretical Physics Letters* **59**, 378–384 (1994).
- [132] A. E. Meyerovich, J. H. Naish, J. R. Owers-Bradley and A. Stepaniants, “Zero-temperature relaxation in spin-polarized Fermi systems,” *Low Temperature Physics* **23**, 411–419 (1997).
- [133] R. J. Ragan, personal communication.
- [134] V. B. Braginsky and F. Y. Khalili, “Quantum nondemolition measurements: the route from toys to tools,” *Reviews of Modern Physics* **68**, 1–11 (1996).
- [135] M. Gajdacz, P. L. Pedersen, T. Mørch, A. J. Hilliard, J. Arlt and J. F. Sherson, “Non-destructive Faraday imaging of dynamically controlled ultracold atoms,” *Review of Scientific Instruments* **84**, 083105 (2013).
- [136] I. Carusotto and E. J. Mueller, “Imaging of spinor gases,” *Journal of Physics B: Atomic, Molecular and Optical Physics* **37**, S115–S125 (2004).
- [137] M. H. Levitt, “Composite pulses,” *Progress in Nuclear Magnetic Resonance Spectroscopy* **18**, 61–122 (1986).
- [138] I. A. Fomin, “Transverse spin dynamics of a spin-polarized Fermi liquid,” *Journal of Experimental and Theoretical Physics Letters* **65**, 749–754 (1997).
- [139] N. Masuhara, D. Candela, D. O. Edwards *et al.*, “Collisionless spin waves in liquid ^3He ,” *Physical Review Letters* **53**, 1168–1171 (1984).
- [140] L. P. Lévy and A. E. Ruckenstein, “Collective spin oscillations in spin-polarized gases: Spin-polarized hydrogen,” *Physical Review Letters* **52**, 1512–1515 (1984).
- [141] B. T. Seaman, M. Krämer, D. Z. Anderson and M. J. Holland, “Atomtronics: Ultracold-atom analogs of electronic devices,” *Physical Review A* **75**, 023615 (2007).

- [142] S. Datta and B. Das, “Electronic analog of the electro-optic modulator,” *Applied Physics Letters* **56**, 665–667 (1990).
- [143] D. A. Steck, “Rubidium 87 D line data,” (2001).

Appendix A

Physical parameters of ^{87}Rb

Table A.1: Selection of relevant properties of ^{87}Rb from Ref. [143]

Property	Symbol	Value
Physical properties		
Atomic mass	m	$1.443160648(72) \times 10^{-25}$ kg
Nuclear spin	I	3/2
Nuclear lifetime	τ_n	4.88×10^{10} yr
Properties of D2 transition in ^{87}Rb ($5S_{1/2} \rightarrow 5P_{3/2}$)		
Frequency	ω_0	$2\pi \cdot 384.2304844685(62)$ THz
Natural line width	Γ	$2\pi \cdot 6.0666(18)$ MHz
Transition dipole matrix element	$\langle J = 1/2 e\mathbf{r} J' = 3/2 \rangle$	$3.58424(74) \times 10^{-29}$ C·m
Cycling transition saturation intensity $ F = \pm 2\rangle \rightarrow F = \pm 3\rangle$	I_{sat}	1.66933(35) mW/cm ²
Nuclear g -factor	g_I	-0.000 995 141 4(10)
Ground-state polarizability	$\alpha_0(5S_{1/2})$	$h \cdot 0.0794(16)$ Hz/(V/cm) ²

Appendix B

Collisional integrals for 1D spin transport

The collision integrals in the quantum Boltzmann equation can be computationally expensive to solve so a relaxation time approximation is used to simplify the theoretical and numerical work with reasonable accuracy. In this appendix, the full details of the collisional integrals are stated from Ref. [85]. These collision integrals could be used to incorporate the slightly different scattering lengths for the ^{87}Rb spin states used, which would be the same as including a transverse spin decay. While this transverse spin decay time is long (~ 10 s) in this ^{87}Rb experiment, it could be shorter in other experiments or with other atoms, where these collisional integrals would be useful.

For atomic density distribution f and spin density distribution $\underline{\mathbf{m}}$, the collision integrals are

$$\left. \frac{\partial f}{\partial t} \right|_{\text{collisions}} = \frac{\pi g^2}{\hbar} \int \frac{d\underline{\mathbf{p}}_2}{(2\pi\hbar)^3} \int \frac{d\underline{\mathbf{p}}_3}{(2\pi\hbar)^3} \int d\underline{\mathbf{p}}_4 \delta(\epsilon_p + \epsilon_{p_2} - \epsilon_{p_3} - \epsilon_{p_4}) \delta(\underline{\mathbf{p}} + \underline{\mathbf{p}}_2 - \underline{\mathbf{p}}_3 - \underline{\mathbf{p}}_4) \{3[f(\underline{\mathbf{p}}_3)f(\underline{\mathbf{p}}_4) - f(\underline{\mathbf{p}})f(\underline{\mathbf{p}}_2)] + \underline{\mathbf{m}}(\underline{\mathbf{p}}_3) \cdot \underline{\mathbf{m}}(\underline{\mathbf{p}}_4) - \underline{\mathbf{m}}(\underline{\mathbf{p}}) \cdot \underline{\mathbf{m}}(\underline{\mathbf{p}}_2)\} \quad (\text{B.1})$$

and

$$\left. \frac{\partial \underline{\mathbf{m}}}{\partial t} \right|_{\text{collisions}} = \frac{\pi g^2}{\hbar} \int \frac{d\underline{\mathbf{p}}_2}{(2\pi\hbar)^3} \int \frac{d\underline{\mathbf{p}}_3}{(2\pi\hbar)^3} \int d\underline{\mathbf{p}}_4 \left[\delta(\epsilon_p + \epsilon_{p_2} - \epsilon_{p_3} - \epsilon_{p_4}) \delta(\underline{\mathbf{p}} + \underline{\mathbf{p}}_2 - \underline{\mathbf{p}}_3 - \underline{\mathbf{p}}_4) \{3f(\underline{\mathbf{p}}_3)\underline{\mathbf{m}}(\underline{\mathbf{p}}_4) + \underline{\mathbf{m}}(\underline{\mathbf{p}}_3)f(\underline{\mathbf{p}}_4) - f(\underline{\mathbf{p}})\underline{\mathbf{m}}(\underline{\mathbf{p}}_2) - 3\underline{\mathbf{m}}(\underline{\mathbf{p}})f(\underline{\mathbf{p}}_2)\} \right], \quad (\text{B.2})$$

where $\epsilon_p = p^2/2m$ and the definitions of p_2, p_3, p_4 can be found in Section 2.2.

Appendix C

1D quantum Boltzmann equation in Cartesian, cylindrical, and spherical coordinate systems

The 1D quantum Boltzmann equation in vector form is

$$\frac{\partial \underline{\mathbf{m}}}{\partial t} = -\frac{p}{m_{\text{atomic}}} \partial_z \underline{\mathbf{m}} + m\omega_z^2 z \partial_p \underline{\mathbf{m}} + \frac{1}{\hbar} (U_{\text{diff}} \hat{\mathbf{z}} + g \underline{\mathbf{M}}) \times \underline{\mathbf{m}} + \left. \frac{\partial \underline{\mathbf{m}}}{\partial t} \right|_{1\text{D}}, \quad (\text{C.1})$$

where $\underline{\mathbf{M}} = \frac{1}{2\pi\hbar} \int dp \underline{\mathbf{m}}$ is the spin density, which is the observable. Note that the integral for $\underline{\mathbf{M}}$ must be performed over Cartesian coordinates because the integral breaks the contravariance property of the vector so that $M_x^2 + M_y^2 \neq \int dp m_\rho$. The 1D quantum Boltzmann equation for $\underline{\mathbf{m}}$ is expressed in three coordinate systems below. In Cartesian coordinates $\{x, y, z\}$ it reads

$$\frac{\partial \underline{\mathbf{m}}}{\partial t} = \frac{\partial m_x}{\partial t} \hat{\mathbf{x}} + \frac{\partial m_y}{\partial t} \hat{\mathbf{y}} + \frac{\partial m_z}{\partial t} \hat{\mathbf{z}} \quad (\text{C.2})$$

$$\begin{aligned} \frac{\partial m_z}{\partial t} = & -\frac{p}{m_{\text{atomic}}} \partial_z m_z + m\omega_z^2 z \partial_p m_z - \frac{g}{\hbar} (M_x m_y - M_y m_x) \\ & - \frac{1}{\tau} (m_z - \lambda_{\text{dB}} e^{-p^2/2mk_B T} M_z) \end{aligned} \quad (\text{C.3})$$

$$\begin{aligned} \frac{\partial m_x}{\partial t} = & -\frac{p}{m_{\text{atomic}}} \partial_z m_x + m\omega_z^2 z \partial_p m_x - \frac{U_{\text{diff}}}{\hbar} m_y + \frac{g}{\hbar} (M_y m_z - M_z m_y) \\ & - \frac{1}{\tau} (m_x - \lambda_{\text{dB}} e^{-p^2/2mk_B T} M_x) \end{aligned} \quad (\text{C.4})$$

$$\begin{aligned} \frac{\partial m_y}{\partial t} = & -\frac{p}{m_{\text{atomic}}} \partial_z m_y + m\omega_z^2 z \partial_p m_y + \frac{U_{\text{diff}}}{\hbar} m_x - \frac{g}{\hbar} (M_x m_z - M_z m_x) \\ & - \frac{1}{\tau} (m_y - \lambda_{\text{dB}} e^{-p^2/2mk_B T} M_y). \end{aligned} \quad (\text{C.5})$$

In cylindrical coordinates $\{z, \rho, \phi\}$ it reads

$$\frac{\partial \underline{m}}{\partial t} = \frac{\partial m_\rho}{\partial t} \hat{\rho} + m_\rho \frac{\partial m_\phi}{\partial t} \hat{\phi} + \frac{\partial m_z}{\partial t} \hat{z} \quad (\text{C.6})$$

$$\begin{aligned} \frac{\partial m_z}{\partial t} = & -\frac{p}{m_{\text{atomic}}} \partial_z m_z + m\omega_z^2 z \partial_p m_z - \frac{g}{\hbar} M_\rho m_\rho \sin(M_\phi - m_\phi) \\ & - \frac{1}{\tau} \left(m_z - \lambda_{\text{dB}} e^{-p^2/2mk_B T} M_z \right) \end{aligned} \quad (\text{C.7})$$

$$\begin{aligned} \frac{\partial m_\rho}{\partial t} = & -\frac{p}{m_{\text{atomic}}} \partial_z m_\rho + m\omega_z^2 z \partial_p m_\rho + \frac{g}{\hbar} M_\rho m_z \sin(M_\phi - m_\phi) \\ & - \frac{1}{\tau} \left(m_\rho - \lambda_{\text{dB}} e^{-p^2/2mk_B T} M_\rho \cos(M_\phi - m_\phi) \right) \end{aligned} \quad (\text{C.8})$$

$$\begin{aligned} \frac{\partial m_\phi}{\partial t} = & -\frac{p}{m_{\text{atomic}}} \partial_z m_\phi + m\omega_z^2 z \partial_p m_\phi + \frac{U_{\text{diff}}}{\hbar} + \frac{g}{\hbar} M_z - \frac{g}{\hbar} M_\rho \frac{m_z}{m_\rho} \cos(M_\phi - m_\phi) \\ & + \frac{1}{\tau} \lambda_{\text{dB}} e^{-p^2/2mk_B T} \frac{M_\rho}{m_\rho} \sin(M_\phi - m_\phi). \end{aligned} \quad (\text{C.9})$$

And in spherical coordinates $\{r, \theta, \phi\}$ it reads

$$\frac{\partial \underline{m}}{\partial t} = \frac{\partial m_r}{\partial t} \hat{r} + m_r \frac{\partial m_\theta}{\partial t} \hat{\theta} + m_r \sin(m_\theta) \frac{\partial m_\phi}{\partial t} \hat{\phi} \quad (\text{C.10})$$

$$\begin{aligned} \frac{\partial m_r}{\partial t} = & -\frac{p}{m_{\text{atomic}}} \partial_z m_r + m\omega_z^2 z \partial_p m_r \\ & - \frac{1}{\tau} \left(m_r - \lambda_{\text{dB}} e^{-p^2/2mk_B T} M_r \left[\sin(M_\theta) \sin(m_\theta) \cos(M_\phi - m_\phi) + \cos(M_\theta) \cos(m_\theta) \right] \right) \end{aligned} \quad (\text{C.11})$$

$$\begin{aligned} \frac{\partial m_\theta}{\partial t} = & -\frac{p}{m_{\text{atomic}}} \partial_z m_\theta + m\omega_z^2 z \partial_p m_\theta + \frac{g}{\hbar} M_r \sin(M_\theta) \sin(M_\phi - m_\phi) \\ & + \frac{1}{\tau} \lambda_{\text{dB}} e^{-p^2/2mk_B T} \frac{M_r}{m_r} \left(\sin(M_\theta) \cos(m_\theta) \cos(M_\phi - m_\phi) - \cos(M_\theta) \sin(m_\theta) \right) \end{aligned} \quad (\text{C.12})$$

$$\begin{aligned} \frac{\partial m_\phi}{\partial t} = & -\frac{p}{m_{\text{atomic}}} \partial_z m_\phi + m\omega_z^2 z \partial_p m_\phi + \frac{U_{\text{diff}}}{\hbar} \\ & + \frac{g}{\hbar} M_r \cos(M_\theta) - \frac{g}{\hbar} M_r \sin(M_\theta) \frac{\cos(m_\theta)}{\sin(m_\theta)} \cos(M_\phi - m_\phi) \\ & + \frac{1}{\tau} \lambda_{\text{dB}} e^{-p^2/2mk_B T} \frac{M_r \sin(M_\theta)}{m_r \sin(m_\theta)} \sin(M_\phi - m_\phi). \end{aligned} \quad (\text{C.13})$$

The components of the spin density distribution $m_x, m_y, m_z, m_\rho, m_r$ are all dimensionless and m_θ and m_ϕ are in radians. The spin densities $M_x, M_y, M_z, M_\rho, M_r$ are in units of m^{-1} , but M_θ and M_ϕ are in units of radians, which is a key distinction between the units of the components of \underline{m} and \underline{M} .